UNIVERSITÀ DEGLI STUDI DI MILANO BICOCCA
DIPARTIMENTO DI SCIENZA DEI MATERIALI

GAAS NANOSTRUCTURES FOR THE GENERATION OF ENTANGLED PHOTONS: DESIGN, DEVELOPMENT, AND SPECTROSCOPY

Francesco Basso Basset

Supervisor
Prof. Emiliano Bonera

SCUOLA DI DOTTORATO
UNIVERSITÀ DEGLI STUDI DI MILANO-BICOCCA

DEPARTMENT OF MATERIALS SCIENCE
PhD PROGRAM IN MATERIALS SCIENCE AND NANOTECHNOLOGY
Curriculum in Materials Science

GaAs nanostructures for the generation of entangled photons: design, development, and spectroscopy

FRANCESCO BASSO BASSET

XXX Cycle - Reg. nº 798795

Supervisor: Prof. Emiliano Bonera
Coordinator: Prof. Marco Bernasconi

Academic Year 2016/2017

Contents

Chapter 1

Introduction

The last few years have witnessed to a steadily growing interest in some areas of physics and engineering towards the field of quantum technologies. Under this term fall a variety of research topics aimed at developing devices with a novel functionality or better performance whose operation is based on the generation, transfer, storage, manipulation, or probing of quantum states of matter or light [1–10].

The ability to address physical systems whose description is bound to purely quantum mechanical properties, such as quantum entanglement, quantum superposition and quantum tunneling, has often been boosted by progress in nanoscale science and technology. Epitaxial quantum dots are a prominent example of this process. On the one hand, they have similar electronic and optical properties to single atoms, on the other hand, they are designed, fabricated, and processed using experimental techniques developed for the manufacturing of semiconductor devices.

In this thesis, I will focus on the study of quantum dots as solid-state sources of polarization-entangled photon pairs. The production of entangled polarization states of light, crucial for the first experimental demonstration of the foundations of quantum mechanics [11, 12], plays now an important role in several protocols for quantum cryptography and communication [13]. In contrast to current technological solutions, the potential for on-demand operation and device scalability make quantum dots a promising candidate as building block for quantum networks able to exchange photon qubits between distant nodes [14].

Several challenges lie ahead in the direction of this goal. Strict conditions must be met in order to reliably and reproducibly fabricate emitters able to provide an elevated degree of entanglement. A high structural symmetry and a proper choice of materials are crucial to tackle the main sources of entanglement degradation, namely the fine structure energy splitting between the bright exciton states [15–17] and fluctuating nuclear magnetic fields due to the hyperfine interaction [18–20]. At the same time, the wavelength of operation is required to match efficient single-photon detectors and optical quantum memories able to slow down and store photon qubits [21, 22]. The main sources of spectral wandering have to be suppressed, and the emitted photons are required to be indistinguishable [23] and highly coherent [24] so to observe clear two-photon quantum interference at a beamsplitter. Optimal performance is only achieved by maximizing the brightness of the emitter, the collection efficiency, and the fidelity in the preparation of the quantum state and in its detection [25].

Among the several approaches that have been investigated during the last decade, droplet epitaxy enables control of the shape, size, density, and emission wavelength of the quantum dots, together with some flexibility on the materials choice [26]. Nonetheless, the fraction of entanglement-ready quantum dots that can be fabricated with this method is still limited to values around 5% [27], and matching the energy of the entangled photons to atomic transitions in vapor cells—a promising implementation of optical memories for quantum networking—remains an open problem.

Here I present a novel approach to droplet epitaxy for the fabrication of GaAs/AlGaAs quantum dots on a (111)A-oriented substrate. The challenges described above are dealt with by tackling a long-standing drawback of this technique, namely the low substrate temperature required for the fundamental crystallization step [28, 29]. Thanks to the peculiar surface dynamics associated with the (111)A orientation, quantum dot formation is observed up to the temperature of deposition of a high quality AlGaAs matrix, giving access to a novel parameter space of growth conditions.

The impact of the growth parameters on the structural properties—size distribution, aspect ratio, shape symmetry, and crystalline quality—is investigated. A great deal of attention is devoted to the characterization of the optical properties relevant for the envisaged application as entangled photon emitters—emission wavelength, fine structure splitting, radiative

lifetime, and excitonic linewidth. As the correlation between the growth parameters and the various figures of merit from the photoluminescence analysis is understood, the design process of the nanostructures is improved. Ultimately, state-of-the-art values are found in each investigated aspect.

A resonant two-photon excitation scheme is successfully adopted in order to obtain high single-photon emission purity and to demonstrate the generation of entangled photon pairs. Droplet epitaxy of GaAs/AlGaAs nanostructures is proved to offer a simple strategy based on self-assembly to obtain a high yield of entanglement-ready emitters in a spectral region compatible with atomic vapor cells for quantum networking.

Nonetheless, the use of a tunable external field would provide, in addition, accurate matching of the atomic transitions in vapor cells and complete restoring of the bright exciton degeneracy to maximize entanglement fidelity. As a possible development in this direction, the compatibility with electrically controlled strain tuning [30, 31] is explored. In particular, I address the problem of integrating a membrane containing high quality GaAs (111)A quantum dots on top of a piezoelectric substrate by means of semiconductor processing techniques.

The last major step towards the realization of an efficient solid-state entangled photon source is enhancing light extraction efficiency. While this point is not investigated in this work, several effective strategies compatible with molecular beam epitaxy exist, such as integration in optical microcavities, photonic-crystal cavities, microdisk resonators, microlenses, nanophotonic waveguides, and tapered nanowires [23, 32]. However, the choice of the (111)A substrate orientation, less investigated than the (100) counterpart, poses additional challenges concerning the growth of complex heterostructures [33] and doping [34]. Some preliminary results on the use of a 2° miscut substrate to increase the deposition rate are presented, which could bridge the gap towards the fabrication of thick distributed Bragg reflectors.

I briefly outline below how the contents presented in the thesis are organized.

Chapter 2 gives a basic introduction to the concept of entanglement and to the relevant case study of the joint polarization state of two photons. Different experimental methods to generate pairs of polarization-entangled

photons are explained and reviewed, with particular regard to the biexciton-exciton cascade in quantum dots.

In the next chapter, I provide a theoretical background on the electronic structure of quantum dots, from the single particle picture to the excitonic effects, and on the physics of the radiative recombination in these systems. A brief section is devoted to the epitaxial growth technique used to fabricate the quantum dots in this work.

In chapter 4, I describe the experimental techniques and illustrate in detail the setups and their operating procedures.

The fifth chapter contains the main body of original results. The first main section extensively studies the relationship between the growth parameters, the morphology of the dots as probed on the uncapped samples, and the ensemble and individual optical properties of the emitters. The sample obtained from the process of growth optimization is then characterized more in depth with additional single dot spectroscopic measurements. Finally, the generation of polarization-entangled photon pairs is discussed and experimentally demonstrated.

Chapter 6 presents a successful approach to transfer the quantum dots developed in the previous chapter on top of a piezoelectric substrate for the fine tuning of the emission wavelength and the fine structure splitting. The challenges related to the crystalline and optical quality of the material are discussed in detail.

Finally, the last chapter summarizes the main results and delineates some possible directions for future research.

Chapter 2

Polarization-entangled photons for quantum networks

2.1 Overview: from foundations to quantum technologies

Entanglement is the physical property of a set of particles whose quantum states cannot be described independently, even when separated by large distances and not interacting. This concept is undoubtedly one of the most groundbreaking and far-reaching ideas introduced by the theory of quantum mechanics. The counter-intuitive nature of this phenomenon was pointed out in a seminal paper by Einstein, Podolsky and Rosen [35]. In this work, the authors demonstrated the incompatibility of the behavior of a two-particle system formed from the decay of a radioactive source as described by the fundamental laws of quantum mechanics with a local realist physical description of nature. The EPR paradox stimulated a lively debate around the Copenhagen interpretation of quantum mechanics and the possibility of a hidden local reality theory, but the question was not settled until decades later, when John Bell came up with an experimental test for the foundations of quantum mechanics [36]. Bell theoretically investigated two-particle correlations of a two spin 1/2 singlet state and revealed that the outcomes of specific measurements of non-commuting observables violate a series of inequalities which must hold under the hypothesis of local realism.

Experimental work on polarization-entangled photon pairs from atomic cascades followed [11, 12] and overcame the classical threshold in the Bell inequalities as expected from the quantum theory.

While the demonstration of the foundations of quantum mechanics has grown more and more sophisticated [37], a field of research in constant development has addressed the possibility of manipulating single quantum states of matter and light—in a regime where entanglement is not washed out by decoherence effects—for practical applications. Several are the areas where quantum technologies may play a role, namely communication [1, 2], simulations [3–5], sensing [6] and computing [7–10].

Inside this general research framework, photonics-based technologies cover an important range of applications [38, 39]. Indeed, a single photon is an excellent qubit, especially, but not only, for purposes of secure information transfer and processing, thanks to the unrivaled resistance to the decoherence from the environment. Other advantages are the high speed of transmission and the convenience of manipulating quantum states by means of delay lines and linear optical elements.

All these potential applications rely on the ability to produce and manipulate single and entangled photon states. Efficient generation of entangled photon pairs is crucial for several quantum communication protocols and some approaches to quantum computation [13]. In particular, a yearned long-term scientific and technological goal is the realization of a quantum network able to distribute entanglement over distant nodes [14]. A major milestone in this research direction would be the implementation of a quantum repeater.

Since the concept of classical signal amplification cannot be applied to single-photon qubits because of the no-cloning theorem, the maximum travel distance of a photon is limited by the extinction coefficient of the medium where it propagates. An alternative approach [40] that relies on the principle of entanglement swapping [41] has been devised. Entanglement swapping is a quantum information scheme which allows to entangle two particles that never interacted between each other. Starting from two pairs of particles, each in an entangled Bell state, a joint Bell state measurement is performed on a qubit from each pair. As a result, the other two particles are also projected on a Bell state. This concept can be practically implemented by using two polarization-entangled photon sources and making two photons

from each source interact at the same time on a non-polarizing beam splitter. A synthetic diagram of this procedure is reported in Fig. 2.1. The figure also shows how this approach can be scaled up for long-distance entanglement distribution by inserting quantum memories able to temporarily store a photon state. In this way, it is possible to achieve a polynomial scaling of the communication efficiency with the channel length.

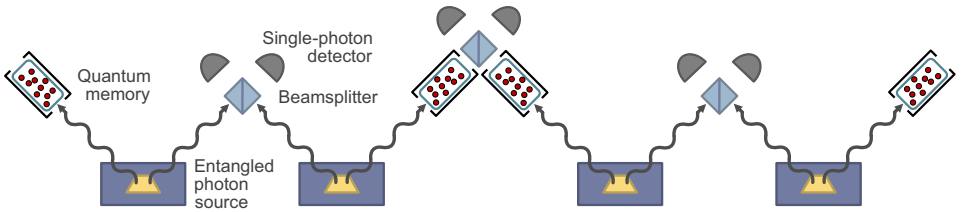

FIGURE 2.1: Diagram of a quantum repeater consisting of synchronized sources of polarization-entangled photons, beamsplitters and single-photon detectors arranged to perform Bell state measurements, and quantum memories able to store a photon state in case of an operation failure in one of the other nodes of the repeater.

Apart from its immediate function, the realization of a quantum repeater is a relevant target, because it is a relatively simple device and, at the same time, contains all the fundamental building blocks of a quantum network. Therefore, it defines the main requirements for a practical source of entangled photons: it should be able to generate indistinguishable photon pairs on demand and must operate at an emission wavelength covered by highly efficient single-photon detectors and matched by a quantum memory or a storage medium able to slow down and release a photon when requested.

2.2 Entangled states of photonic qubit pairs

A multi-particle system is called entangled when its global state $|\psi\rangle$ cannot be described as a direct product of single particle states $|\psi_i\rangle$ [42, 43].

$$|\psi\rangle = \sum_{i=\mathbf{i}_1,\ldots,\mathbf{i}_n} c_{\mathbf{i}_1,\ldots,\mathbf{i}_n} |\mathbf{i}_1\rangle \otimes |\mathbf{i}_2\rangle \otimes \ldots \otimes |\mathbf{i}_n\rangle \neq |\psi_1\rangle \otimes |\psi_2\rangle \otimes \ldots \otimes |\psi_n\rangle \quad (2.1)$$

$|\mathbf{i}_j\rangle$ represents an orthonormal basis for the jth single particle, $c_{\mathbf{i}_1,\ldots,\mathbf{i}_n}$ are normalized complex coefficients.

In this thesis, I will discuss the simplest case of entanglement, the one between a pair of qubits. A qubit is a generalization of the classical bit, a quantum state formed by the linear superposition in an Hilbert space of two orthogonal states $|0\rangle$ and $|1\rangle$.

Any particle or physical property described by an isolated two-level system can implement a qubit. When a pair of qubits is considered, it is possible to identify a basis of four maximally entangled states $|\psi^{\pm}\rangle_{AB}$ and $|\phi^{\pm}\rangle_{AB}$, also known as Bell states.

$$|\psi^{\pm}\rangle_{AB} \equiv \frac{1}{\sqrt{2}}(|0\rangle_A |1\rangle_B \pm |1\rangle_A |0\rangle_B) \tag{2.2}$$

$$|\phi^{\pm}\rangle_{AB} \equiv \frac{1}{\sqrt{2}}(|0\rangle_A |0\rangle_B \pm |1\rangle_A |1\rangle_B) \tag{2.3}$$

An entangled state must not be confused with a statistical mixture of two-qubit states. Mixed states can be necessary to describe the effects of decoherence or statistical measurements and are represented with the formalism of the density matrix $\hat{\rho}$.

$$\hat{\rho} = \sum_i p_i |\varphi_i\rangle \langle\varphi_i| \tag{2.4}$$

p_i is the probability that the system is in the state $|\varphi_i\rangle$.

Photons offer different degrees of freedom that can be used to encode a qubit [13, 44, 45]. The approach that has received more attention up to date and that was used for the first experimental demonstration of quantum entanglement consists in using the polarization state of the photon as the qubit. This is a natural choice because a photon is a spin 1 particle with just two eigenvalues of spin, $\pm\hbar$, along its direction of propagation. These two states correspond to right-handed and left-handed circularly polarized light respectively. Polarization states can conveniently be manipulated and measured by means of linear polarizers and wave plates.

Nonetheless, as mentioned, also other approaches have been investigated, and entangled states have been prepared using space and time separation, frequency difference, and orbital angular momentum. Among

these options, storing a qubit in time-bins [46, 47] is probably the most serious alternative to a polarization state for applications in fiber transmission. A time-bin qubit can be created by using an unbalanced Mach-Zehnder interferometer, whose delay is longer than the coherence time of the photon wave packet. This strategy can even be combined in hyper-entanglement schemes with polarization states [48]. However, this work is going to focus on the latter choice of qubit.

A promising approach to construct entangled states relies on the use of linear optical elements, such as beam splitters and phase shifters, in combination with a clocked source of indistinguishable photons [49, 50]. The alternative route, which has taken on a paramount role in the experimental research on quantum technologies throughout the years, is the direct generation of polarization-entangled photon pairs. In fact, several physical mechanisms have been studied to perform this task.

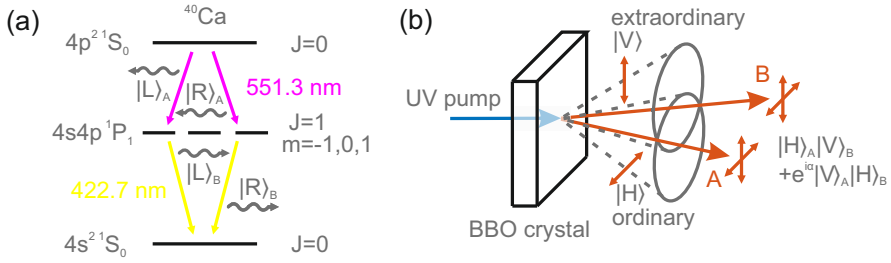

FIGURE 2.2: a) Energy diagram which describes the decay of a Ca atom from a $4p^2$ state to ground state with emission of a pair of photons correlated in polarization. b) Generation of polarization-entangled photons from type II parametric down-conversion. Phase-matching conditions require that the down-converted photons emerge in cones of opposite polarization and quantum superposition at the intersections produces entanglement.

The first attempts searched for entanglement in gamma-ray photons produced by positron annihilation [51], but they were limited by the poor performance of polarizers in that spectral region. The first experimental demonstration of entanglement came only much later, from experiments on atomic cascades. Figure 2.2a describes the radiative decay process of a

calcium atom used in Aspect's experiment [12]. By a two-photon excitation process two electrons are excited in a 4p state $|e\rangle$ with total angular momentum J = 0.

$$|e\rangle = \frac{1}{\sqrt{3}}(|+1\rangle_A |-1\rangle_B - |0\rangle_A |0\rangle_B + |-1\rangle_A |+1\rangle_B) \tag{2.5}$$

$|m\rangle_{AB}$ refers to the state of one excited electron, labeled with its magnetic quantum number m. The excited state $|e\rangle$, according to the conservation of momentum, can decay through two equivalent paths, generating a pair of photons described by a polarization-entangled state. Under the assumption of photons propagating in opposite directions, the polarization state of the system is described by the maximally entangled Bell state $|\phi^+_{RL}\rangle$.

$$|\phi^+_{RL}\rangle = \frac{1}{\sqrt{2}}(|L\rangle_A |L\rangle_B + |R\rangle_A |R\rangle_B) = \frac{1}{\sqrt{2}}(|H\rangle_A |H\rangle_B - |V\rangle_A |V\rangle_B) \tag{2.6}$$

$|L\rangle_{AB}$ ($|R\rangle_{AB}$) refers to the left-handed (right-handed) circularly polarized photon state, while $|H\rangle_{AB}$ ($|V\rangle_{AB}$) refers to the horizontally (vertically) linearly polarized photon state.

Even if it was possible to demonstrate a clear violation of the classical limit in Bell inequalities, the difficulty of controlling a single atom and the poor collection efficiency due to the isotropic emission make this approach unfeasible for the quantum technologies.

Currently, the most common technique for generating polarization-entangled photon pairs is spontaneous parametric down-conversion [13]. This phenomenon takes place when a strong laser beam is shone into a non-linear crystal and two photons of lower energy are generated from the pump photon. The process is an example of three wave mixing, a non-linear response of the material to an electric field, which is related to the second-order susceptibility tensor of polarization. Since the mechanism relies on an optical nonlinearity, and the external electric field is usually orders of magnitude weaker as compared to atomic electric fields, its probability cross-section is low. In addition to that, the phase-matching conditions must be satisfied, that are the energy and momentum conservation of the photon in the crystal. Given the anisotropy of the refractive index, these conditions are usually satisfied under specific circumstances, when birefringence

compensates for dispersion.

There are a few different schemes for generating entangled photons with this mechanism, one of the most relied on is the non-collinear type II phase matching process [52]. The principle of operation is illustrated in Fig. 2.2b. Down-converted photons are emitted in cones of opposite polarization that cross each other along two lines. A photon collected from one of the two intersection points has an individual polarization state which is not known a priori, but must be opposite to the one of the other phonon generated during down-conversion. Therefore, the photon pair is described by a two-qubit entangled state of the form $1/\sqrt{2}\left(|H\rangle_A |H\rangle_B + e^{i\alpha} |V\rangle_A |V\rangle_B\right)$.

The phase α can be willingly controlled with an additional birefringent phase shifter. If also a half-wave plate is placed in one collection path, any of the four Bell states can be fabricated.

The entangled photon sources by parametric down-conversion are relatively easy to set up, operate with high spectral stability, and yield a much higher brightness as compared to atomic cascades, mainly due to the directionality of the emission. Despite the many advantages, a couple of drawbacks limit the potential application of this technology, namely the poor scalability and the impossibility to generate photon pairs on demand. The latter hurdle is a fundamental one, because the down-conversion process is probabilistic and can also produce zero or two photon pairs [53]. This results in a trade-off between the brightness of the source and the necessity to keep the probability of two pair emission negligible. This drawback can be alleviated by combining heralded single photon sources with active multiplexing [54]. Alternatively, some quantum communication protocols can by implemented without the need for a deterministic source, provided that photons have longer coherence times than the response time of the detectors [55].

2.3 Polarization-entangled photon pairs from quantum dots

A viable solution to the issue of multi-photon emission is offered by a different physical mechanism, namely the radiative recombination of an exciton in a quantum dot. Semiconductor quantum dots are nanostructures able to

spatially confine electrons and holes and are characterized by discrete energy levels (see Sec. 3.1 and 3.2 for an in-depth introduction to the electronic structure of quantum dots), therefore behaving as artificial atoms.

Thanks to the Pauli exclusion principle, which limits the occupation number of the lowest lying conduction and valence confined levels, and to the internal radiative efficiency close to one, semiconductor quantum dots behave as excellent single-photon emitters.

Single-photon emission purity can be quantified using the second-order autocorrelation function of light $g^{(2)}(\tau)$ [42].

$$g^{(2)}(\tau) = \frac{\langle E^*(t)E^*(t+\tau)E(t+\tau)E(t)\rangle}{\langle E^*(t)E(t)\rangle\langle E^*(t+\tau)E(t+\tau)\rangle} = \frac{\langle I(t)I(t+\tau)\rangle}{\langle I(t)\rangle\langle I(t+\tau)\rangle} \tag{2.7}$$

The condition that one photon at most can be emitted by the source in a given time-bin translates in complete anti-bunching at zero-delay in the autocorrelation function, that is $g^{(2)}(0) = 0$. This property can be experimentally estimated with coincidence measurements in a Hanbury Brown–Twiss setup, as it will be described in Sec. 4.2.4.

High single-photon purity can be easily achieved in high-quality quantum dots under (quasi-)resonant excitation [56, 57]. This asset represents a major advantage with respect to spontaneous parametric-down conversion and leads up to on-demand operation.

In practice, an additional hurdle precluding this objective is set by the poor collection efficiency. The limitation is related to the non-directional emission and the total internal reflection caused by the high refractive index of the semiconductor material, and it is not a fundamental one. In fact, there are effective strategies to maximize the extraction of light from a semiconductor, such as integration in an optical waveguide or a resonant microcavity [23]. The latter, in particular, has been demonstrated able to achieve a higher emission rate of indistinguishable single photons as compared to parametric down-conversion sources [58, 59].

Moreover, the fabrication of III-V epitaxial semiconductor quantum dots can take advantage of the already existing technological platform for the optoelectronics industry and holds the potential for scaling down the size of devices.

Quantum dots are able to generate polarization-entangled photon pairs

by means of the biexciton-exciton cascade [25, 60]. In fact, the proposed approach has strong similarities with the already discussed radiative cascade in Ca atoms. If two electron-hole pairs are excited inside the quantum dot, a biexciton state is formed. The lowest bound state of the biexciton has total angular momentum J=0, similarly to the $4p^2$ excited state of the Ca atom described in Eq. 2.5.

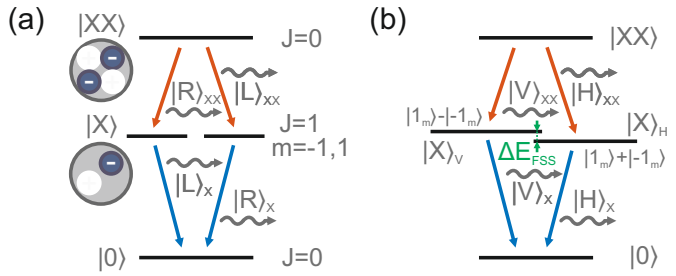

FIGURE 2.3: a) Energy diagram which describes the decay of a biexciton state in an ideal quantum dot, resulting in the emission of a pair of polarization-entangled photons. b) Energy diagram which describes the decay of a biexciton state in a realistic quantum dot, in presence of a fine structure splitting (FSS) between the two bright exciton states.

This state radiatively recombines with the emission of two photons. The process can take place through two equivalent paths, corresponding to the intermediate neutral bright exciton states with magnetic quantum number m equal to 1 and -1 (see Fig. 2.3a). Since in a usual experiment both the photons are collected from the same direction, the polarization state of the photon pair can be described by the maximally entangled Bell state $|\psi^+_{RL}\rangle$.

$$|\psi^+_{RL}\rangle = \frac{1}{\sqrt{2}}(|L\rangle_{XX}|R\rangle_X + |R\rangle_{XX}|L\rangle_X) = \frac{1}{\sqrt{2}}(|H\rangle_{XX}|H\rangle_X + |V\rangle_{XX}|V\rangle_X) \tag{2.8}$$

2.3.1 Entanglement fidelity

Despite the previously listed advantages, there are some other factors that hinder the use of semiconductor quantum dots. An important property that

defines the performance of an entangled photon source, that has not been discussed so far, is the degree of entanglement of the emitted photon pair.

Several measurements of entanglement can be used to assess the degree of entanglement of a generic two-qubit state, for example the entanglement of formation and the concurrence [61, 62]. Although, in the studied case, the ideal outcome state of the physical process is known, and a simpler figure of merit is often used, namely the fidelity f to the expected maximally entangled Bell state $\left|\psi_{RL}^{+}\right\rangle$.

$$f(|\varphi\rangle) = \left|\left\langle\psi_{RL}^{+}|\varphi\right\rangle\right|^2 \tag{2.9}$$

$|\varphi\rangle$ is a generic two-qubit pure state here.

Up to date, it has not been possible to obtain a fidelity close to 1 from a biexciton-exciton radiative cascade. The major problem is due to anisotropies in the confinement potential of a real quantum dot, which break the degeneracy of the bright exciton states through electron-hole exchange interaction (see discussion in Sec. 3.2.1). The two neutral exciton states recombine and emit photons with orthogonal linear polarization and with an energy separation ΔE_{FSS}, as sketched in Fig. 2.3b.

The presence of the fine structure splitting introduces a difference in the phase evolution of the two intermediate states of the radiative cascade [17]. This is reflected in the final polarization state which acquires a phase contribution that depends on the magnitude of the fine structure splitting and on the lifetime of the intermediate exciton state.

$$|\varphi\rangle = \frac{1}{\sqrt{2}}(|H\rangle_{XX}|H\rangle_{X} + \exp(i\Delta E_{FSS}t/\hbar)\,|V\rangle_{XX}|V\rangle_{X}) \tag{2.10}$$

An experimental measurement of fidelity is averaged over a large number of acquisitions, a mixed state which reflects the temporal distribution of the recombination events.

$$\hat{\rho} = \int_0^\infty \frac{1}{\tau_X}\exp\left(-\frac{t}{\tau_X}\right)|\varphi\rangle\langle\varphi|\,\mathrm{d}t \tag{2.11}$$

$$f = \left\langle\psi_{RL}^{+}\right|\hat{\rho}\left|\psi_{RL}^{+}\right\rangle \tag{2.12}$$

It is already evident from these expressions that a low ratio between fine

structure splitting and radiative linewidth—defined as $\Gamma_X = \hbar/\tau_X$, τ_X being the exciton lifetime—is necessary to prevent a strong reduction of the entanglement fidelity. It can easily be demonstrated [63] that any separable (i.e. unentangled) two-qubit state cannot exceed a Bell-state fidelity value of 0.5. Therefore, a figure above this threshold is required so to demonstrate the presence of non-classical correlations.

In addition to finite fine structure splitting, the intermediate exciton state of the cascade can be altered by the interaction with the environment. It was experimentally demonstrated that the entanglement degradation is not directly related to the spectral wandering, since most of the electric fields that cause it affect both the polarization states equally [17, 64]. On the other hand, spin scattering events affect the first-order cross-coherence function $g^{(1)}_{H,V}$, defined as the probability that a photon pair is emitted with a well-preserved phase between the energy eigenstates. If an estimate of the characteristic time of spin scattering τ_{SS} is known, which is shorter than the characteristic time of the specific dephasing events between the superimposed intermediate exciton-photon states, the first-order cross-coherence can be phenomenologically estimated as $g^{(1)}_{H,V} = 1/(1 + \tau_X/\tau_{SS})$.

A leading physical mechanism for electron spin relaxation is hyperfine coupling with nuclear spins [18]. It has been recently pointed out as one of the main causes for non-ideal fidelity in quantum dots with vanishing fine structure splitting [19, 20]. The interaction of the delocalized electron wave function with a large population of randomly oriented nuclear spins can be described with a Fermi contact Hamiltonian H_{hf} in first order perturbation theory.

$$H_{hf} = \sum_j A_j \left|\psi_e(\mathbf{R}_j)\right|^2 \hat{\mathbf{I}}_j \cdot \hat{\mathbf{S}} \equiv \mathbf{B}_N \cdot \hat{\mathbf{S}} \tag{2.13}$$

j is the lattice index, $\psi_e(\mathbf{R}_j)$ is the electron envelope wave function at the jth nucleus, $\hat{\mathbf{S}}$ and $\hat{\mathbf{I}}_j$ are the spin of the electron and of the jth nucleus respectively, and A_j are coefficients dependent on the electron Bloch function at the nucleus. Without entering a more detailed discussion, it is possible to notice that the nuclei act as an effective magnetic field $\mathbf{B}_N$ on the electron. The magnitude of the magnetic field is strongly dependent on the materials choice and, in particular, on the nuclear spin of the atomic components.

Recent studies alternatively suggest that excess charges in the surroundings of the quantum dot may also exert an effective magnetic field on the exciton through either direct spin coupling or fluctuating electric fields by way of the spin-orbit interaction [65].

The effects of the exciton scattering and the background light can be included as well in the density matrix of the final two-photon state introduced in Eq. 2.11, leading to an analytical expression for fidelity.

$$f = \frac{1}{4}\left(1 + \kappa g^{(1)}_{H,V} + \frac{2\kappa g^{(1)}_{H,V}}{1 + \left(g^{(1)}_{H,V}\Delta E_{FSS}\tau_X/\hbar\right)^2}\right) \tag{2.14}$$

κ is the fraction of photons generated from exciton recombination with respect to background noise and it can be inferred from autocorrelation measurements as $\kappa = 1 - g^{(2)}(0)$. Eq. 2.14 summarizes the main factors that must be controlled in order to improve the degree of entanglement provided by a polarization-entangled photon source based on a quantum dot.

2.3.2 State of the art of quantum dot sources

Several solutions for the realization of a semiconductor polarization-entangled photon source have been proposed in the literature since the first experimental demonstrations dating back to a decade ago [66, 67].

Most of the research up to date has focused on how to deal with the problem of the finite fine structure splitting. The issue strongly affects the InGaAs Stranski-Krastanow quantum dots, which have been the most investigated family of high-quality epitaxial nanostructures for single-photon studies. In that case, the energy splitting usually ranges from a few to hundreds of μeV [16, 68], as compared to a typical radiative linewidth around 1 μeV.

Even if it is possible to observe a quite low average fine structure splitting in a narrow spectral region after a high temperature post-growth annealing [69], the small fraction of emitters with a high degree of entanglement, together with the poor flexibility in the design of the nanostructures, make this approach unpractical.

In alternative, it has been demonstrated that the fine structure splitting can be reduced and possibly brought to zero by means of various external perturbations. Viable strategies include magnetic [66], electric [70], strain [30, 31] and optical [71] fields. In order to completely restore the degeneracy of the bright exciton states and to fine tune the emission energy - required for matching Rb transitions in a slow-light vapor cell, see Sec. 2.3.3 - of a generic quantum dot, the combined control over three degrees of freedom is necessary [72, 73].

Another approach consists in using a different epitaxial growth method able to tackle the origin of the finite fine structure, that is the low structural symmetry. The goal is to reliably fabricate entangled photon emitters which do not require post-growth adjustments. Most of the attempts in this direction rely on improving the in-plane symmetry of as-grown quantum dots by moving to the (111)-substrate orientation. The symmetry of a typical nanostructrure grown on a standard (100) substrate is C_{2v}, due to the different surface mobilities along the [011] and the [01-1] directions, the built-in piezoelectric fields and the anisotropies of the interface related to the orientation of the zinc-blende lattice. The choice of the (111)-orientation can improve the ideal symmetry to C_{3v}, which protects the degeneracy of the bright exciton states [74, 75].

Since InAs does not grow in the Stranski-Krastanow mode on GaAs(111), a different epitaxial technique is needed to implement this concept. During recent years several solutions have been proposed, namely droplet epitaxy (see Sec. 3.4 for a description of the technique) InGaAs [76] and GaAs [77] quantum dots, patterned InGaAs inverted nano-pyramids [78], Stransky-Krastanov GaAs nanocrystals on an unconventional InP substrate [79] and InAsP segments in InP nanowires [80].

All the materials systems listed above achieved a reduced average fine structure splitting in a range from 2 to 10 μeV. In few cases [27, 80, 81], this lead to the demonstration of the generation of polarization-entangled photon pairs on selected emitters without the need for temporal post-selection or tuning by external fields. Nonetheless, only a small minority of the quantum dots on each sample is able to emit photon pairs with an entanglement fidelity above the classical limit. The highest fraction of entanglement-ready emitters was reported for a technique with high site and shape control [81], but it still did not exceed 15%.

On the other hand, the highest value of entanglement fidelity—86%—was reported for GaAs quantum dots grown by droplet epitaxy. This result has been confirmed by recent studies on GaAs/AlGaAs quantum dots fabricated with droplet etching, that achieved record values of fidelity [19] and yield of entanglement-ready emitters [20]. It has been suggested that such an improvement is related to the lower magnetic moment of Ga as compared to In, which strongly reduces the magnitude of the fluctuating nuclear magnetic field and, consequently, the exciton dephasing by spin scattering.

2.3.3 Integration with atomic media for photon storage

Another requirement for a practical solid-state entangled photon source, stated in the initial section of this chapter, is the compatibility with efficient single-photon detectors and with a device for storing polarization qubits.

While the development of an efficient quantum memory is a large research field on its own [82, 83], up to date the main candidate technology for the storage of the state of a single photon is light slow-down in an atomic vapor [21, 84, 85].

Under the assumption of moderate pulse distortion and absorption in the optical medium, the propagation speed of light can be described by its group velocity v_g [86, 87].

$$v_g = \frac{c}{n + \omega(\mathrm{d}n \,/\, \mathrm{d}\omega)} \tag{2.15}$$

A simple way to implement the technique and reduce group velocity relies on the basic principle of tuning the energy of the photon between two transitions separated by a small hyperfine splitting in a warm atomic cloud. In this spectral interval, the refractive index n of the medium steeply increases and a group velocity several order of magnitudes lower than the vacuum speed can be achieved.

The large normal dispersion of the atomic cloud can be quantitatively modeled by assuming a simple double Lorentzian resonance for the electric susceptibility χ—which directly returns the index of refraction as $n = \mathrm{Re}\{\sqrt{1+\chi}\}$.

$$\chi \propto \frac{g_1}{\omega_1 - \omega - i\gamma} + \frac{g_2}{\omega_2 - \omega - i\gamma} \tag{2.16}$$

g_1 and g_2 are the transition strengths, ω_1 and ω_2 are the frequencies, 2γ is the homogeneous linewidth relative to the two atomic transitions.

Frequency detuning, either by means of temperature control, optical pumping or application of an electric field, can be used to vary the delay of the optical pulse inside the vapor cell.

The GaAs/AlGaAs choice of materials, identified in the previous section as optimal for generating photon pairs with a strong degree of entanglement, is practical also from the point of view of compatibility with the technologies for a semiconductor-atomic hybrid repeater capable to transfer entanglement over long distances. In addition to working in the spectral range of high efficiency Si-based single-photon detectors, GaAs quantum dots have already been interfaced with Rb-based vapor cells [22].

Time delaying of single photons was successfully demonstrated by tuning the emission wavelength of GaAs nanostructures at an energy between the D_2 absorption lines of ^{87}Rb. These transitions are at a typical wavelength of 780 nm and are separated by an hyperfine splitting of 28 μeV [88]. The bandwidth of the slow-down effect is large enough to tolerate for small spectral wandering in the quantum dot emission and the polarization state of the photon is preserved.

Consistently, the first demonstration of slowing down a photon from an entangled pair emitted from an InAs quantum dot through a Cs vapor cell showed no negative effect on the degree of entanglement [30]. The study of this kind of semiconductor-atomic hybrid systems is still in its infancy and up to now only small time delays of the order of 10 ns have been tested. The storage time for the polarization state of a photon in a room-temperature atomic cloud can currently be extended up to around 20 μs [85].

Chapter 3

Introduction to semiconductor quantum dots

3.1 Electronic structure

Quantum dots are semiconductor crystals of nanometer size, whose carrier motion is confined in three dimensions. Spatial confinement below a certain length scale dramatically affects the electronic and optical properties of the material, due to an effect known as quantum confinement. This phenomenon can be qualitatively explained as related to the Heisenberg uncertainty principle. By enforcing localization on a free particle, higher uncertainty on its momentum is introduced. As a result, also its average kinetic energy is increased and the effect becomes relevant when the confinement energy exceeds the thermal energy associated to motion in the direction of confinement. Therefore, quantum size effects are observed when the length of confinement is comparable or below the de Broglie wavelength for thermal motion λ_{dB} [89].

$$\lambda_{dB} = \frac{h}{\sqrt{3mk_BT}} \tag{3.1}$$

h is the Planck constant, m is the mass of the particle and T is the temperature. In this thesis I am focusing on quantum dots made out of GaAs,

a III-V direct band gap semiconductor with wide application in optoelectronics. Using the estimate of effective mass from Ref. [90], the electron thermal de Broglie wavelength is approximately 24 nm at room temperature, hence typical length scales of quantum dots fall into the domain of nanotechnology.

The carriers in a quantum dot are confined by the presence of a potential well. In epitaxial quantum dots a potential barrier for electrons and holes is implemented by fabricating a heterostructure between two materials with band alignment of type I. In other words, the minimum of the conduction band and the maximum of the valence band of the included material (well) fall lower and higher respectively in energy as compared to the ones of the surrounding material (barrier). Figure 3.1a schematically illustrates this concept for the case of a GaAs/AlGaAs potential well, which corresponds to the system studied in this work.

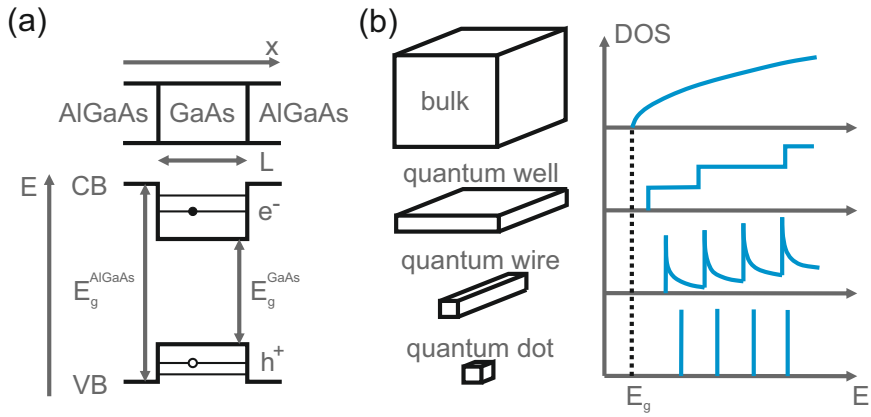

FIGURE 3.1: a) Sketch of a one-dimensional potential well with discrete bound energy levels, formed by type I band alignment in a GaAs/AlGaAs heterostructure. b) Density of states of an electron gas as a function of confinement dimensionality.

The simplest model for describing the energy levels of a confined particle is the infinite potential well, also known as particle in a box [91]. The time-independent Schrödinger equation in one dimension reported in Eq. 3.2 simply reduces to the free particle equation in a spatial interval $0 < x < L$,

where L is the length of confinement.

$$-\frac{\hbar^2}{2m^*}\frac{\mathrm{d}^2\psi}{\mathrm{d}x^2} + V(x)\psi(x) = E\psi(x) \tag{3.2}$$

The solutions are sinusoidal wave functions which must vanish in the barrier region and obey the boundary conditions of a stationary wave with nodes in $x = 0, L$.

$$\phi_n(x) = \sqrt{\frac{2}{L}}\sin(k_n x) = \sqrt{\frac{2}{L}}\sin\Big(\frac{n\pi x}{L}\Big) \tag{3.3}$$

$$E_n = \frac{\hbar^2\pi^2 n^2}{2m^* L} \tag{3.4}$$

n is an integer quantum number that labels the confined states of the well.

Despite being very basic and qualitative, this model captures two essential features, summarized in the energy spectrum E_n of Eq. 3.2, namely the discretization of the energy levels and the presence of a zero-point energy. As already mentioned, a finite confinement energy is consistent with the uncertainty principle and it increases as the confinement length L is reduced.

The functional form of the density of states depends in general on the dimensionality of the free motion of the carriers [92], as summarized in Fig. 3.1b for the bulk and different categories of nanostructures. Quantum dots are also defined as artificial atoms, because of the discrete nature of their energy levels.

3.1.1 Effective-mass single-band model

The concept of a potential well model can be adapted to the case of the electronic structure of a semiconductor quantum dot and adequately extended in order to provide a quantitative, yet approximate, description.

The electronic structure of a localized potential V_{well} added to the periodic Hamiltonian H_{crys} of a crystal is a formidable problem, whose exact solution is usually beyond reach, even with numerical methods.

$$[\hat{H}_{crys} + V_{well}(\mathbf{R})]\psi(\mathbf{R}) = E\psi(\mathbf{R}) \tag{3.5}$$

A couple of reasonable assumptions can be adopted in order to simplify the equation.

First, it is supposed that the eigenfunctions of the complete problem can be written as a linear combination of wave functions of the unperturbed crystal coming mainly from one band. Since band mixing is neglected, this is called single-band approximation.

The second assumption, which is also often used to model many physical properties of the bulk material, is the effective-mass approximation. The hypothesis states that the detailed band structure of the semiconductor can be disregarded, and only the energy dispersion near the conduction band minimum and the valence band maximum is taken into account.

It can be easily shown [91] that if the bottom of the band is in Γ—a justified statement for GaAs and AlGaAs with Al content below 45%—the wave function can be reduced to a Bloch function of the perfect crystal $\phi_{n0}(x)$ (n and 0 being band and momentum index respectively), modulated by the so called envelope function $\chi(x)$.

$$\psi(x) = \sum_n \int_{-\pi/a}^{\pi/a} \tilde{\chi}_n(k)\phi_{nk}(x)\frac{\mathrm{d}k}{2\pi} \approx \phi_{n0}(x)\chi(x) \tag{3.6}$$

Consequently, the problem can be reduced to a Schrödinger equation for the envelope function alone with an effective Hamiltonian.

$$\left[E_{crys,n}\left(-i\frac{\mathrm{d}}{\mathrm{d}x}\right) + V_{well}(x)\right]\chi(x) = E\chi(x) \tag{3.7}$$

$E_{crys,n}(k)$ is the full dispersion curve for the band n, which can be simplified once again with the help of the effective-mass approximation and reduced to a parabolic dispersion around Γ. The information on the curvature of the band is included inside the effective mass of the carrier $m_{e/h}$.

$$\left[-\frac{\hbar^2}{2m_{e/h}m_0}\boldsymbol{\nabla}^2 + V_{well}(x)\right]\chi(x) = (E - E_{c/v})\chi(x) \tag{3.8}$$

This equation can be used to describe an heterostructure by choosing V_{well} equal to the band offset, as long as the momentum boundary conditions are corrected for keeping into account the different effective mass values. An

electron (hole) in a quantum dot can be modeled as a particle with effective mass m_e (m_h) in a finite constant-potential well equal to the conduction (valence) band offset. In particular, the maximum of the valence band can be estimated using the heavy-hole effective mass, because confinement energy lifts the degeneracy between light-hole and heavy-hole states, which are degenerate in Γ in the unstrained bulk material instead.

The constant-potential approximation is quite accurate for GaAs/AlGaAs heterostructures with a sharp interface, given the similar lattice constant between the two alloys and the absence of strain. As an opposite example, in InGaAs/GaAs Stranski-Krastanow quantum dots, anisotropic strain distribution and random alloying can introduce local variations in the potential.

While the model presented above can give approximate estimates of the number of bound states and their confinement energy, the single-band assumption can be quite limiting if higher accuracy is required or finer effects such as piezoelectric fields are investigated. Band mixing between the bulk s-like conduction band and the three valance bands formed from bonding p orbitals, namely heavy-hole, light-hole and split-off, is often non-negligible. In particular, heavy-hole light-hole mixing can be an important effect given the relatively small energy separation between the two bands [93]. Approaches that maintain the effective-mass approximation but extend the single-band model by including coupling between a small number of relevant bands of the host crystal constitute the $\mathbf{k} \cdot \mathbf{p}$ method [94].

More sophisticate computational tools that relax the effective-mass assumption are available such as atomistic pseudopotential calculations [95], but at the cost of high computational complexity, and they still rely on less immediate empirical approximations [96].

3.2 Excitonic complexes

In the previous section, I presented a brief introduction to the electronic structure of a quantum dot. The confined motion of an electron or a hole was treated within the single-particle picture. However, since optical absorption and radiative recombination involve an electron-hole pair, modeling the interaction between quantum dot states and the radiation field requires to consider configurations with more than a single charged particle.

A more complete model requires to keep into account the Coulomb interaction between the confined electrons and holes. Each pair of carriers with charge e at a distance $\left|\mathbf{r}_i - \mathbf{r}_j\right|$ contributes to the total energy of the system with an electrostatic coupling term W_{ij}.

$$W_{ij}(\mathbf{r}_i, \mathbf{r}_j) = \frac{1}{4\pi\epsilon_r\epsilon_0} \frac{e_i e_j}{\left|\mathbf{r}_i - \mathbf{r}_j\right|} \tag{3.9}$$

ϵ_r is the dielectric constant of the material and quantifies its electrostatic screening.

Considering an electron-hole pair, the interaction is attractive, and the energy of the system is lowered, forming a bound state called neutral exciton. The binding energy of a free exciton, defined as the energy necessary to ionize it to a non-correlated electron-hole couple, in a bulk III-V semiconductor is usually smaller than the thermal energy at room temperature. The electron and the hole are delocalized over several lattice cells, and their binding energy $E_{b,X}$ can be estimated in Wannier approximation, that is as a hydrogen-like atom using effective masses and a renormalized dielectric constant.

$$E_{b,X}^{Bohr}(n) = -\frac{\mu}{m_0} \frac{1}{\epsilon_r^2} \frac{R_N}{n^2} \tag{3.10}$$

R_H is the Rydberg energy of the hydrogen atom (13.6 eV), μ is the reduced mass of the system and n is an integer quantum number. In the case of GaAs, the binding energy of the first bound state is only 4.2 meV, which corresponds to a Bohr radius of 13 nm.

When the carriers are confined in a heterostructure on a length scale smaller than the extension of the free exciton, their Coulomb interaction changes accordingly. However, for quantum dots in a strong confinement regime, size effects on the exciton binding energy in GaAs are only a correction as compared to the quantum confinement energy. This justifies the use of a single-particle picture for rough estimates of the transition energy of exciton states in a quantum dot.

Nonetheless, the exciton picture is fundamental to describe the electronic fine structure of the electron-hole pair and their correlated dynamics.

As explained in the previous section, the electronic structure of a quantum dot is characterized by discrete energy levels, and they can be labeled

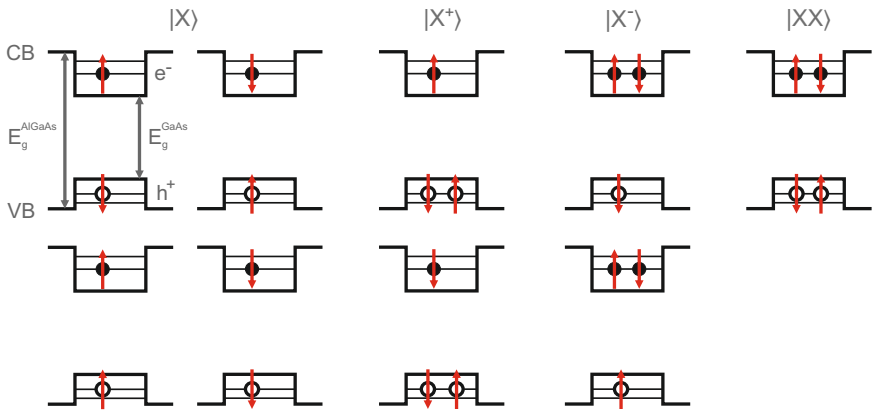

FIGURE 3.2: Possible spin configurations of the neutral exciton (X), the singly charged excitons (positive X^+ and negative X^-) and the biexciton (XX) in the s-shell of a GaAs/AlGaAs quantum dot.

in an atomic fashion. A ground state confined exciton is formed by carriers in the lowest lying level, also defined as s-shell. Since electron and holes are fermions and obey the Pauli exclusion principle, only a finite number of carrier configurations is available. They are illustrated in Fig. 3.2 together with the possible combinations of spin states. A bound state composed of two, three or four charge carriers is called neutral, charged or bi- exciton respectively.

The direct term of Coulomb interaction introduces a binding energy for the electron-hole pair. The presence of an extra charge creates a strongly interacting few-body system and renormalizes this binding energy. In a simple mean field picture, the electron is more delocalized thanks to the lighter effective-mass and the spatial charge distribution of the electron-hole pair acts as an attractive potential for an additional electron, repulsive for a hole [97–99]. This would lead to a bound negatively charged exciton and to an unbound positively charged exciton, but the inter-particle correlation is non-negligible, especially for smaller quantum dots. The sign of the binding energy changes depending on the specific materials choice and geometry. The same considerations are valid for the sign of the binding energy of the

two electron-hole pair configuration. In the case of GaAs/AlGaAs quantum dots, the biexciton state is usually bound and the binding energies of these few-particle excitonic complexes fall in the range of few meV [99, 100].

3.2.1 Exciton fine structure

A neutral exciton can be found in four different dispositions of the spins, which are degenerate if only the direct term of Coulomb interaction is considered. Coulomb exchange interaction E_{exc} couples the spins of the electron and the hole and induces the presence of a fine structure [15, 16].

$$E_{exc} = \frac{e^2}{\epsilon_0 \epsilon_r} \int\int \mathrm{d}^3 r_e \, \mathrm{d}^3 r_h \, \Psi_X^*(\mathbf{r}_e, \mathbf{r}_h) \frac{1}{|\mathbf{r}_e - \mathbf{r}_h|} \Psi_X(\mathbf{r}_e, \mathbf{r}_h) \tag{3.11}$$

$\Psi_X(\mathbf{r}_e, \mathbf{r}_h)$ is the two-particle exciton wave function, $\mathbf{r}_e$ and $\mathbf{r}_h$ are the spatial coordinates of the electron and the hole respectively.

In typical epitaxial quantum dots, the main confinement direction coincides with the growth direction z, which is also the symmetry axis of the system, if present. Therefore, the projection of angular momentum along the z axis is the good quantum number to represent the splitting between light- and heavy-hole states. In first approximation, the valence band maximum is composed of heavy-hole states with spin $J_h = 3/2$, $J_{h,z} = \pm 3/2$, whereas the spin of the electron is defined as $S_e = 1/2$, $S_{e,z} = \pm 1/2$. The spin state of the bound exciton can be written as a combination of the single-particle spin states of the heavy hole and the electron, leading to four states with different projection of angular momentum $M = S_{e,z} + J_{h,z}$.

Due to the conservation of angular momentum, only states with $|M| = 1$ can absorb or emit a photon. These excitons are denoted as bright, whereas the states with $|M| = 2$ that do not couple to the radiation field are known as dark excitons.

In order to describe the fine structure of the heavy-hole exciton states, a parametric Hamiltonian H_{exc} can be written on the basis of symmetry considerations [15, 101].

$$H_{exc} = -\sum_{i=x,y,z} \left(a_i J_{h,i} S_{e,i} + b_i J_{h,i}^3 S_{e,i} \right) \tag{3.12}$$

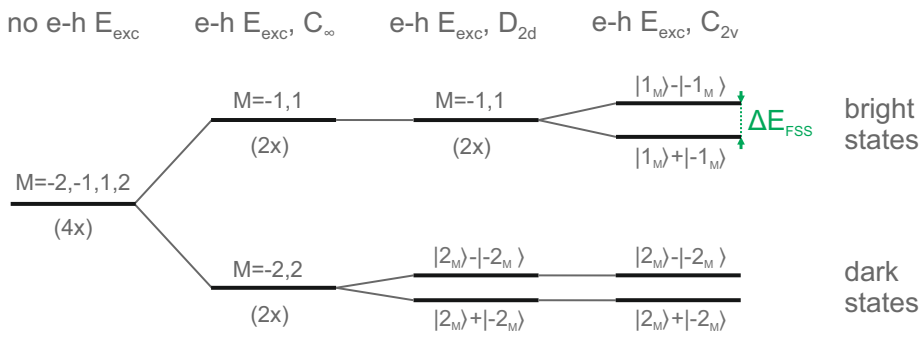

FIGURE 3.3: Schematic energy diagram that represents the refinement of the fine structure of a heavy-hole neutral exciton as electron-hole exchange interaction and lowered symmetry are included in the model.

a_i and b_i are generic spin-spin coupling constants and depend on the geometry of the quantum dot. By solving the Hamiltonian in Eq. 3.12 for eigenstates and keeping into account symmetry constraints on the coefficients a_i and b_i, it is possible to deduce some important qualitative features about the exciton fine structure.

The degeneracy between the bright and dark excitons is removed by exchange interaction even in the idealized case of cylindrical symmetry C_∞ [16], which ignores the crystal atomistic symmetry. If the crystal zincblende structure is kept into account while retaining a quantum dot shape with ideal in-plane rotational invariance, as in the case of the D_{2d} global symmetry, a small energy difference is introduced between the two dark excitons $M = \pm 2$, whereas the two bright excitons $M = \pm 1$ remain degenerate energy eigenstates.

However, when an in-plane asymmetry is present, so that $b_x \neq b_y$, as in the commonly reported case of a global C_{2v} symmetry, also the degeneracy between the two bright exciton states is lifted. The refined fine structure is sketched in Fig. 3.3. The angular momentum is not necessarily a good quantum number in absence of rotational symmetry, and the two energy eigenstates are linear superpositions of the states $M = \pm 1$, specifically their symmetric and antisymmetric superpositions. The radiative recombination

of these two states leads to the emission of photons with orthogonal linear polarization.

The bright exciton fine structure splitting depends on the second term of the Hamiltonian in Eq. 3.12 and its amplitude should be smaller as compared to the one which separates bright and dark states. This expectation is met by typical data from GaAs/AlGaAs dots, in which the dark exciton states stay around 200 μeV below the bright exciton ones [102], whereas the bright exciton fine structure splitting varies between few and a hundred of μeV [103].

On the other hand, exchange interaction in charged excitons induces no fine structure, since the two hole (X^+) or electron (X^-) pair is a spin singlet. This prediction is valid in the strong confinement regime, when the two wave functions composing the spin-singlet state have overlapping spatial distribution.

Similarly, the biexciton is a spin-singlet state and shows no exchange-induced splitting.

3.3 Single dot photoluminescence

While discussing the electronic structure of a quantum dot I have already commented on its influence on the optical properties of the system. This interplay underlies the operation of any optoelectronic device as well as single- and entangled photon emission, the object of this thesis.

Light emission from a semiconductor can be triggered by a high-energy electron beam (cathodoluminescence) or an electric current (electroluminescence), but in this work I am focusing on photoexcitation. Photoluminescence is the physical phenomenon of light emission from matter that takes place when the energy for the process is provided by an optical excitation mechanism. According to the quantum mechanical interpretation [104], if a photon impinges on a semiconductor material and has an energy higher than its bandgap, it gets absorbed, transfers its energy to an electron in the crystal potential and creates an electron-hole pair. The photoexcited carriers, after thermalization by means of interactions with lattice vibrations or other carriers, can undergo radiative recombination, a process by which the system returns to the electronic ground state with the related emission of a photon.

Even though electrical pumping is probably more desirable in view of the application in compact devices [60], photoluminescence is a valuable experimental tool that allows to access information on the energy levels and the recombination dynamics and does not require any particular sample preparation. Moreover, it provides better control on the energy and the polarization of the injected carriers.

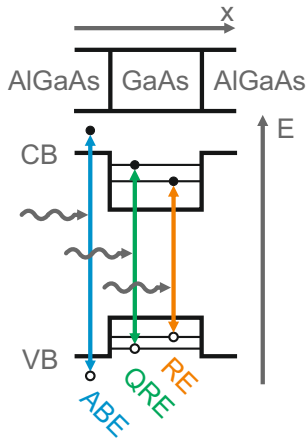

FIGURE 3.4: Different excitation schemes illustrated with the help of the energy level sketch from Fig. 3.1a. In detail, above-barrier excitation (ABE), quasi-resonant excitation in the p-shell (QRE), and resonant excitation in the s-shell (RE).

Different strategies to populate a quantum dot with an electron-hole pair can be pursued. The simplest approach employs photons with an energy above the barrier bandgap. In this way, most of the electron-hole pairs are generated in the barrier in a highly non-equilibrium state. These carriers lose their excess energy, first, mainly by electron-electron interaction and, then, by electron-phonon coupling. While decaying towards the minimum (maximum) of the conduction (valence) band, the carriers can be captured by a quantum dot acting as a potential well. Thermalization to the lowest lying levels of the quantum dot usually occurs on a short time scale with respect to interband transitions, of the order of 10–100 ps [105].

A fraction of the carriers interacts instead with defects in the barrier material, either non-radiative recombination centers or charge traps. In the latter case, they are responsible for fluctuating electric fields that affect the energy of excitons confined in the quantum dot. This behavior is a major cause for line broadening in the emission spectrum, an effect known as spectral diffusion [106–108].

The mechanism of above-barrier excitation does not deterministically create a single confined electron-hole pair, but rather the occupation number of the quantum dot levels is described by a Poissonian distribution [109]. In this way, several excitonic complexes are generated, starting from the possible combinations in the s-shell presented in Sec. 3.2. The probability to observe the radiative recombination of a specific excitonic complex can be controlled by changing the excitation power, but without the possibility to select a single optical transition.

Another problem related to non-resonant excitation is time-jittering in the photon emission event under pulsed optical pumping. This is caused both by the thermalization processes and the possibility of cascaded recombination from multiexcitonic states. However, while the latter process can be detrimental for the implementation of a deterministic source of indistinguishable photons, it is conversely essential to observe the emission of polarization-entangled photons through the physical mechanism of the biexciton-exciton radiative decay, as previously illustrated in Sec. 2.3.

The drawbacks listed above—which similarly affect electroluminescence from a p-i-n structure—are mitigated by decreasing the energy of the pump photons below the barrier bandgap so to match absorption resonances of the quantum dot states. An electron-hole pair can be generated into a higher shell of the quantum dot—a technique known as quasi-resonant excitation—from where it relaxes to the s-shell with high quantum efficiency. Direct excitation into the s-shell guarantees total coherent control of the exciton state and minimum time-jittering, but filtering the back-scattering of the laser is challenging. An alternative solution consists in resonantly exciting the biexciton-exciton cascade through two-photon absorption. As discussed more in detail in Sec. 5.2.1, in this way a coherent preparation of the biexciton state is achieved while allowing for spectral filtering of the laser light.

In the final step of the photoluminescence process an electron-hole pair

radiatively recombines through the physical mechanism of spontaneous emission. A general expression for the radiative transition rate $\gamma_{i\to j}$ is given by the Fermi's golden rule under the assumption of dipole interaction [92].

$$\gamma_{i\to j} = \frac{2\pi}{\hbar}|\langle j| - \mathbf{p}_e \cdot \mathbf{E_0}\,|i\rangle|^2 g(\hbar\omega_{ij}) \tag{3.13}$$

$|i\rangle$ and $|j\rangle$ are the wave functions of the initial and final state respectively, $g(\hbar\omega_{ij})$ is the density of state of the photon field at the transition energy (keeping into account the discrete electronic structure of the quantum dot), $\mathbf{E_0}$ is the electric field amplitude at the point of the quantum dot and $\mathbf{p}_e = -e\cdot\mathbf{r}$ is the electric dipole moment operator.

The matrix element of the dipole operator poses some constraints, known as selection rules, on the parity and on the angular momentum quantum numbers of the initial and final state in order to have a non-vanishing transition rate. I implicitly made use of the rules $\Delta J = 0, \pm 1$ ($J = 0 \to 0$ forbidden) and $\Delta S = 0$ in Sec. 3.2.1, in particular to label bright and dark excitons accordingly to their interaction with the radiation field.

Strong interaction with the radiation field is a peculiar asset of quantum dots, thanks to the discrete density of states and to the spatial overlap of the confined electron and hole wave functions, which enhances the optical transition strength with respect to the bulk material.

This property is often evaluated in terms of the oscillator strength f. It is defined as the ratio of the quantum mechanical transition rate of the system to the decay rate of a classical single electron oscillator emitting at the same energy $\hbar\omega_{ij}$. It can be demonstrated that, in the case of an exciton recombining in a quantum dot in a strong confinement regime, this quantity is directly related to the overlap of the electron and hole envelop functions $|\chi_{e/h}\rangle$ [32].

$$f = \frac{2m_0\omega_{ij}}{\hbar}|\langle j|\,\mathbf{r}\,|i\rangle|^2 = \frac{E_p}{\hbar\omega_{ij}}|\langle\chi_h|\chi_e\rangle|^2 \tag{3.14}$$

m_0 is the rest mass of the electron, E_p is the Kane energy and contains the contribution from the Bloch states of the crystal.

In small nanostructures where the electron-hole overlap is maximized, fast radiative recombination is expected [110]. According to Eq. 3.14, an oscillator strength up to 18 can be observed for a GaAs quantum dot emitting

at 780 nm. For large quantum dots, with a size greater than the exciton Bohr radius, even larger values can be observed due to the coherence volume effect, leading to the phenomenon of giant oscillator strength [111, 112].

These considerations lead to typical exciton lifetimes in quantum dots from few hundreds of ps to a couple of ns. As a consequence of the large radiative decay rate γ_{rad}, the impact of non-radiative recombination (γ_{nrad}) can be reduced in quantum dots, resulting in high quantum efficiency η_{IQE}.

$$\eta_{IQE} = \frac{\gamma_{rad}}{\gamma_{rad} + \gamma_{nrad}} \tag{3.15}$$

The strong spatial confinement of the carriers in a defect-free crystalline region also strongly limits the number of non-radiative decay channels available, especially if thermal escape from the quantum dot is quenched. In fact, close-to-one quantum efficiency is achieved in high-quality epitaxial III-V quantum dots under resonant excitation at cryogenic temperatures [23].

Given the high internal quantum yield, the main bottleneck on the brightness measured in experiments is related to the problem of light collection from the semiconductor. The emission of photons from a quantum dot is essentially non-directional, and, when the dot is embedded in a single thick barrier layer, the fraction that exits from the top semiconductor-air interface is limited by total internal reflection. Given the large refraction index characteristic of semiconductor materials—3.7 for GaAs at 780 nm—only about 2% of the emitted radiation escapes [113]. This figure can be drastically increased if the quantum dot is embedded in an optimized structure for light collection, such as an optical microcavity, a waveguide [23] or a nanowire [114].

3.4 Droplet epitaxy

With the previous sections I introduced the peculiar physics of three-dimensional confinement in lateral semiconductor nanostructures with particular regard to electronic and optical properties. Band-gap engineering, increased density of states, and excitonic effects are all appealing features for a new generation of optoelectronics devices. Possibly the main challenge in this direction resides in the fabrication of the quantum dots. Many parameters,

such as size, density and uniformity, need to be controlled, a high-level optical and structural quality has to be achieved, and the materials have to be chosen accurately in order to conciliate compatibility with the growth technique, requirements for the emission wavelength and an adequate confinement potential for the carriers.

Even if several strategies can be used to localize carriers in semiconductors—e.g. chemical colloidal synthesis, top-down lithography and etching, gate-defined electrostatic potentials—self-assembled epitaxial systems provide the best results in terms of optical properties.

Probably the most studied approach in this research field focuses on the spontaneous formation of crystalline three-dimensional islands in the Stranski-Krastanow growth mode [115]. This strain-driven mechanism is compatible with standard molecular beam epitaxy technology and leads to excellent crystalline and optical quality. However, it is restricted to only specific heterostructures with large lattice mismatch, such as InAs/GaAs (100) or Ge/Si (100).

The fabrication method used in this work, droplet epitaxy, allows to overcome this hurdle and produce nanometer-sized crystalline inclusions of lattice-matched materials.

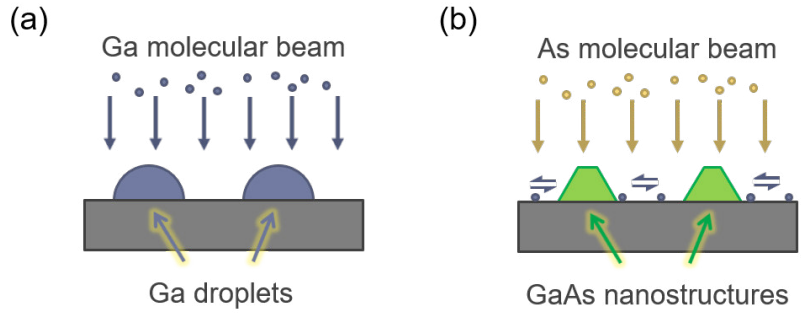

FIGURE 3.5: Synthetic depiction of the two fundamental deposition steps of droplet epitaxy. a) Formation of metallic nanodroplets under a group III (Ga) flux. b) Exposure to an intense group V (As) molecular beam and crystallization into an ordered III-V (GaAs) alloy.

The technique was developed by Koguchi and co-workers in the early

Nineties [116, 117]. As in the case of Stranski-Krastanow growth, it relies on a simple self-assembly process and is compatible with a standard molecular beam epitaxy setup. The basic procedure of operation is illustrated in Fig. 3.5. The main concept behind droplet epitaxy consists in dividing the deposition in two phases and supplying separately the group III and V molecular beams to the surface.

In the first step, the substrate is irradiated with a molecular beam of group III material, namely Ga, In or Al. After creating a group III-rich reconstruction, an additional sub-monolayer quantity of material is provided, leading to the spontaneous formation of liquid droplets with typical base radius in the 10–100 nm range. The size distribution and the spatial density of the droplets can be controlled by varying the substrate temperature, the flux and the total quantity of material employed. A wide space of deposition parameters can be explored (temperatures from 150 to 450°C, fluxes from 0.01 to 1 ML/s), offering high flexibility in engineering the outcome of the process. In particular, the density can be tuned from 10^8 to 10^{11} cm^{-2}, targeting applications for which either high coverage is required or single emitters must be addressed individually. While a certain degree of size dispersion is unavoidable in self-assembly growth, this effect can also be managed during this phase (see Sec. 5.1.3).

After the droplets are deposited, the group III cell is shuttered, and they are exposed to a flux of group V material, As, P, Sb, and N being potentially viable choices. During this phase, in certain conditions the formation of three-dimensional nanocrystals of the III-V compound is observed. Group V atoms from the molecular beam can be directly incorporated into the liquid droplet and, then, crystallize by supersaturation and precipitation at the droplet-substrate interface.

The droplet acts as a nanoscale reservoir of group III atoms and determines the volume of the quantum dot, which will occupy its same position at the end of the process. The chosen growth parameters, namely the substrate temperature and the group V flux, dictate the final morphology of the nanostructures. In this way, droplet epitaxy achieves the possibility to independently control size, density and shape of the quantum dots and provides a unique degree of flexibility in the design of a self-assembly process.

The conditions for obtaining crystallization of GaAs in three-dimensional islands on top of an AlGaAs(100) surface were found by Watanabe, Koguchi

and Gotoh in Ref. [28]. A low substrate temperature (around 200°C) and a high As beam equivalent pressure (around 10^{-5} torr) are required in order to contain Ga surface diffusion and maintain the droplet lateral size after crystallization.

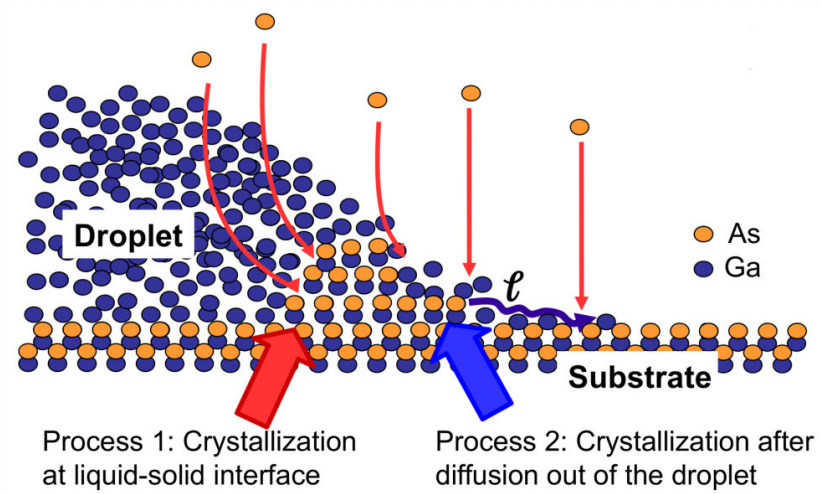

FIGURE 3.6: The diagram outlines the two competing mechanisms which lead to As incorporation. Image taken from Ref. [29].

The crystallization dynamics has been thoroughly investigated on (100) substrates and island formation has been observed up to 250°C [29] during exposure to the As flux. Above this temperature, As incorporation in the droplet and the consecutive crystallization at the liquid-solid interface, starting from the triple point, ceases to be the dominant mechanism. Due to the stark increase in Ga diffusivity, As impinging on the surface is more likely to bind to Ga adatoms outdiffusing from the droplet, leading to planar growth (see Fig. 3.6 for a sketch of the two possible growth pathways).

The shape of the quantum dots depends on the detailed kinetics of the process. In this way, there are a few degrees of freedom for the design of the morphology of the islands. Several shapes have been obtained in the literature by simply changing the growth parameters during the exposure of the droplet to the As flux. Among the reported shapes are truncated

pyramids with circular base and aspect ratio from 0 to 0.5 [29], rings [118], multiple concentric rings [119], and planar quantum molecules [120].

Another strategy for shape engineering, offered by the versatility of this technique, is the use of a different substrate orientation. An example was anticipated in Sec. 2.3.2 and consists in the use of a (111)-oriented substrate in order to improve the in-plane symmetry of the quantum dots [77]. This approach overcomes the issue of different Ga diffusivity along the [011] and [01-1] crystallographic directions causing shape elongation. In addition to that, even in presence of a dot shape with no planar anisotropy, the atomistic symmetry is related to the orientation of the crystal and passes from C_{2v} to C_{3v}.

To conclude the description of sample fabrication, after the growth of the quantum dots, an upper layer of barrier material is grown on top. A full three-dimensional heterostructure is realized in this way. Moreover, distancing the active region from the semiconductor-air interface is necessary to provide good optical quality. Indeed, it suppresses a channel for non-radiative recombination and minimizes spectral wandering due to fluctuating charges trapped in surface defects [121].

Finally, post-growth annealing at temperatures above 600°C may be used to improve crystal quality, which suffers from the presence of point defects due to the constraints on low substrate temperature during the fundamental crystallization step [122]. In situ annealing at intermediate temperatures before capping is another viable approach [123] able to provide abrupt interfaces and a defect-free atomic structure [124].

Chapter 4

Experimental methods

4.1 Growth and morphological characterization

This thesis deals with semiconductor quantum dots fabricated by a molecular beam epitaxy technique. A major focus of the work is actually devoted to the optimization of the growth procedure. All the samples were produced and characterized by atomic force microscopy at the L-NESS interuniversity research center in Como. I performed data analysis and actively collaborated to the development of the growth recipes. In the next subsections, I briefly outline the experimental setups used for the fabrication of the samples and their morphological characterization.

4.1.1 Molecular beam epitaxy

Molecular beam epitaxy is an experimental method developed for the deposition of thin films of single crystal materials. While, on the one hand, this technique requires ultra-high vacuum and is characterized by a slow deposition rate, on the other hand, it provides unmatched control on the growth of complex heterostructures with abrupt interfaces and high crystal quality. Up to date, this method has been the most investigated—and successful—in the fabrication of epitaxial quantum dots for applications with demanding requirements on quality and structure, such as single-photon emission.

The samples examined and presented in this thesis were fabricated with a Gen II molecular beam epitaxy machine. The apparatus is composed

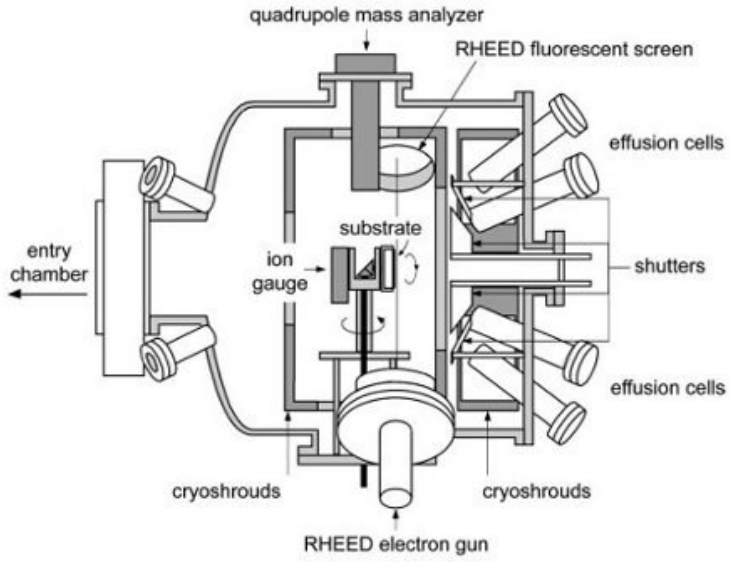

FIGURE 4.1: Schematic illustration of the growth chamber of a III-V molecular beam epitaxy system.

of three connected ultra-high vacuum sections, separated by gate valves. The introduction chamber was vented to atmosphere while inserting the sample—usually a 2" GaAs wafer—which was mounted or soldered with indium onto a molybdenum block. The pressure in this chamber can be brought down to 10^{-9} torr, and some contaminants were removed from the surface of the sample by heating it to 200°C with quartz lamps. The next step took place in the buffer chamber. A degas station allowed to increase the temperature of the substrate up to 600°C in order to desorb impurities and contaminants prior to the transfer into the main chamber.

In the growth chamber, stable ultra-high vacuum is required. Given the typical low deposition rates associated with this technique, the base pressure must be kept as low as possible so to reduce the incorporation of impurities during the growth of the material. We operated at a pressure of 10^{-10} torr, maintained with the help of a combination of three vacuum pumps—cryogenic, ion, and titanium sublimation. In addition to that,

shrouds filled with liquid nitrogen surround components brought at high temperatures. These cold surfaces have a gettering effect that prevents the thermal desorption of gas molecules by hot surfaces from degrading the ultra-high vacuum regime during operation.

A sketch of the growth chamber is reported in Fig. 4.1. A set of effusion cells containing high purity elemental materials—only Ga, As, and Al were used in this work—are disposed radially in front of the sample holder. During operation, specific cells were heated up till the solid material inside starts to sublimate, generating a molecular beam that diffuses balistically—thanks to the long mean free path in ultra-high vacuum—towards the surface of the sample. Al and Ga fluxes were tuned by changing the temperature of the crucible inside a Knudsen cell, whereas a valved cracker cell was used for As. The cracking zone temperature was set so to provide As_4 molecules, and the flux was finely controlled with the needle valve. All the sources are equipped with a pneumatic shutter to rapidly block or release the molecular beam. Accurate control over the molecular fluxes is crucial during deposition, especially in the case of droplet epitaxy of quantum dots. A ionization gauge for the beam flux measurement, mounted on the back of the substrate manipulator, was regularly used to monitor fluxes, together with periodical calibrations based on the thickness of the deposited material.

The other fundamental growth parameter is the temperature of the substrate. An electrical heater on the substrate holder was used to bring the sample to temperatures up to 620°C. The actual temperature was monitored by both a thermocouple and an optical pyrometer in order to achieve a high accuracy, about 5°C.

The main chamber also contains a reflection high-energy electron diffraction setup, which was routinely used to monitor surface structure and morphology during growth.

4.1.2 Atomic force microscopy

The surface morphology of the quantum dots was imaged using a commercial atomic force microscopy setup. The nanometer spatial resolution in three dimensions and non-destructive operation in air make atomic force microscopy an unmatched tool for routine imaging of objects at the nanoscale. Being an instrument for surface analysis, its application is limited to the

collection of structural information of nanostructures at a semiconductor-air interface rather than encapsulated in a multilayered solid structure.

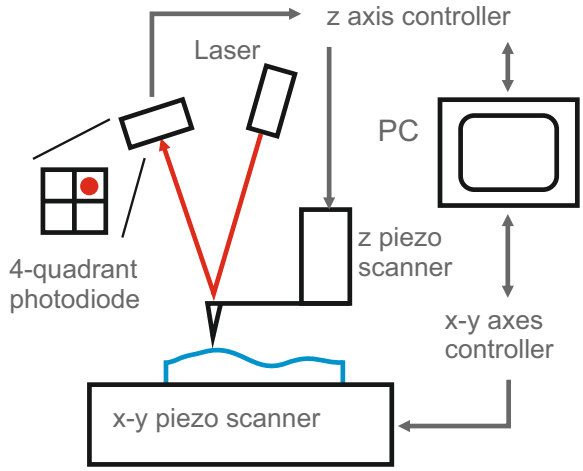

FIGURE 4.2: Schematic illustration of a tapping-mode atomic force microscopy setup.

Figure 4.2 reports a schematic diagram of a typical atomic force microscopy setup like the one used to image the samples studied in this thesis. The principle of operation relies on the interaction between the surface of the sample and an ultra-sharp tip mounted on a cantilever. The motion of the tip caused by atomic forces from the surface induces a tilting in the cantilever which is probed by optical beam deflection. The horizontal displacement of the sample and the vertical position of the cantilever base are controlled by means of piezoelectric actuators which can provide sub-nanometer accuracy.

To perform imaging on large areas rather than force spectroscopy, the instrument was operated in tapping mode [125]. In this mode, the cantilever is driven by a mechanical oscillation at a frequency near its vibrational resonance and the change in the amplitude and phase of the tip oscillation are recorded. Meanwhile the sample is moved in a raster scan pattern, and an electronic feedback loop adjusts the height of the cantilever so that the

tip oscillation amplitude stays fixed—usually in a condition that minimizes contact.

The spatial resolution of this mapping procedure is often limited by the dimensions of the tip, since its shape gets convoluted to the one of the scanned object. In this work rougher probes were used for large area scans (e.g. 10 x 10 μm^2), whereas tips with a radius of 2 nm were used to obtain sound information of the shape of a quantum dot in high resolution images. Data analysis was performed with the modular software Gwyddion which also implements algorithms for artifact remotion and blind tip estimation [126].

4.2 Photoluminescence

The experimental work I performed in this thesis is mainly concentrated on the characterization of semiconductor quantum dots by means of optical spectroscopy. In particular, photoluminescence is the technique of choice, since it provides direct information on the significant physical properties and figures of merit of a quantum dot as a single- or entangled photon emitter. Several different setups, presented in the following subsections, are necessary to address specific ensemble and single dot optical properties.

4.2.1 Ensemble spectroscopy

Macro-photoluminescence at cryogenic temperature is a valuable characterization tool for assessing the process of growth optimization. This technique is mainly used to obtain the distribution of excitonic transitions of an ensemble of emitters, as well as indications on their radiative efficiency. The analysis of the photoluminescence signal as a function of excitation power or sample temperature can give additional information, e.g. on the excited states of the system and on the recombination dynamics of the carriers.

A schematic representation of the setup I employed in this thesis is illustrated in Fig. 4.3. Ensemble photoluminescence measurements were carried out using the 532 nm line of a Nd:YAG continuous wave laser. The actual power incident on the samples for most of the spectra reported here was 0.5 mW, except for the power dependence analysis where it was

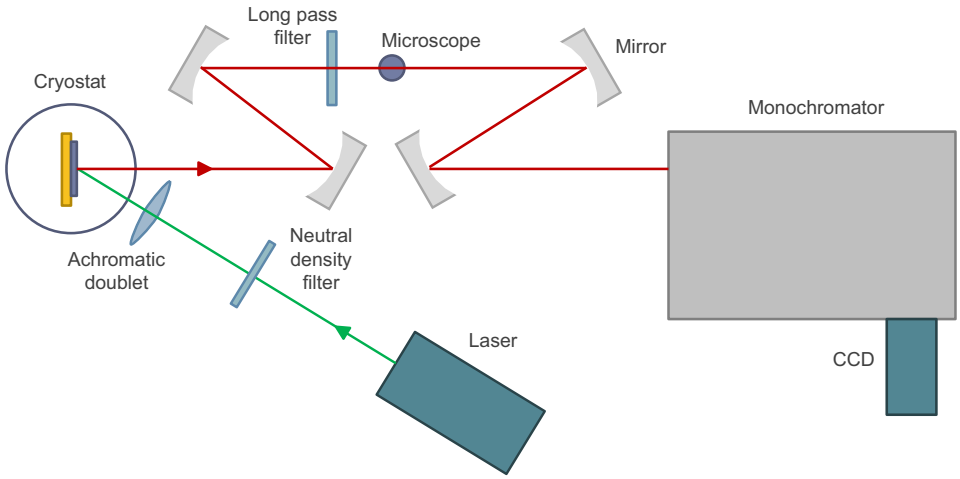

FIGURE 4.3: Schematic illustration of an ensemble photoluminescence setup.

changed in steps from 5 mW to 5 μW adding neutral density filters to the excitation path.

The laser beam was focused on the sample through an achromatic doublet with 50 mm focal length and arrived with an angle of incidence of 45°. The laser spot size on the sample surface was approximately 80 μm, resulting in the simultaneous excitation of thousands of quantum dots on our low density samples. The photoluminescence was collected at normal incidence by a series of spherical mirrors and separated from the laser stray light with a long pass filter. A flipping mirror was placed between the second and the third spherical mirrors, so that it could route the light collected from the sample to an optical microscope to directly view its surface. When the mirror was removed from the collection path, the photoluminescence signal entered a spectrometer with 500 mm focal length, was dispersed by a 150 l/mm diffraction grating, and then was analyzed by a Peltier-cooled CCD detector. The resulting spectral pitch was 0.8 meV. The large spectral window allows to simultaneously collect and analyze the signal from the substrate, the barrier material, and the quantum dots.

The samples were mounted inside a closed-cycle cryostat and cooled

down to a 15 K. In few measurements the temperature was increased in a guided way with a heating wire attached to a PID control loop.

4.2.2 Single dot spectroscopy

Inhomogeneous broadening coming from the size dispersion of the quantum dots hinders the access to fundamental optical and electronic properties in ensemble measurements. In order to identify different excitonic complexes and study their fine structure, a higher spatial resolution of the order of 1 μm is needed, so that the signal from an individual emitter can be singled out.

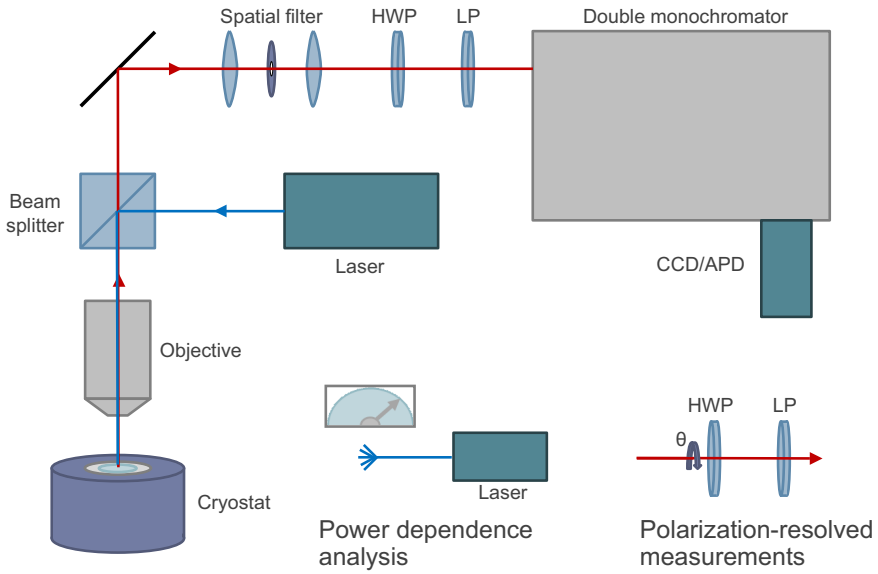

FIGURE 4.4: Schematic illustration of a micro-photoluminescence setup. Two insets at the bottom left depict the power dependence and polarization-resolved modes of operation.

A typical micro-photoluminescence apparatus is shown in Fig. 4.4. In this thesis I used two similar setups: one assembled at the University of

Milano-Bicocca and pictured in Fig. 4.5; the other in the equipment of the JKU Linz, together with the setups listed in the following subsections.

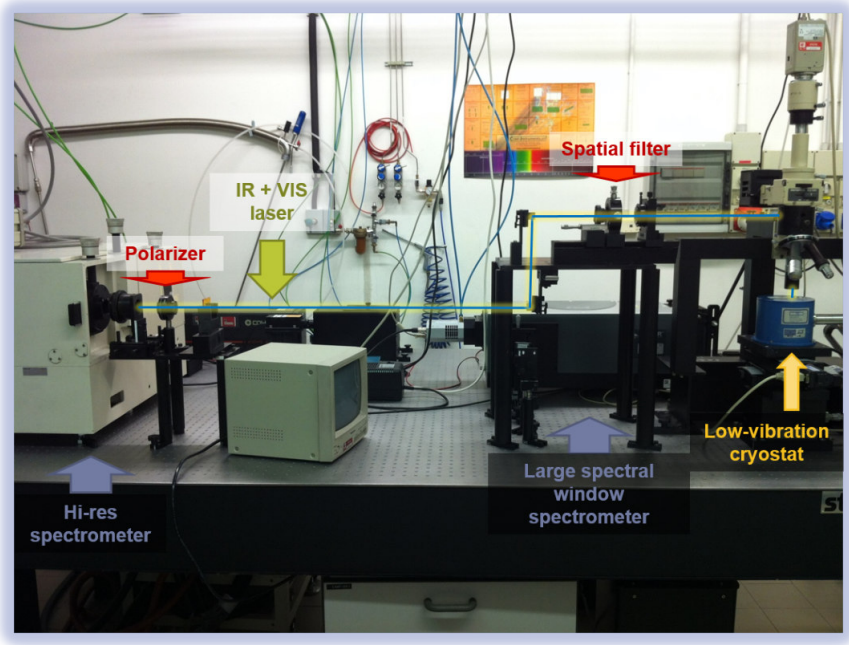

FIGURE 4.5: Picture of the micro-photoluminescence setup I assembled at the University of Milano-Bicocca. Main components are labeled and highlighted by arrows. The half-wave plate in the collection path is missing. Laser shielding panels are added during operation.

Different laser sources were used to perform single dot photoluminescence measurements. In non-resonant and continuous wave excitation conditions, either a Argon ion laser emitting at 457.9 nm or the 532 nm line of a Nd:YVO_4 laser was used. The power was varied over a wide range of values, from 1-20 nW to 1-10 μW, in order to study radiative recombination at different filling levels. During time-resolved experiments, the quantum dots were excited with a pulsed diode laser emitting at 440 nm with 80 MHz repetition rate and a pulse width below 100 ps. Finally, resonant two-photon excitation was accomplished using a Ti:sapphire femtosecond

laser, with 80 MHz repetition rate and a pulse width around 100 fs, tunable in the wavelength range from 690 to 1040 nm. In order to reduce the spectral width of the pulse, its duration was broadened from 100 fs to about 10 ps by means of a 4f pulse-shaper.

The sample was excited at normal incidence through a 0.42 NA objective—optimized for operation in the NIR window and long working distance—resulting in a 1.4 μm spot diameter, according to the Rayleigh criterion [127]. Under above barrier excitation the photo-excited carriers can diffuse and broaden the spatial extension of the region of emission to a disk of about 3 μm of diameter. The emission of the sample was collected in collinear geometry, and a spatial filter, implemented with either a couple of lenses and a pinhole or a single mode optical fiber, was added to the collection path when needed to isolate emitters near the center of the ensemble emission energy distribution. In some measurements, a solid immersion lens—a hemisphere with 2 mm diameter made out of zirconium—was fixed on top of the sample with vacuum grease. This procedure allowed to achieve an 8-fold enhancement in light extraction from the semiconductor heterostructures. Since the solid immersion lens is affected by a heavy chromatic aberration, the objective was focused at the wavelength of emission of the quantum dots, resulting in a larger laser spot in the case of non-resonant excitation. Under these conditions, spatial filtering in the collection path is usually required.

Accurate positioning was achieved with a couple of motorized mechanical linear stages placed below the cryostat for the horizontal axes and with either a manual or piezoelectric vertical scanner for the objective. I developed a code in the LabVIEW programming environment to interface the horizontal stages with the acquisition software and perform spatial mapping of the photoluminescence signal.

In order to suppress laser backscattering a long pass filter was used under above-barrier excitation, whereas in the case of resonant excitation three tunable notch filters with a bandwidth of 0.4 nm were placed in the collection path.

The filtered quantum dot emission was sent either in a 800 mm focal length double spectrometer with two additive 900 l/mm gratings operating at second diffraction order or in a 750 mm focal length double spectrometer with two additive 1200 l/mm gratings operating at first diffraction order.

A 40 μeV spectral resolution was achieved in the 700–800 nm wavelength region.

During continuous wave operation, the signal was acquired by a CCD camera with either Peltier deep-cooling or deep depletion, back illumination, and liquid-nitrogen cooling. Instead, for time-resolved experiments, a single-photon avalanche detector with time resolution slightly above 50 ps was used, controlled by a time-correlated single-photon counting module.

The samples were mounted inside a low-vibration continuous-flow helium cryostat working at a 8 K temperature. The requirement for spatial resolution below 1μm poses stringent demands on vibration damping and stability against drift movements on the time scale of hours. The closed-cycle cryostat used for macro-photoluminescence measurements was not able to meet these standards.

Polarization-dependent spectra were acquired by adding a fixed linear polarizer and a rotating half-wave plate to the collection path. For each measurement several polarized spectra were recorded at different orientations of the half-wave plate. Also in this case I developed a LabVIEW code for synchronizing the motorized rotation of the half-wave plate with the acquisition of the signal. The emission lines were fitted with a Gaussian line shape in order to extract their peak position. The energy shift was then fitted with a sinusoidal function, thus estimating the fine structure splitting with very high accuracy down to 1 μeV [70]. The excitation power was kept at 0.2–2 μW, near the saturation level of the neutral exciton line. I chose to operate in this condition to achieve fast acquisition of the lines from the main excitonic complexes (see Sec. 3.2) while keeping low the contributions related to other more complex multiexcitonic features.

4.2.3 Michelson interferometry

The double spectrometer presented in the last section allows to achieve a high resolution of 40 μeV. However, the natural linewidth of typical GaAs quantum dots is in the range of few μeV. If spectral wandering effects are weak, a dispersive technique does not provide the required sensitivity, so I resorted to an interferometric apparatus.

A Michelson interferometer, like the one depicted in Fig. 4.6, was placed in front of the entrance slit of the spectrometer. The design of the setup and

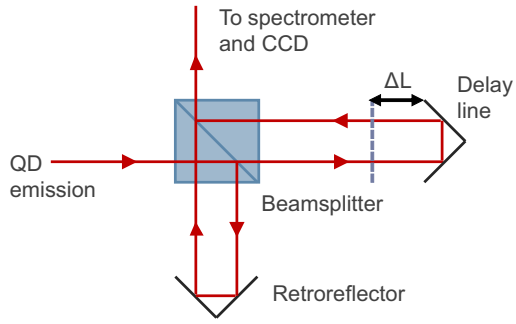

FIGURE 4.6: Schematic illustration of a Michelson interferometer. This delay line was inserted in the collection path of the micro-photoluminescence setup shown in Fig. 4.4 to perform coherence time measurements.

the data analysis followed the methodology presented in Ref. [128]. The delay between the two paths was changed using motorized linear stages that control the position of the retroreflectors. One was moved by a long range mechanical stage (30 cm, equivalent to a maximum delay of 2 ns), which allowed to set large delays comparable to the decoherence length of the emitted radiation. The other one was controlled by a high precision piezoelectric drive and was used to record interference fringes using step sizes below the wavelength of radiation.

The complete interference pattern as a function of delay time $I(t)$ is described by a sinusoidal function modulated by a monotonically decaying curve $C(t)$.

$$I(t) = I_0(1 + C(t)cos(\omega_0 t + \phi(t))) \tag{4.1}$$

ω_0 is the central detection frequency and $\phi(t)$ accounts for a slowly varying phase factor in case of asymmetry in the line profile.

In an actual measurement, the piezoelectric stage was scanned across a distance of a few wavelengths while photoluminescence spectra were acquired with a CCD camera. This operation was repeated for a series of given time delays, controlled with the mechanical stage. For each scan of the piezoelectric stage, the integrated intensity of the emission line of interest was plotted and the amplitude of the interference fringes was quantified in

terms of visibility V [129].

$$V = (I_{max} - I_{min})/(I_{max} + I_{min}) \tag{4.2}$$

I_{max} and I_{min} are the maximum and minimum signal intensities in a relatively short time interval where the interference pattern can be fitted by a simple sinusoidal function.

The visibility as a function of time delay is actually a direct measurement of the first-order correlation function of the electric field $E(t)$ [105, 130].

$$V(\tau) = \left| g^{(1)}(\tau) \right| = \left| \frac{\langle E^*(t)E(t+\tau)\rangle}{\langle E^*(t)E(t)\rangle} \right| \tag{4.3}$$

The decay of the first-order correlation function is dictated by the loss of coherence of the probed radiation field. Its functional form depends on the specific decoherence mechanisms involved and is related by Fourier transform to the spectral line shape, thus giving information on the exciton linewidth for quantum dots.

Using this technique pure dephasing effects—that determine the total decoherence time in addition to the natural lifetime [42]—are investigated on average on the typical temporal scale of acquisition ($\sim$ seconds).

4.2.4 Hanbury Brown–Twiss setup

I introduced in Sec. 2.3 the second-order correlation function $g^{(2)}(\tau)$, a useful concept in order to describe the photon statistics of a single-photon source. This quantity can be experimentally determined in a coincidence counting experiment using a Hanbury Brown–Twiss setup like the one sketched in Fig. 4.2.4a. In principle, a continuous time-resolved detection of light intensity would be sufficient to evaluate the expression in Eq. 2.7. However, in practice, every detector has a dead time, so that it cannot register two events within a close delay. The idea behind this approach consists in using two detectors and correlate their detection events with high speed electronics in order to overcome this problem.

In a typical experiment, the light emission collected from a selected quantum dot was sent to a non-polarizing beamsplitter and then to two polarization maintaining single mode fibers. The photoluminescence signal

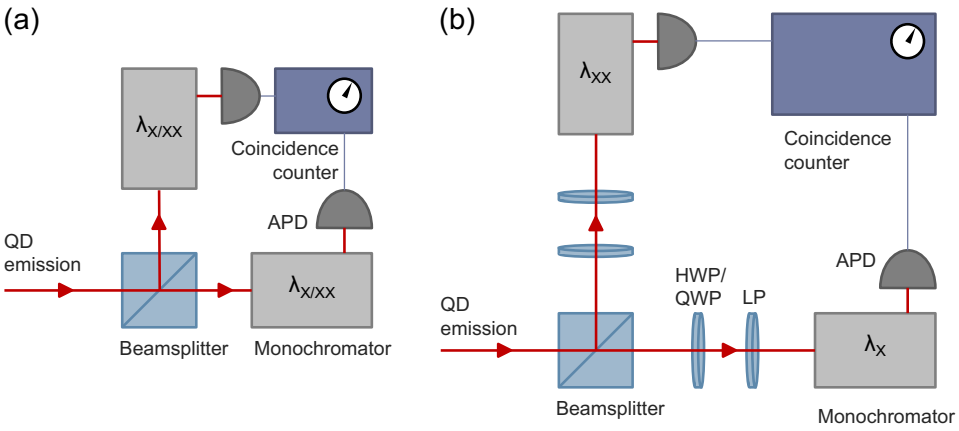

FIGURE 4.7: Schematic illustration of a Hanbury Brown–Twiss interferometer. This apparatus modifies the last part of the collection path in the micro-photoluminescence setup shown in Fig. 4.4 for coincidence correlation analysis. Slightly different arrangements are used to perform: a) autocorrelation measurements to evaluate the second-order correlation function $g^{(2)}(\tau)$; b) cross-correlation measurements in different polarization bases to estimate entanglement fidelity.

at the output of these fibers was sent to two independent spectrometers which could be tuned to direct a specific wavelength to an avalanche photodiode. In autocorrelation measurements the wavelength is the same on the two paths and it corresponds to the center of the selected emission line. In contrast to the lifetime measurements presented in Sec. 4.2.2 where a high temporal resolution is crucial, high detection efficiency is the most relevant figure of merit here, so to maximize the number of useful coincidence events. This results in a longer timing jitter, 500 ps for the avalanche detectors used here, a value still significantly lower with respect to the temporal distance between two recombination events triggered by consecutive laser pulses, 12.5 ns with a 80 MHz repetition rate.

The detectors were connected to a fast correlation electronics system

with two channels operating in time-tagging mode, that is registering individual photon events with their arrival time and processing this information via an algorithm to generate a histogram of coincidence events $n(\tau)$. If the signal-to-noise ratio is high enough, this quantity is equal to the second-order coherence function $g^{(2)}(\tau)$.

A Hanbury Brown–Twiss setup can be also used for measuring the degree of entanglement of a pair of photons. Figure 4.2.4b shows the apparatus I used for estimating the fidelity of photons emitted from the biexciton-exciton cascade in quantum dots to the expected maximally entangled Bell state. The two spectrometers were set to transmit the wavelength of the biexciton and exciton line respectively, while either a quarter-wave or a half-wave plate and a linear polarizer were inserted right after the beamsplitter on both paths to count coincidences in different polarization bases. In particular, three photon qubit bases were considered. The first one was studied with the insertion of quarter-wave plates and is composed of the right- and left-handed circular polarization states. The other two are formed by pairs of orthogonal linear polarization states, rotated one with respect to the other by 45°, and were selected with the help of half-wave plates.

Coincidence measurements allow to estimate the degree of correlation C_{AB} between two generic polarization bases $A = (a, \bar{a})$ and $B = (b, \bar{b})$, a physical quantity which enters Bell inequalities [131] and quantum state tomography [62]. In fact, this figure of merit was directly obtained from experimental estimates of the second-order cross-correlation function $g^{(2)}_{X,XX}(0)$ in co- and cross-polarized configurations.

$$C_{AB} = p(a,b) - p(a,\bar{b}) = \frac{g^{(2)}_{Xa,XXb} - g^{(2)}_{Xa,XX\bar{b}}}{g^{(2)}_{Xa,XXb} + g^{(2)}_{Xa,XX\bar{b}}} \tag{4.4}$$

$p(a,b)$ is the normalized probability of detection of a photon with polarization state a and a second one with polarization b within a given time interval, $g^{(2)}_{Xa,XXb}$ and $g^{(2)}_{Xa,XX\bar{b}}$ were evaluated in an equivalent time bin around zero delay.

4.2.5 Hong-Ou-Mandel experiment

In Sec. 4.2.3 I introduced the necessity of estimating the magnitude of spectral wandering effects. The presence of dephasing mechanisms affecting the coherence of the exciton state is particularly relevant for the characterization of single-photon emitters. Indeed, quantum communication protocols and quantum computation with linear optics [9, 13] primarily rely on interference effects between single-photon qubits and perfect frequency matching is paramount to get high efficiency for the single operation and then scale up the complexity of the system.

In this context, a more direct figure of merit of the performance of a quantum dot light source is the degree of indistinguishability of the photons emitted. When indistinguishable photons are considered, quantum interference effects, whose outcome is dictated by the superposition of probability amplitudes, can be observed. The most simple and common way to recreate two-photon quantum interference is the Hong-Ou-Mandel effect [132], that consists in the interference of two indistinguishable photons impinging at the same time on two entries of a symmetric 50:50 beam splitter. As a result of the bosonic statistics of photon creation and destruction operators at the beamsplitter interface [133] in the case of perfect indistinguishability—in time of arrival, frequency, polarization, wave packet profile—the two photons are expected to leave in the same direction.

This phenomenon can be actually observed, and the degree of indistinguishability estimated, in a coincidence counting experiment. Figure 4.8 illustrates the setup I employed for test measurements of Hong-Ou-Mandel interference, based on a design similar to the one used in Ref. [134, 135].

A pulsed laser (80 MHz repetition rate, 12.5 ns temporal separation) was used to optically pump the quantum dot. In the excitation path, a Mach-Zehnder delay line was inserted so to obtain a train of pairs of pulses separated by a 2 ns delay ΔT. An analogous Mach-Zehnder interferometer was inserted in the collection path as well, with the addition of a couple of linear polarizers used to select photons with the same polarization state. Upon the arrival of two subsequent laser pulses, the quantum dot can emit two photons that may interfere at the last beamsplitter, depending on the path taken. The coincidences at opposite output ports of the beam splitter were monitored as described in Sec. 4.2.4.

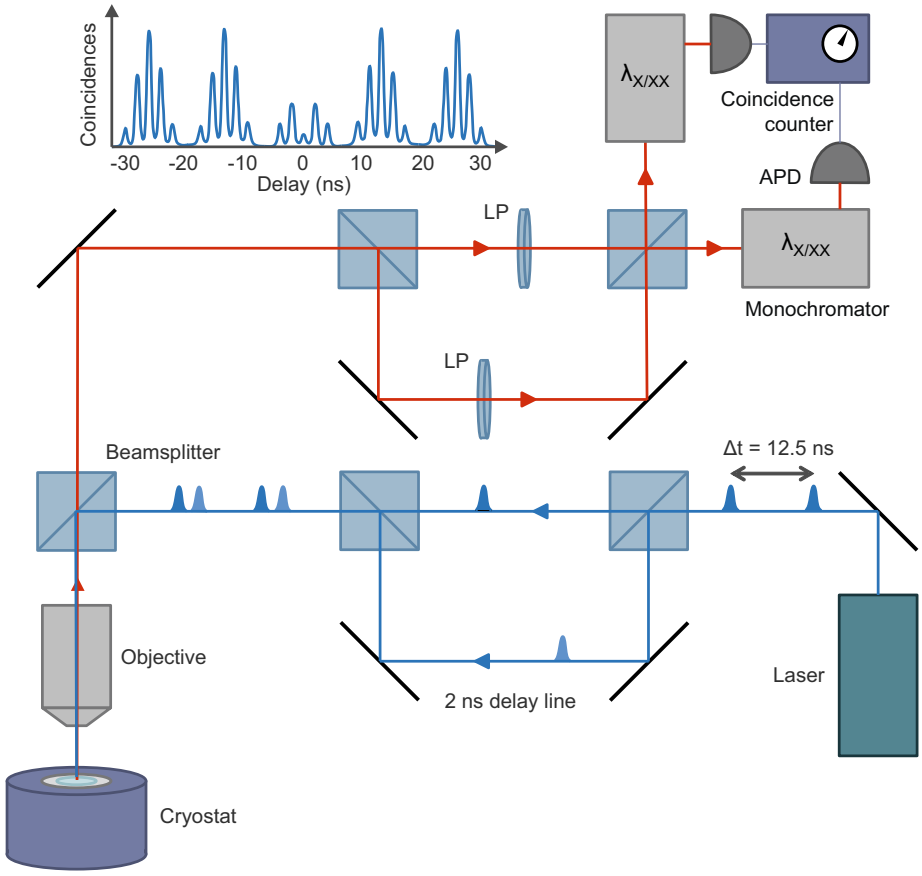

FIGURE 4.8: Schematic illustration of a Hong-Ou-Mandel interferometer. The insert (left top corner) reports a typical histogram of the delay time between consecutive detection events at the opposite counters.

The inset of Fig. 4.8 shows a typical histogram of coincidence events and features five peaks at different delay times related to the possible combinations of photon paths. The central peak at zero time delay corresponds to the situation where the first photon emitted by the quantum dot takes the long arm of the Mach-Zehnder, while the second photon takes the short one.

In this case, both photons arrive at the beamsplitter simultaneously. If they are distinguishable and no interference takes place, this peak is expected to have the same intensity of the side ones ($\pm\Delta T$). Instead, if the conditions for quantum interference are satisfied, a dip in intensity is observed, related to the fact that the photons leave the beamsplitter together at a specific port.

In real experiments, the intensity of the central peak is not completely suppressed due to the incoherent phonon sidebands, the time jitter in the emission, and the dephasing from charge noise, spin noise, and lattice vibrations. The overlap between the photon wave functions at the 50:50 beamsplitter directly corresponds to the visibility V_{HOM} of two-photon interference, defined as the ratio between the measured integrated intensity of the coincidences peak at zero time delay and its expected value in the case of totally distinguishable photons. I estimated this quantity by dividing the area of the central peak $A(0)$ in the histogram of the coincidence counts by the average of the areas of the two side ones $A(\pm\Delta T)$, which give a reference of the expected number of events with two photons leaving the beamsplitter from opposite ports if no quantum interference takes place.

$$V_{HOM} = 1 - \frac{2A(0)}{A(-\Delta T) + (\Delta T)} \tag{4.5}$$

Chapter 5

GaAs quantum dots grown by droplet epitaxy for entangled photon generation

5.1 Growth optimization and optical properties

One of the distinguishing features of droplet epitaxy is the possibility to design the shape of the nanostructures through careful adjustment of the growth parameters that are employed during the crystallization of the droplets. In this section, I will present a detailed investigation of the impact of substrate temperature and As flux on the geometry and the optical properties of the quantum dots. In particular, I will describe the process by which a sample is designed, and how morphological characterization and optical spectroscopy offer a feedback that guides the choice of deposition parameters. Ultimately, this allows to hit the goals on emission wavelength and optical quality.

5.1.1 Simulation and design

One of the main specifications of an optoelectronic device is the wavelength of operation, which is strictly dictated by the envisaged application. As I previously discussed in Sec. 2.1 and 2.3.3, if an entangled photon source is

meant to be used as a building block of a quantum network, it must match a spectral region where single-photon detectors with high efficiency exist and should be interfaced with a storage element for the photon polarization qubit. This task can be performed by a Rb atomic cell, that operates in the large dispersion region between its D_2 absorption lines—around 780 nm. Luckily enough, we know from Sec. 3.1.1 that the confinement energy in nanostructures offers an additional knob for tuning the wavelength of emission, namely size.

Since typical band parameters for AlGaAs and GaAs are well-known, it is possible to computationally estimate the expected energy of emission once the geometry of the quantum dot is known. A rough prediction of the confinement energy can play a useful role already during the first phase of development of the deposition procedure for the quantum dots. First, it can help to define an approximate target for the dimensions of the nanostructure, which can be easily probed by means of atomic force microscopy on uncapped samples. In addition to that, a comparison between the emission energy as estimated with such a calculation and the ensemble photoluminescence emission from a complete sample can reveal significant changes in size after capping or thermal treatment. While this analysis is hardly quantitative, it provides information on a large ensemble of emitters, is non-destructive and can be performed much more quickly as compared to a statistically significant series of direct imaging measurements by means of cross-sectional TEM or STM. Hence, it is a valuable tool to guide the optimization of a growth protocol and to give an indication of presence of intermixing between the dot and the barrier materials.

In order to compare the geometry probed by atomic force microscopy scans with the results of ensemble photoluminescence measurements performed on our samples, I developed a numerical code based on the simple effective-mass, constant-potential and single-band model presented in Sec. 3.1.1. The numerical procedure adopted to solve the problem follows closely the approach described in Ref. [136]. The states of an electron or a hole in the quantum dot are described by the Schrödinger equation for the envelop function, which is derived from the effective-mass approximation in the case of a finite potential well with arbitrary shape. The solution to the equation is expressed as a linear combination of eigenfunctions of an infinite square well potential, a.k.a. particle in a box, problem. When this

generic solution is substituted into the Schrödinger equation and projected onto the orthonormal basis of wave functions of the cuboidal problem with infinite barrier height, the resulting matrix equation returns as eigenvalues the confinement energies of the bound states of the carriers. The hypothesis of pyramidal shape, used in the cited paper in order to minimize computational cost, is relaxed here. The three-dimensional shape of the potential well can be described by a generic surface map, e.g. taken from a scan performed by atomic force microscopy. This high flexibility on the morphology of the quantum dot, which is called for by the broad shape engineering capabilities of the droplet epitaxy technique, together with the modest computational requirements, are the two main advantages of this method.

The script was written in the MATLAB programming language, so to easily have access to optimized routines for the diagonalization of large matrices and for the graphical representation of the spatial distribution of energy eigenstates. The calculation of the matrix elements is performed by a function written in the C programming language using parallel processing in order to speed up the computation of volume integrals.

The correct implementation of the software was successfully tested against simple problems with analytic solution, such as the parallelepiped potential well, and by comparison with the predictions on pyramidal InAs/GaAs dots presented in Ref. [136] (see Fig. 5.1). The energy eigenvalues converge within 1 meV using a basis of at least 19 orthonormal wave functions per linear dimension. This amounts to a modest memory consumption of 0.75 GB—memory usage being the main performance bottleneck. A more complex shape may require a higher number of wave functions, but it can still be easily be managed by a small computer cluster or even by an affordable desktop workstation. As a demanding test case, the application to realistic geometries of asymmetric quantum molecules grown by droplet epitaxy is briefly discussed in Appx. A.

The assumptions of this model are quite basic. Band mixing is not taken into account, $k \cdot p$ perturbation theory would have to be included. The effect of mixing between heavy and light holes could be non-negligible, especially for the excited states. In addition to that, also the Coulomb interaction between electron and hole—a perturbative term in GaAs due to the quite shorter Bohr radius as compared to the De Broglie wavelength

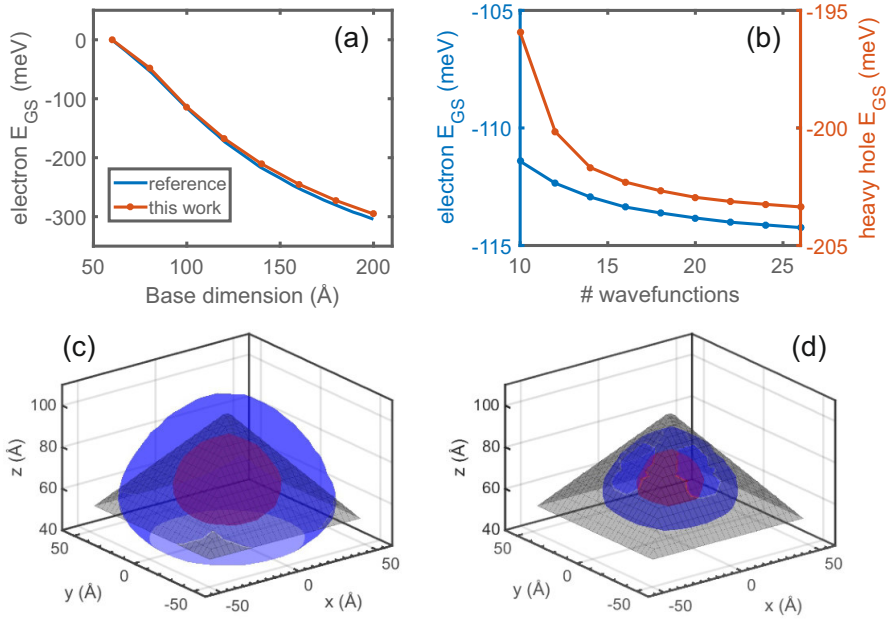

FIGURE 5.1: a) Energy of the electron ground state with respect to the GaAs conduction band as a function of size for InAs pyramidal quantum dots. Comparison between the predictions reported in Ref. [136] and calculated with the script employed here. b) Energy of the electron and heavy-hole ground state vs. the number of basis wave functions per linear dimension used in the simulation. c) Probability density isosurfaces (50% red, 95% blue) of the envelope function of the wave function of an electron confined inside a square pyramid InAs/GaAs well, ground state. d) Same as (c) for the ground state heavy hole.

[97]—is totally disregarded. Despite all these assumptions, it has been reported in the literature that the model succeeds in predicting the number of bound states and in giving approximate estimates of their energy [136, 137], proving itself valuable in routine interpretation of experimental data. This approach applies effectively to the lattice-matched GaAs/AlGaAs materials system. Indeed, in addition to the ordered alloy phase of the dot

material, a great simplification comes from the absence of strain. Complex local effects on the electronic structure and the presence of a piezoelectric potential due to strain can be neglected, thus facilitating the choice of band parameters.

5.1.2 Quantum dot morphology and ensemble photoluminescence

As we enter the discussion of the optimization of the growth protocol towards the goal of reliably fabricating entangled photon emitters for hybrid atomic-solid state quantum technologies, the concepts introduced in the previous subsection provide a useful guide. Among the multiple challenges that will be discussed in this section, I focus here on the tuning of the emission wavelength. In particular, I present a systematic study of the influence of the main deposition parameters during the crystallization phase over the morphology of the quantum dots, as probed by means of atomic force microscopy, and discuss how it relates to the results of ensemble photoluminescence experiments.

As previously described in Sec. 2.3.2, transposing the growth protocol of GaAs/AlGaAs droplet epitaxy on a substrate with (111)A orientation was a key improvement that paved the way for the demonstration of polarization-entangled photon generation with a strong degree of entanglement without the use of external fields or temporal post-selection. While the intricacies of the formation and crystallization of nanodroplets on (100) surfaces are now well understood, leading to strong control over shape and aspect ratio (see Sec. 3.4), the investigation of this process on (111)A substrates is still in its infancy [138].

Taking as a starting point the recent literature on the topic [27], we considered crystallization of the GaAs quantum dots at a temperature of 200°C. Such a low substrate temperature is a typical feature of standard droplet epitaxy. The dots were embedded between two barrier layers made of AlGaAs with 30% Al content, deposited at the much higher temperature of 520°C, each with a thickness of 50 nm. In particular, we used a set of parameters for temperature and III-V fluxes specifically developed to minimize the formation of hillocks and provide a flat surface before the

deposition of quantum dots [139]. A very thin capping layer made of GaAs—5 nm—was finally added to prevent surface oxidation.

The deposition of the Ga droplets was performed by providing 0.1 ML on a surface kept at 450°C, resulting in a surface density of $3 \cdot 10^8$ cm^{-2}. Here I present the results for a sample where an As flux of $2 \cdot 10^{-6}$ torr was employed during the crystallization phase. Atomic force microscopy images on an uncapped replica of this sample unveil a rather symmetric truncated pyramid shape with average values of base radius and height respectively of 17 and 10 nm (see Fig. 5.2a).

The dimensions of an average quantum dot are well below the de Broglie wavelength in GaAs so that tridimensional confinement is expected. At the same time, the vertical extension of few tens of monolayers achieves a relatively low confinement energy, complying with the target emission energy being approximately 70 meV above the bandgap of GaAs. I obtained a more quantitative evaluation of the expected emission energy by employing the effective-mass constant-potential model introduced in the previous subsection.

The potential well was modeled as a truncated pyramid, mimicking the experimentally determined geometry, with base radius and height equal to the average values of the measured size distribution. The main concern is about the position of the centroid of the emission band in ensemble photoluminescence, so there is no need to launch multiple simulations covering a range of different sizes observed on the sample. The band parameters used in the calculation for GaAs and AlGaAs are taken from Ref. [90, 137] and reported in Table 5.1. I run a simulation using a basis of 25 wave functions per linear dimension and obtained an energy of the ground state transition of 1.568 meV, corresponding to 790 nm in vacuum. Keeping into account typical ensemble linewidth values, around 15–25 nm, a fraction of the quantum dots is expected to emit near the target wavelength of 780 nm.

However, the ensemble photoluminescence spectrum of the sample with upper barrier and capping layers shown in Fig. 5.2b points out a dramatic discrepancy with respect to what expected. The excitation laser power used for the measurement was set low enough not to have an impact on the spectral shape. Under this condition, and at cryogenic temperatures, the contribution from the recombination of excited states is negligible and the

TABLE 5.1: Parameters used in the effective-mass model to describe conduction and valence (heavy- and light-hole) bands in the GaAs/AlGaAs materials system: effective mass of conduction band electrons (m_e), effective mass of heavy holes (m_{hh}), effective mass of light holes (m_{lh}), conduction band offset (ΔE_c), valence band offset (ΔE_v)

Material	m_e	m_{hh}	m_{lh}	ΔE_c (meV)	ΔE_v (meV)
GaAs	0.067	0.51	0.082		
AlGaAs (30% Al)	0.093	0.57	0.1054	262	195

distribution of emission energy reveals the actual population of excitonic ground states. This happens to be heavily blueshifted as compared to the value calculated on the geometry probed by atomic force microscopy on the uncapped sample, from about 1.57 to 1.86 eV. The behavior was consistently reproduced over repeated growth attempts.

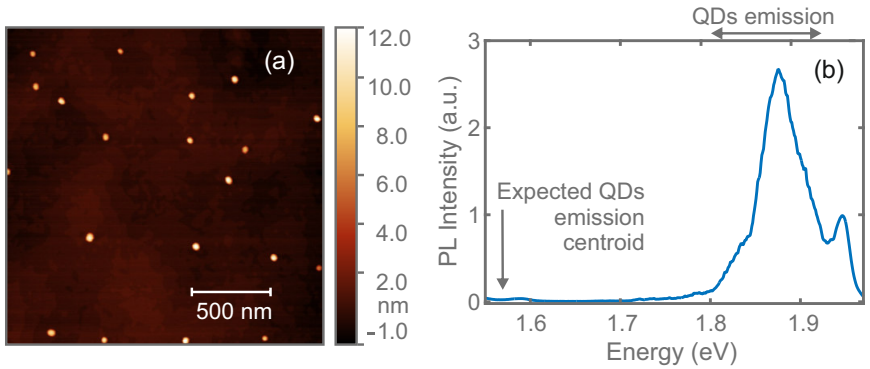

FIGURE 5.2: a) An example of atomic force microscopy image from an uncapped sample with quantum dots crystallized at 200°C. b) Low temperature ensemble photoluminescence spectrum from a sample with an equal quantum dots preparation and the addition of the upper barrier and capping layers.

An increase in the energy of transition must come from higher confinement energy. The tighter carrier localization is very likely caused by heavy

intermixing at the interface of the nanocrystal. I suggest that the low temperature of crystallization enables the formation of point defects, such as the As vacancies [122, 140] reported for droplet epitaxy on (100) substrates, which then promote interdiffusion during the immediately following step, when the temperature is raised to 520°C and the nanostructure is slowly covered with an AlGaAs layer.

Failure to control the size of the quantum dots is a serious issue because it undermines the reproducibility of the growth protocol and limits the capabilities of wavelength tuning. Approaching lower wavelengths close to 780 nm appears out of reach.

The low substrate temperature used during the crystallization of the droplets likely causes strong interdiffusion during their capping at higher temperature and spectral wandering, negatively affecting the optical quality of the sample, as discussed later in subsection 5.1.4. However, it is a distinctive feature of the droplet epitaxial growth technique (see Sec. 3.4).

On the other hand, recent studies on self-assisted Ga nanowires [141], prepared on a GaAs(111)A substrate, highlighted the possibility to retain a rounded top even at the elevated temperature of 580°C. The possibility to extend the three-dimensional growth mode to higher temperatures by working with this substrate orientation was also brought forward in Ref. [138], even if only formation of large islands is presented there.

Following these clues, we explored the fabrication of quantum dots in conditions of increased substrate temperature during crystallization. Formation of three-dimensional nanocrystals was observed up to 520°C, the same temperature which is used for deposition of GaAs and AlGaAs with high crystalline quality on (111)A substrates.

It is possible to give an explanation based on the kinetic model presented in Sec. 3.4 that considers two competing channels of As incorporation. With respect to the case of (100) surface orientation, (111)A presents a peculiar and crucial difference, that is an extremely lower As sticking coefficient [142]. The short As surface lifetime reduces the reactivity of the surface surrounding the droplet towards incorporation of Ga adatoms. The decreased probability of this mechanism allows the other one, that is As direct incorporation in the droplet followed by supersaturation and precipitation at the droplet/substrate interface, to be favorable even at high temperatures.

In a similar fashion to the in-depth analysis presented in Ref. [29], we fabricated several samples differing in substrate temperature T_{sub} and As beam equivalent pressure P_{As} during the quantum dot crystallization process. The spatial density of the droplets is kept constant near 2.5 μm^{-2}. By changing one parameter at once, two series of uncapped samples were prepared with the aim to understand the impact of growth parameters on the geometry of the quantum dots. Recipes and average dimensions are reported in Table 5.2.

TABLE 5.2: Average and standard deviation of the radius (r) and height (h) distributions are listed together with the full emission wavelength (λ_{em}) range for a series of samples differing in the amount of Ga supplied for the droplets and in the substrate temperature (T_{sub}) and As beam equivalent pressure (P_{As}) during the quantum dot crystallization process.

x_{Al}(%)	$T_{sub}(^\circ)$	Ga (MLs)	P_{As}(torr)	r(nm)	h(nm)	λ_{em}(nm)
30	200	0.1	$2 \cdot 10^{-6}$	17 ± 2	10 ± 2	640–690
30	400	0.1	$2 \cdot 10^{-6}$	31 ± 7	2.6 ± 0.7	660–715
30	500	0.4	$1.2 \cdot 10^{-6}$	34 ± 6	2.2 ± 0.6	660–705
30	500	0.2	$2 \cdot 10^{-6}$	24 ± 5	1.6 ± 0.3	650–690
30	500	0.4	$3 \cdot 10^{-5}$	43 ± 8	4.1 ± 1.0	690–765
30	520	0.4	$7 \cdot 10^{-5}$	34 ± 7	3.8 ± 0.7	665–770
15	500	0.4	$3 \cdot 10^{-5}$	-	-	730–780

As expected, we discovered that the choice of crystallization process strongly affects the morphology of the quantum dots. In particular, either increasing the As flux or decreasing the substrate temperature results in nanostructures with a higher aspect ratio. Differences in volume can be easily interpreted as a function of the amount of Ga provided for the formation of the metallic droplets. A direct consequence is that the exposure of the droplets to an As flux at a temperature close to the one of the deposition of AlGaAs layers with high material quality leads to flatter nanocrystals. This implicates stronger confinement and again hinders emission at lower wavelengths near the 780 nm target. On the other hand, a taller structure can be handily recovered by providing a larger As flux during crystallization.

The dependence of the base shape of the quantum dots on the growth parameters is less trivial. Images of typical quantum dots for different samples are reported in Fig. 5.3. In most of the cases, I observed a hexagonal or triangular base, compatible with the required C_{3v} symmetry. A higher resolution image will be discussed later on in Sec. 5.2. Instead, on a sample grown at high temperature and moderate As flux, some structures with a more complex double branched geometry were spotted.

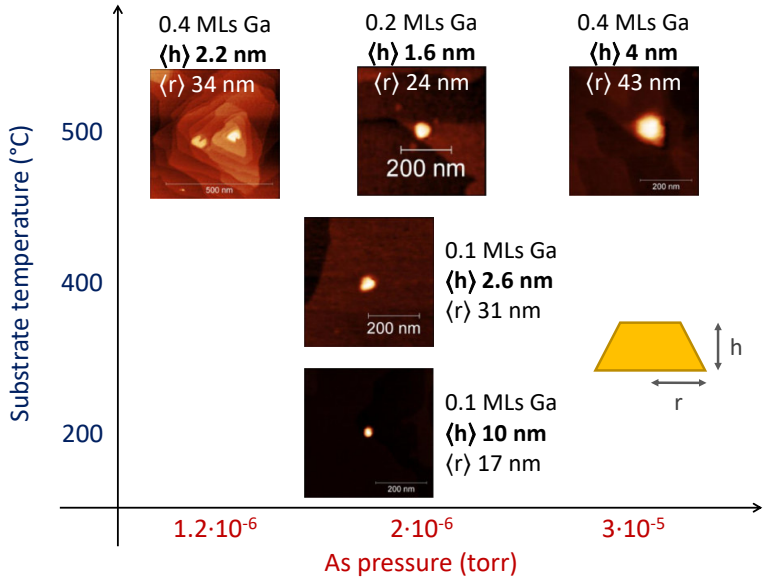

FIGURE 5.3: Atomic force microscopy scans of single quantum dots crystallized in different conditions of substrate temperature and As flux (rows 1–5 of Table 5.2).

Once again I investigated the link between the various achieved geometries and their related optical properties, by means of ensemble photoluminescence. In addition to average uncapped quantum dots dimensions, Table 5.2 also reports the range of emission wavelength. As demanded, the control over the height of the quantum dots translates into a tuning of their emission energy. Some of the corresponding ensemble photoluminescence spectra are displayed in Fig. 5.4.

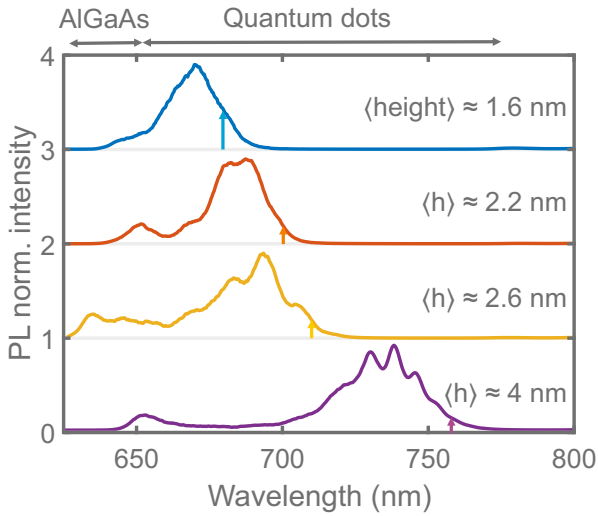

FIGURE 5.4: Low temperature ensemble photoluminescence spectra of a series of samples with 30% Al content in the barrier layers and crystallization temperature above 400°C (rows 2–5 of Table 5.2) with varying confinement strength along the growth direction. Vertical arrows mark the expected ground state exciton energies assuming the height values—average experimental data on uncapped quantum dots—reported on the right.

It is possible to notice that these spectra show sizable modulations which are typical of quantum dots with low aspect ratio and can be attributed to monolayer fluctuations in height [77, 143, 144].

I simulated the expected radiative recombination energies with the single-band constant-potential model, using realistic dot shapes from atomic force microscopy images with dimensions given by average values from the experimental size distribution. The results for the ground state transition are shown in Fig. 5.4 alongside the ensemble photoluminescence spectra. For the samples in which the substrate temperature during the quantum dots crystallization process was set equal or higher than 400°C, I found a largely lower and reproducible blueshift—around 30 meV—between the simple theoretical estimate and the centroid of the energy distribution. While the interdiffusion processes during the deposition of the capping layer are

probably still present, they have much more limited impact and the shape of the quantum dots most likely does not undergo dramatical changes. The ability to preserve the shape of the nanostructures and the reproducibility of the fabrication procedures are valuable assets for designing emitters for wavelength-specific applications.

The ensemble photoluminescence spectrum did not suffer from significant variations even after a post growth annealing performed at 700°C for 1 hour. This is in contrast to what observed on samples fabricated with the standard droplet epitaxy process. In that case, a large interdiffusion length has been reported and attributed to the high content of defects of the as-grown material [122]. I suggest that the high temperature procedure of quantum dot formation here presented reduces the concentration of point defects, which facilitate interdiffusion processes at post growth annealing temperatures and are also known to strongly contribute to spectral wandering [123].

However, as the temperature approaches the 520°C employed during the deposition of the AlGaAs barrier, a very intense As beam is required to get laterally confined dots taller than 6 nm. As shown in Fig. 5.5a, I observed that increasing the As flux above a certain threshold does not significantly affect the photoluminescence signal, hindering emission at the target wavelength of 780 nm. This behavior could be due to activation of a planar growth mechanism near the perimeter of the Ga droplet in presence of a sufficiently elevated As pressure. Since Ga adatom concentration can be quite high close to the droplet [145], incorporation of As adsorbed on the surface may take place despite its low residence time. Another factor which can play a role is a simple setup limitation, that is finite shutter opening time, reducing the effective As pressure during the first seconds of exposition.

An additional knob, that allows to tune the emission energy of these nanostructures, is the Al content in the barrier, which determines the height of the potential well. We reproduced a sample where dots are crystallized at elevated temperature and high As flux and reduced the Al content in the barrier from 30 to 15%, with the goal of lowering the energy of the optical transition. As shown in Fig. 5.5b, this successfully increases the emission wavelength up to 780 nm on the low energy tail of the distribution. In that spectral region, a convenient spatial density of emitters for single quantum dot studies is achieved, as it will be discussed later in this Sec. 5.2.

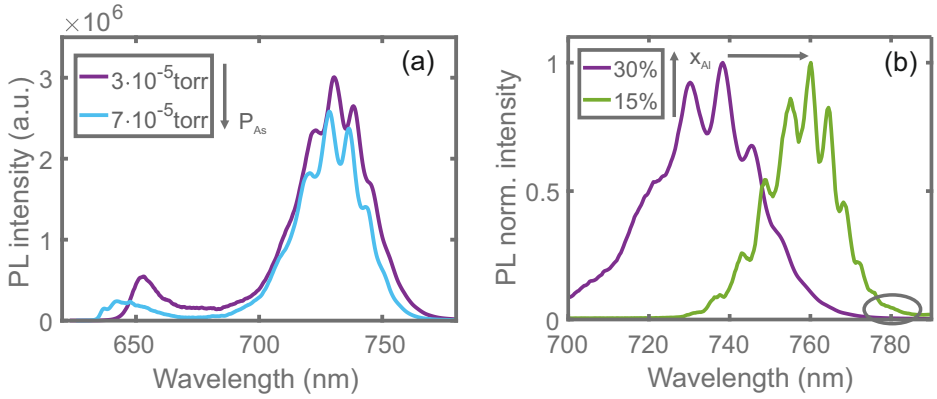

FIGURE 5.5: Comparison of the low temperature ensemble photoluminescence spectra between the sample emitting at the lowest wavelength from the previous series (row 5 of Table 5.2) and a modified version with: a) higher As flux during quantum dot crystallization; b) lower Al content in the barrier (row 7 of Table 5.2).

5.1.3 Self-assembly with good size uniformity

As described in Sec. 3.4, one of the remarkable features of droplet epitaxy is the possibility to decouple the control over spatial density and volume, set during Ga droplet deposition, from the one over shape, which depends on the crystallization step. Most of the activities presented in this thesis focus on the latter, because the main objective is to get high in-plane symmetry together with a specific confinement energy by tuning the aspect ratio and retaining shape homogeneity. On the other hand, the choice of Ga flux and temperature of the substrate during the formation of the droplets directly influences their spatial density, an important property when it is required to easily access the single quantum dot. At the same time, it can be noticed that both large area scans by atomic force microscopy and ensemble photoluminescence data from the previous section reveal a broad size distribution. This feature belongs to most self-assembly techniques and did not prevent us from obtaining the desired density needed to drive individual single-/entangled-photon emitters in a practical way.

Nevertheless, many applications would benefit from a tighter uniformity

of the nanocrystals. Several strategies to position quantum dots in arrays have been proposed, but no established solution up to now [146]. The reason is that these approaches often require cumbersome procedures and processing steps that result in poorer material quality.

While self-assembly on unpatterned substrates is an intrinsically random process, I want to demonstrate that the uniformity of the size distribution can be improved up to a certain extent by means of careful choice of the parameters of deposition. A sharp size distribution leads to a narrower ensemble photoluminescence peak that gives access to some optical properties relative to the single quantum dot, and I will mainly focus on this aspect.

We investigated in depth the formation of Ga droplets on an AlGaAs(100) surface, taking advantage of the broad experience already acquired from years of development of droplet epitaxy on this materials system and from related literature reports [147]. An extension of this study to (111)-oriented substrates is a promising future research direction, and this problem has only recently started to receive attention [148].

The spatial density of the quantum dots and their distribution of size and capture zone—the locus of points closer to a specific dot than to all the others, i.e. the Voronoi cell from which the dot captures Ga adatoms in first approximation—have been analyzed by means of atomic force microscopy in a wide parameter space of deposition. In particular, the substrate temperature was varied from 200 to 450°C and the Ga flux from 0.01 to 1 ML/s. Without entering a detailed discussion of the obtained results, I just concentrate on a specific set of conditions. Optimal results in terms of homogeneity for both size and capture zone dispersion were obtained at an intermediate temperature (around 300°C) and at a very low Ga flux (down to 0.02 ML/s). The analysis by atomic force microscopy is summarized in Fig. 5.6. Both distributions are narrow and regular enough to be adequately fitted with a single Gaussian curve. We achieved a standard deviation of capture zone areas of about 20%, whereas the standard deviation in the volume of the droplets is even lower, around 15%.

This behavior could be explained by an initial fast nucleation followed by a slow accretion. However, the kinetics of formation of the droplets is not trivial, and standard nucleation and accretion models predict the island size distribution to be equal or wider as compared to the capture zone distribution [149, 150], usually because of the presence of Ostwald

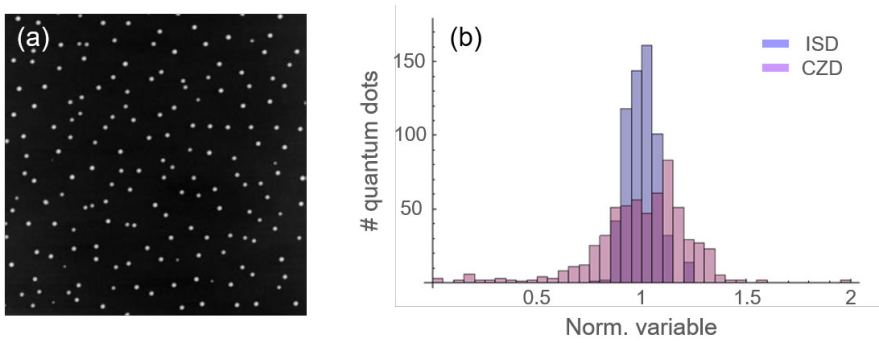

FIGURE 5.6: a) Atomic force microscopy images on a 5 x 5 μm^2 area of Ga droplets deposited at 300°C with a Ga flux of 0.02 ML/s. b) Histogram of the statistical distribution of normalized droplet volumes (island size distribution, ISD) and Voronoi polygon areas (capture zone distribution, CZD), same sample as panel (a).

ripening. A clear understanding of the formation of Ga droplets in a low Ga flux regime will require more sophisticate modeling. A possible explanation of the observed decoupling between volume and capture area may depend on the mobility of supercritical islands, especially during the initial stage of accretion, since this factor is usually overlooked in theoretical simulations.

A sample of quantum dots was fabricated using the protocol for uniform Ga droplets, in order to study their ensemble optical properties. A total quantity of 1.06 MLs of Ga was deposited onto a 30% Al content AlGaAs(100) surface at a temperature of 310°C with a Ga flux of 0.02 ML/s. The first monolayer just covers the As-rich c(4x4) reconstructed interface, whereas the droplets are formed by the remaining 0.06 MLs. The Ga droplets were then exposed to an As beam equivalent pressure of $5 \cdot 10^{-5}$ torr at 150°C for 3 min to crystallize into GaAs. Subsequently, the nanocrystals underwent a flash procedure, kept at 380°C for 10 min in an As pressure of $4 \cdot 10^{-6}$ torr. Finally, the quantum dots were covered with another layer of AlGaAs with 30% Al content, 10 nm deposited at low temperature followed by 140 nm at 580°C, and capped with 10 nm of GaAs.

I performed ensemble photoluminescence measurements on this sample. Figure 5.7a shows the spectrum at low temperature and low excitation

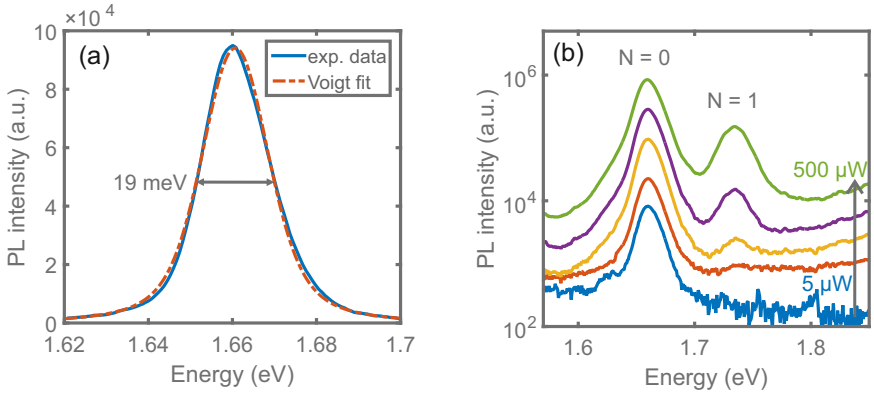

FIGURE 5.7: a) Ensemble photoluminescence spectrum of the emission of highly uniform quantum dots grown by droplet epitaxy, at 14K and low excitation power. The full width at half maximum of the emission energy distribution, obtained from a Voigt fit, is reported in the graph. b) Dependence of the photoluminescence spectrum on the laser power. The recombination from the ground and the first excited exciton states are labeled as N = 0 and 1 respectively.

power. In these conditions the emission peak reveals the energy distribution of ground state exciton lines. As expected from the good uniformity of morphological data obtained by atomic force microscopy on the Ga droplets, the emission band is symmetrical and narrow. The full width at half maximum is only 19 meV, a value that equals the state-of-the-art results obtained for self-assembled Straski-Krastanow InAs quantum dots [151]. Such a low inhomogeneous broadening in the quantum dot distribution allows to spectrally separate the ensemble emission features related to the ground and the first excited exciton state. Radiative recombination from the p-shell states of the quantum dots appears by increasing the excitation power as it can be clearly seen in Fig. 5.7b. The energies of the two transitions are consistent with a population of quantum dots with height of approximately 4 nm and a quite low aspect ratio, according to the prediction of the simple single-band effective-mass model implemented in Sec. 5.1.1.

As already mentioned, the narrow size dispersion allows to access some interesting physical properties from large area optical measurements. I

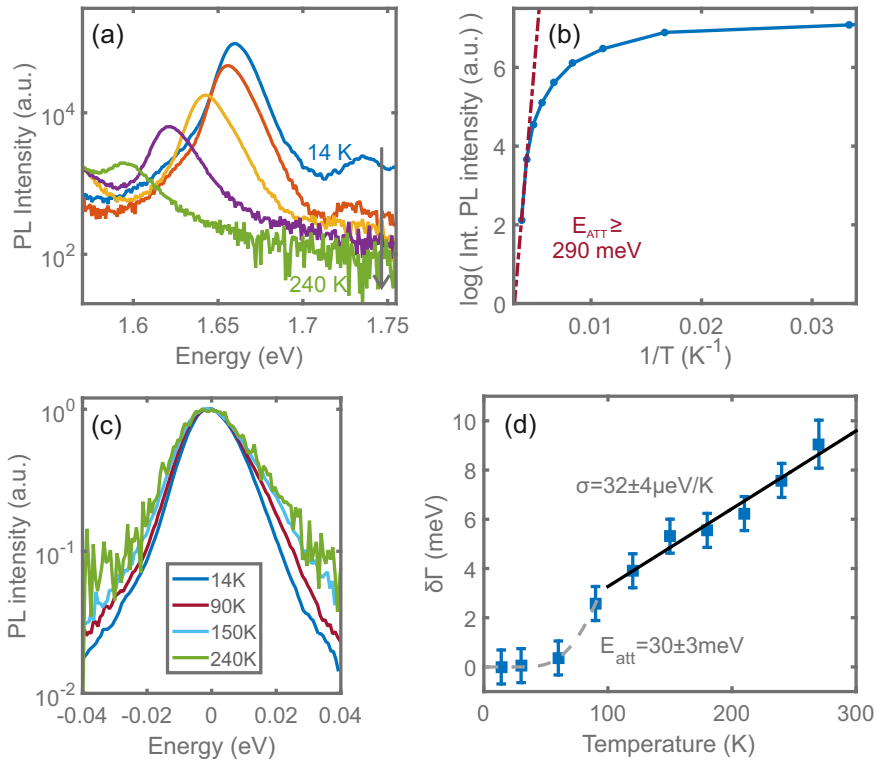

FIGURE 5.8: a) Ensemble photoluminescence spectra of the emission of highly uniform quantum dots grown by droplet epitaxy acquired at low excitation power while varying the temperature of the sample. b) Arrhenius plot of the integrated photoluminescence intensity of the exciton ground state transition. The lower bound slope of the signal quenching at high temperature is also plotted together with the corresponding activation energy. c) Ensemble photoluminescence spectra acquired at different temperatures normalized in intensity and centered in energy, in order to highlight the difference in spectral broadening. d) Broadening of the photoluminescence emission band with increasing sample temperature. Along with the experimental data (blue squares), an exponential fit at low temperatures (dashed grey line), interpreted as the zero-phonon line broadening mediated by optical phonons, and a linear fit at high temperatures, attributed to the contribution of the acoustic-phonon sidebands.

investigated the behavior of the photoluminescence emission at low laser power as a function of the temperature of the sample. Some of the acquired spectra are reported in Fig. 5.8a. With increasing temperature, a redshift of the transition energy is observed, which can be accurately described by the Varshni's law [152]. This behavior is expected for the electronic structure of a single quantum dot and can be observed in ensemble measurements in case the structure of the sample has no wetting layer. In the presence of a wetting layer, the occupation number of a quantum dot with a specific confinement energy is influenced by thermally activated dot–dot coupling and charge transfer. As a consequence, a sigmoidal dependence of the peak energy of the ensemble photoluminescence on the temperature of the sample is usually reported, which depends on both changes in the electronic structure and size-dependent carrier escape [153, 154].

In Fig. 5.8b I plotted the temperature dependence of the integrated photoluminescence intensity of the exciton ground state radiative recombination. In order to reliably monitor the radiative efficiency while increasing the temperature, the collection spot was kept in the same position compensating for thermal drifts, and at each temperature step the laser beam was focused again onto the sample so to maximize the photoluminescence signal. The high energy tail of the radiative recombination from the GaAs buffer and substrate layers was modeled as a decaying exponential function [104] and subtracted so to isolate the contribution due to the emission from the quantum dots. Using this procedure the measurement of the integrated photoluminescence intensity was quantitatively reproducible within 15%.

The quenching of the quantum dot emission in the high temperature limit is due to the thermally activated carrier escape. The slope of this curve depends on the binding energy of the carriers confined in the quantum dot, that is the activation energy required for the escape and the thermalization outside of the dot. The number of data points at high temperature shown in Fig. 5.8a is not sufficient to unambiguously identify the asymptotic behavior. However, an approximate lower bound of 290 ± 40 meV for the activation energy is estimated from the two measurements which are nearer to room temperature. This value is close to the binding energy of the exciton, which corresponds to the energy difference of 320 meV between the bandgap recombination peak of the AlGaAs barrier and the centroid of the quantum dot emission in the photoluminescence spectrum. Conversely, the

independent binding energy of the less strongly bound charge carrier, the heavy hole, is only approximately 150 meV according to the effective-mass single-band model. This piece of evidence suggests the presence of strong electron-hole correlations up to room temperature. In a consistent manner, I also observed a linear dependence of the quantum dot integrated photoluminescence intensity on the laser power density up to 240 K, a signature of correlation between the electron and hole populations in the quantum dot [155].

Another interesting effect I was able to notice thanks to the narrow size distribution was the broadening of the photoluminescence emission band with increasing temperature (see Fig. 5.8c). In order to quantify this phenomenon, I fitted the quantum dot photoluminescence spectra with a Voigt function and studied how the full width at half maximum of the Gaussian and Lorentzian components change with temperature [156]. While the Gaussian contribution does not vary significantly with temperature and can be attributed to the inhomogeneous energy distribution of the emitters, the Lorentzian one broadens as the temperature rises. In Fig. 5.8d I reported the increase in full width at half maximum of the quantum dot emission band as compared to the value measured at 14 K.

Since the inhomogeneous broadening of the quantum dot emission band due to size dispersion is temperature independent, these experimental data can be successfully explained as a result of phonon-exciton interaction.

At cryogenic temperature, the single dot spectrum is dominated by the zero-phonon line and its temperature dependence is described by Eq. 5.1: a constant term due to natural lifetime, charge and spin noise, plus a linear and an exponential term caused by inelastic scattering with acoustic and optical phonons respectively [157].

$$\gamma = \gamma_0 + aT + be^{-E_a/k_BT} \tag{5.1}$$

This regime corresponds to the temperature range below 100 K in Fig. 5.8d, where the energy resolution obtained by deconvolution of the ensemble emission band is insufficient to get a reliable insight about linewidth broadening. Despite that, the activation of scattering processes involving optical phonons can be qualitatively described. Moreover, the increase of the zero-phonon linewidth in this temperature range can be assessed by single dot

photoluminescence measurements.

On the other hand, higher temperatures are hardly accessible by single dot spectroscopy due to the decrease in brightness and to the spectral spread. The quantum dot emission is now dominated by broad phonon sidebands, which are caused by elastic exciton-acoustic-phonon interaction [158]. In order to experimentally study this phenomenon up to room temperature a more complex technique was used, namely four-wave mixing on stacked quantum dots [159]. The ability to investigate this regime allowed to find a linear dependence of the homogeneous phonon line broadening on temperature. Such a behavior was understood as resulting from a cut-off of the acoustic-phonon modes associated with the inverse of the localization length of the exciton.

The simple data analysis of ensemble photoluminescence employed in this section gives access to equivalent information. I was able to observe a linear increase of the width of the phonon sideband as well and to measure the related coefficient σ for a GaAs/AlGaAs three-dimensionally confined system. I report here a value of 32 ± 4 μeV/K, of the same order magnitude of the 20 μeV/K found for InAs/GaAs quantum dots. The difference could be explained as due to the larger conduction and valence band deformation potentials for GaAs with respect to InAs [160].

5.1.4 Single dot photoluminescence

In order to evaluate the prospects of the quantum dots presented in Sec. 5.1.2 as single or entangled photon emitters, it is now necessary to assess their individual properties. The electronic fine structure was investigated in detail by means of single dot photoluminescence. Following a similar approach to the one pursued in Sec. 5.1.2, I am about to describe how the growth parameters affect optical properties of the single emitter, such as exciton linewidth and fine structure splitting, that are relevant for our envisaged application. In particular, I will highlight the advantages introduced by the crystallization at elevated temperature and present an optimal strategy to meet the requirements for entangled photon pair generation.

Figure 5.9a shows a typical emission spectrum, dominated by four lines at low excitation power density. The presence of multiple peaks is a common feature for epitaxial nanocrystals in general, since different combinations of

charge carriers (see the discussion of the theoretical background in Sec. 3.2) may be present in the quantum dot while an exciton recombines radiatively.

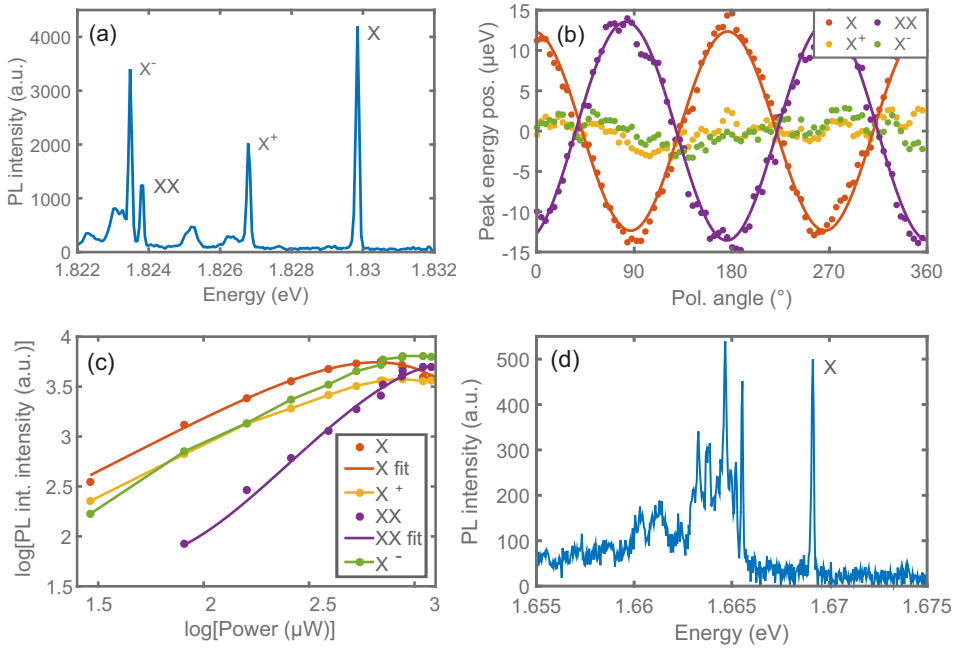

FIGURE 5.9: a) Photoluminescence spectrum of a typical quantum dot emitting in the short wavelength spectral region within an AlGaAs barrier with 30% Al content at moderate excitation power. b) Emission energy shifts of the lines shown in panel a, obtained by Gaussian fits of the spectra, as a function of the polarization angle. c) Power dependence of the photoluminescence intensities of the lines shown in panel (a), labeled consistently with the main text attribution, along with fits (continuous lines) for X and XX data points. d) Photoluminescence spectrum of a typical quantum dot emitting in the long wavelength spectral region.

Polarization-resolved measurements offer an effective tool to identify simple excitonic complexes. In most cases, the bright neutral excitons are two orthogonal linearly polarized states with a small fine structure splitting, induced by the electron-hole Coulomb exchange interaction [16, 68]. On

the other hand, such degeneracy breaking does not affect both charged exciton and biexciton fundamental states [15]. As in standard fine structure splitting measurements (see Sec. 4.2.2), I acquired linearly polarized emission spectra by rotating a half-wave plate in front of a linear polarizer. Fig. 5.9b traces the spectral position of the main emission peaks—extracted from a Gaussian fit—of the spectrum shown in panel (a) at different linear polarization angles. At specific orthogonal orientations it is possible to isolate the two non-degenerate bright exciton contributions and evaluate their energy separation. The same energy shift, yet with opposite sign, is observed for the photons emitted in the transition from the biexciton to the exciton state.

The emission peaks displaying this polarization signature are labeled in Fig. 5.9a as exciton (X) and biexciton (XX), the exciton being the more intense and higher energy line. The two remaining emission lines show no dependence on linear polarization and are interpreted as radiative recombination from trion states (X^+, X^-). This picture is consistent with previous experimental studies [103] as well as with atomistic many-body pseudopotential calculations [100] of GaAs/AlGaAs droplet epitaxy quantum dots. In particular, I rely on previous considerations on residual doping, analysis of the degree of circular polarization after circularly polarized pumping [99], and charge tuning through electrical injection [161] to tentatively attribute a sign to the charged exciton transitions.

The power dependence analysis supports the proposed interpretation, as the biexciton radiative recombination shows a clear quadratic dependency on the injection rate as compared to the linear one of the exciton line. I have quantitatively demonstrated this using a random population model, where the photoluminescence intensity of the exciton and of the biexciton line follows a Poissonian dependence on the average occupation number inside the quantum dot and on its square power respectively [109, 162]. Numerical fits find good agreement with theory (the experimental data points along with the fitted curves are shown in Fig. 5.9c) and properly estimate a near-one exponent in the power law for the dot population process. The difference between the fitting parameters for the exciton and biexciton power dependence curves is within the experimental error. The power dependence of the charged excitons emission on the photoinjected population may vary from linear to superlinear, as in the case of positively

and negatively charged exciton respectively in Fig. 5.9c, depending on the leading capture mechanism of the extra charge.

If we consider quantum dots with lower confinement energy, this simple picture is usually not enough to describe the excitonic spectrum even at low power, as I usually observe more than four peaks, as shown in Fig. 5.9d. These lines most likely come from other charged and multiexcitonic states, which are expected to recombine radiatively at intermediate powers, before the onset of a multiexcitonic broadband due to transitions involving continuum states [100, 163]. A deeper potential barrier in a weak lateral confinement regime leads to a larger number of confined levels, hence a higher probability to find a carrier in an excited state or an extra charge captured by tunneling from energetically aligned defect states. The presence of a few multiexcitonic peaks spectrally overlapping has already been reported for GaAs/AlGaAs nanostructures emitting at long wavelengths, but grown with a different epitaxial technique [19]. However, it has also been shown that the biexciton radiative recombination can be singled out effectively by recurring to a resonant excitation scheme.

Nonetheless, I am able to describe how the binding energies of positive and negative trions, as well as of the biexciton, vary as a function of the confinement energy, thanks to the ability to cover a large spectral range of emission. The results, reported in Fig. 5.10, highlight that the main features resemble the behavior observed on similar quantum dots grown on different substrate orientations [99]. However, I found some interesting major differences, such as the absence of a transition to an unbound state for the positive exciton or the presence of a maximum binding energy for the biexciton state. These discrepancies are arguably a signature of the peculiar shape—a truncated pyramid with an hexagonal/triangular base, as deduced from atomic force microscopy morphological information on uncapped samples—which has an important impact on the excitonic emission spectrum [100]. A high biexciton binding energy is an asset for the two-photon resonant excitation scheme, in which the biexciton state is directly pumped to efficiently trigger the cascade, and backscattered laser light must be spectrally filtered [164].

Once it is possible to unambiguously identify the neutral exciton line, we can proceed and address the most relevant properties of the quantum dot

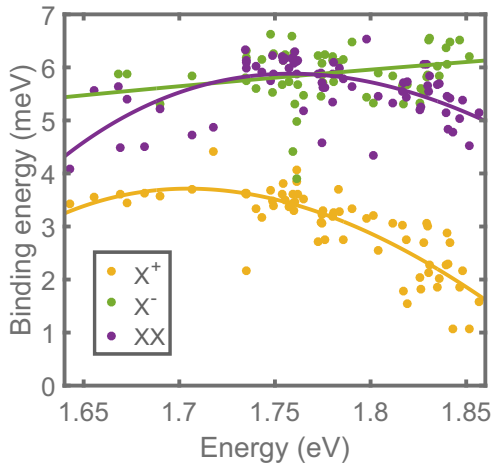

FIGURE 5.10: Binding energies of the excitonic complexes as a function of the emission wavelength, 30% Al content in the barrier.

as a light emitter. The linewidth measured at liquid helium temperature—so that the contribution of phononic sidebands is heavily reduced—is an important figure of merit that quantifies the presence of spectral diffusion [165]. Most quantum information protocols [9, 13, 38] require photons emitted at different times to interfere with each other, hence a Fourier-limited (linewidth limited by natural lifetime) single-photon emitter would be highly desirable. I looked into how to reduce the impact of spectral wandering sources. A complete understanding of the phenomena behind the broadening of the zero-phonon exciton line is a very complex problem, but charge noise, that is time-varying Stark shifts induced by localized charges trapped in defects in the surroundings of the quantum dot, is commonly the dominant contribution [106–108, 121, 166]. While sources of spectral diffusion are in practice hard to completely suppress, I found that several growth and structural parameters have an impact on the average exciton linewidth.

Table 5.3 reports the average linewidth values of the exciton zero-phonon line for a list of samples. This value is obtained by extracting the full width at half maximum from a Gaussian fit performed on spectral

TABLE 5.3: Average linewidth (FWHM) and fine structure splitting (FSS) values, evaluated on emission lines unambiguously identified as neutral excitons, are reported for a list of samples differing for thickness (d) of the AlGaAs barrier (defined as the distance between the quantum dots and both the GaAs buffer and the semiconductor-air interface), Al content (x_{Al}) in the barrier and substrate temperature (T_{sub}) during the droplet exposure to As.

d(nm)	x_{Al}(%)	T_{sub}(°C)	FWHM(μeV)	FSS(μeV)
50	30	200	250	30
50	30	400	130	21
50	30	500	170	24
50	30	520	150	22
50	15	500	130	17
100	30	400	100	16
100	15	400	80	12
100	15	500	60	10
150	15	500	<40	-

features which could be reliably identified as neutral exciton lines. The measurements were performed under above-barrier excitation.

The first five entries of the table compare the samples studied with ensemble photoluminescence, previously presented in Sec. 5.1.2. These samples were fabricated in consecutive depositions, in order to assure the conditions in the MBE chamber to be as stable as possible. If we consider the fact that the lowest optical quality is observed in the case where the crystallization of the quantum dots was performed at 200°C instead of 400°C or more, it emerges that a higher crystallization temperature is actually a successful strategy to reduce spectral diffusion. This is a major improvement with respect to the standard droplet epitaxy technique, where the constraint of a low temperature during exposure of the droplets to As results in a poor crystalline quality, which can be mostly, yet not entirely, compensated by post growth thermal annealing processes [122]. We tried to perform a post growth rapid thermal annealing on these samples as well, performed at 700°C for 1 hour, but in this case the treatment has brought no improvement of optical quality. On the contrary, the average single dot excitonic linewidth

has increased consistently on all treated samples. A possible explanation for the detrimental effect is the formation of defects at the semiconductor-air interface that act as charge traps and ultimately cause spectral wandering.

Since transient electrostatic fields from surface charges at the vacuum-semiconductor interface have already been pointed out as a major cause for spectral wandering in GaAs/AlGaAs droplet epitaxy quantum dots grown on (100) substrates [121], we reproduced the best performing samples with thicker AlGaAs layers in order to increase the distance between dots and free surface. The comparison of the average full width at half maximum values of the neutral exciton line, reported in Table 5.3, confirms that this effect is indeed significant. A thick enough AlGaAs barrier, at least 100 nm above and under the quantum dots, allows to get resolution-limited (below 40 μeV) lines.

The As flux chosen during the process seems to play a role as well, with an optimal range of pressures which depends on the temperature of the substrate, but in this case the studied parameter space is not rich enough to draw safe conclusions. If only the samples with the thicker AlGaAs barrier are compared, it is possible to notice an improvement in the average linewidth and in the fraction of resolution limited lines for smaller Al content in the barrier. Reasonably, when GaAs is grown at a temperature high enough to get a good crystal and interface effects are reduced to secondary, the crystalline and optical quality of the AlGaAs layers is the prevalent factor affecting exciton linewidth. Since at a fixed temperature the AlGaAs quality is known to get worse with increasing Al content [90], I suggest that this could bear a side advantage for the 15% Al composition in addition to the previously discussed role in emission wavelength tuning.

Under optimal conditions, I observed the majority of exciton lines being below the resolution of the experimental setup, 40 μeV, even without recurring to a resonant excitation scheme. Since the lowest linewidth value is still probably limited by electrostatic effects induced by carriers trapped in the AlGaAs barrier, resonant excitation could succeed in further suppressing spectral wandering [15, 166], by reducing the density of carriers excited close to the exciton confined in the quantum dot. Further investigations will be needed to tackle this point.

Table 5.3 also presents the values of fine structure splitting obtained by

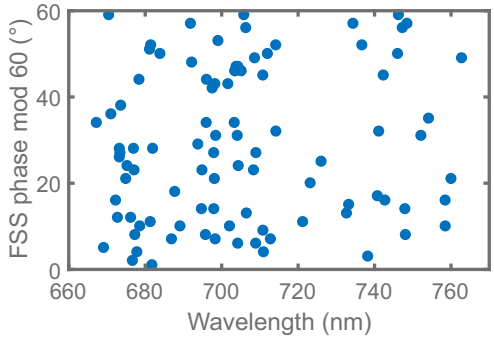

FIGURE 5.11: Polarization of the higher energy bright exciton state with respect to [1-10] (or an equivalent direction rotated around the z axis by 60°) as a function of emission wavelength, collected from a series of samples with 30% Al content in the barrier.

means of polarization resolved measurements, averaged on a collection of quantum dots emitting at different wavelengths for each sample. As it was thoroughly discussed in Sec. 2.3, this figure of merit is relevant for assessing the potential of a quantum dot as an entangled photon emitter. The morphology analysis provided by atomic force microscopy on uncapped samples, that I presented in Sec. 5.1.2, confirms the improved symmetry of droplet epitaxy performed on (111) substrates, as no in-plane elongation is present unlike the case of (100) orientation [103]. The fine structure splitting statistics is consistent with this picture as the average energy separation is strongly reduced and the emitting dipole shows no preferential in-plane orientation, as clear from Fig. 5.11. Similar results have already been reported for droplet epitaxy quantum dots grown on high symmetry substrates [77].

However, in this work, I was able to cover a larger spectral range of emission, thanks to the control over the shape and the potential barrier. Each sample displays a relatively weak dependence on the confinement energy as compared to Stranski-Krastanow InAs quantum dots [68], arguably related to the possibility to decouple the size and shape distributions in a kinetically driven epitaxial technique such as droplet epitaxy. Despite that, in the previously unexplored high emission wavelength region, the average fine structure splitting is further reduced, down to less than half of the previous

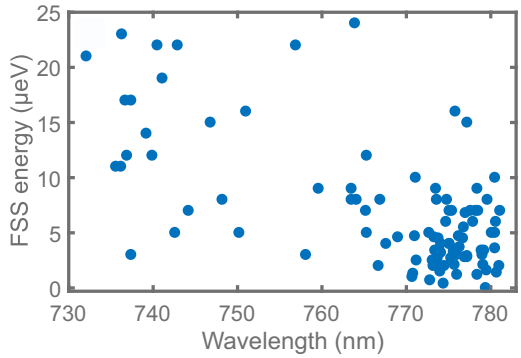

FIGURE 5.12: Fine structure splitting as a function of emission wavelength, collected from the samples whose spectral window reaches 780 nm (rows 8–9 of Table 5.3).

best report for this fabrication method [27]. For the samples where such a low figure of merit was observed (rows 8–9 of Table 5.3), the fine structure splitting energies as a function of emission wavelength are reported in Fig. 5.12 (see a more detailed discussion of this result in the next section). The key improvement has to be attributed to the taller geometry of the quantum dots, possibly because their shape is less affected by monolayer fluctuations in the substrate. An alternative explanation could rely on the magnitude of electron-hole exchange interaction, which is weaker in systems where carrier localization is less strong. This hypothesis has been demonstrated theoretically and experimentally for another family of GaAs quantum dots [167]. Conversely, lower fine structure splitting was found in smaller quantum dots grown by droplet epitaxy on the (100) surface [103], but that behavior could be attributed to the size-dependent in-plane elongation instead.

An unexpected insight offered by Table 5.3 concerns the qualitative relationship between the optical quality and the energy separation between the bright exciton states. Indeed, a positive correlation is observed between average values of zero-phonon linewidth and fine structure splitting. The same correlation holds up if we consider the data point distribution on each sample individually. It is non-trivial to give a straight explanation to this

observation. A worse control on the material crystalline quality, while fostering an electrically noisy environment that disturbs the excitonic coherence, also appears to be related to random local anisotropies in the confinement potential, which are assumed to be the cause of non-vanishing fine structure splitting in quantum dots grown on highly symmetrical substrates.

Another optical property which strongly affects the entanglement fidelity of a pair of photons emitted in a biexciton-exciton cascade is radiative lifetime (see Sec. 2.3.1 for theoretical background). Time-resolved measurements are called for to complete the characterization of our quantum dots.

Figure 5.13a shows the time decay of the photoluminescence intensity of a neutral exciton line. The excitation power was tuned below the saturation level of the exciton in order to prevent band filling effects. In such conditions, the experimental data can be described quite accurately by the convolution of the instrument response function with a single exponential decay. This approach returns the total decay time of the system, which does not translate plainly into a radiative lifetime, since the processes which populate the exciton and non-radiative decay channels also enter the rate equations. However, in a high quality epitaxial quantum dot at low temperature, it can be assumed for simplicity that the spontaneous radiative recombination is dominant over non-radiative mechanisms [168]. In this way, I estimated the radiative lifetime as approximately given by the time constant obtained from the exponential decay of the photoluminescence signal.

As an attempt to support this assumption, I adopted a simple model which has been recently developed and successfully applied to time-resolved photoluminescence measurements on standard droplet epitaxy GaAs quantum dots [169]. The photoluminescence signal decay is fitted with a double exponential decay, where the slower decay comes from carrier transfer from dark exciton states and contains information about the non-radiative decay rates. I used this model to interpret the measured decay curves, which actually exhibit a weak and slower contribution, and I obtained an average intrinsic quantum efficiency of 88%, which is clearly consistent with the hypothesis that radiative recombination is the dominant decay process inside the quantum dot.

The radiative lifetime has been evaluated from the single exponential decay time over a series of several different quantum dots (see Figure 5.13b)

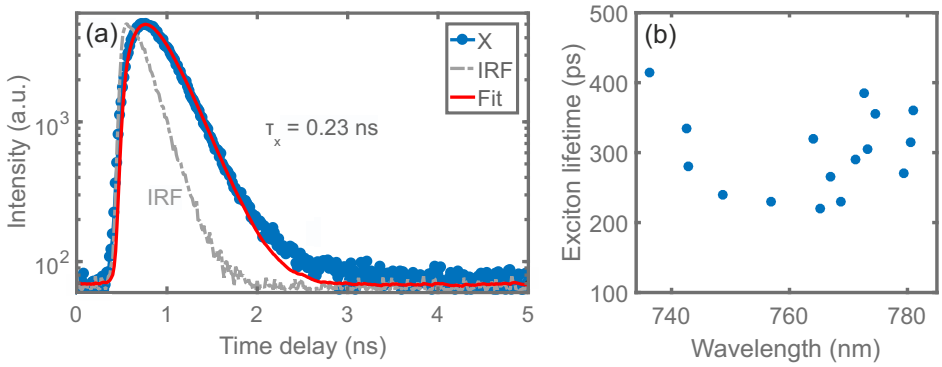

FIGURE 5.13: a) Example of time-resolved photoluminescence decay of an exciton line (blue curve with circles). Also the instrument response function (IRF, gray dashed curve) is shown as well as the fit (red continuous curve) performed by convoluting the IRF with a simple exponential decay. b) Lifetime values estimated under above-barrier excitation on quantum dots emitting at different wavelengths, on a sample with 15% Al content in the barrier.

and a short average value of 300 ps was found using above-barrier excitation. This quantity depends rather weakly on emission wavelength over a broad range from 740 to 785 nm. The radiative decay of these nanostructures is fast, partly thanks to the relatively high transition energy, near the visible range [170], partly because of the large lateral dimensions compared to the exciton Bohr radius, despite not being fully in the scenario of giant oscillator strength [111, 112].

The lifetimes reported are shorter with respect to unprocessed (with no cavity enhancement, as in the studied case) In(Ga)As quantum dots—see well known reference values for self-assembled nanocrystals around 800 ps [170, 171], as well as more recent data on systems where successful entangled photon emission was reported: 1000 ps on Stranski-Krastanow dots [172] (400 ps with resonant excitation [164]), 1800 ps on inverted patterned pyramids [81], 500 ps on dots in InP nanowires [80]—and the latest generation of droplet epitaxy GaAs/$Al_{0.3}Ga_{0.7}As$ quantum dots with highest crystalline and optical quality—1000 ps on standard (100) substrates [123]

and 560 ps on (111) substrates [27], whereas shorter total decay times between 500 and 150 ps were reported in previous studies [110]. The radiative lifetimes of the quantum dots investigated here are close to the best values reported for GaAs droplet etching quantum dots, that are around 200 ps under quasi-resonant p-shell excitation [173].

Resonant excitation is indeed a viable way to further decrease the reported values, because the temporal duration of the decay processes that populate the exciton state of the quantum dot may not be negligible on the considered timescale.

5.2 Single dot optical spectroscopy near 780 nm

During the previous section, I analyzed the main features of single dot spectroscopy as a function of the growth parameters and looked into how to improve relevant figures of merit associated to the generation of polarization-entangled-photon pairs. Here, instead, I focus on the sample achieved as a result of this optimization process (last entry in Table 5.3) and investigate more in detail the performance of single-/entangled-photon emitters in the spectral region near 780 nm for operation in combination with Rb vapor cells.

Emission near 780 nm is achieved by quantum dots in the high side of the size distribution, like the one profiled in Fig. 5.14a. Spatial microphotoluminescence imaging over a 100 x 100 μm^2 area found more than 50 emitters with a neutral exciton line at less than 2 nm from 780 nm. Within this spectral distance is possible to apply an external field (check introduction of Ch. 6 for a list of available implementations) and tune the emission energy in the large dispersion region between the D_2 lines of ^{87}Rb.

In Fig. 5.14b I reported a typical spectrum, which is characterized by an intense and narrow neutral exciton line, accompanied by few peaks at positive binding energies from the radiative recombination of other exciton complexes. Like in the case previously described in Fig. 5.9d, the biexciton cannot always be singled out spectrally. From spectra in which it can be identified in polarization-resolved measurements, a binding energy of 3.7 meV (0.3 meV standard deviation, 1.9 nm wavelength separation) is obtained.

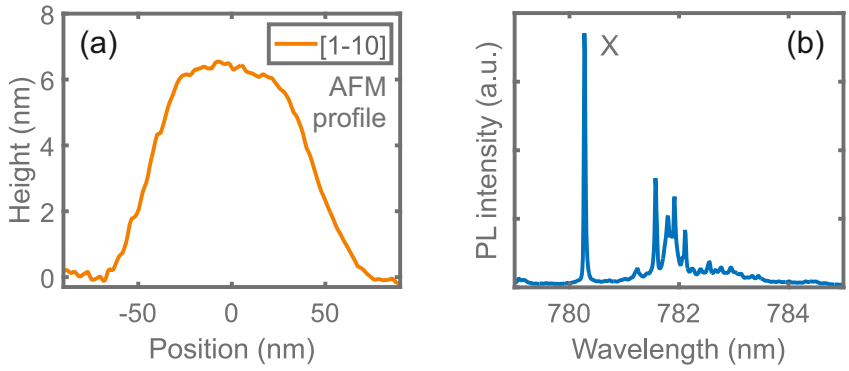

FIGURE 5.14: a) Height profile probed by atomic force microscopy on an equivalent uncapped sample of a quantum dot compatible with emission at 780 nm. b) Photoluminescence spectrum of a typical quantum dot emitting near 780 nm.

Light emission near 780 nm shows desirable features with respect to both spectral wandering and fine structure splitting. The majority of neutral exciton lines display a linewidth below the resolution of the spectrometer (40 μeV). In order to quantify the residual level of decoherence broadening and compare it with the Fourier limit, a much more sensitive technique is needed. Therefore, I performed a series of coherence time measurements by means of a Michelson interferometer (see Sec. 4.2.3). I investigated several neutral exciton lines below the spectrometer resolution and fitted their visibility decay as a function of Michelson path difference with an exponential decay, as shown for example in Fig. 5.15a.

This model assumes a Lorentzian line broadening, which implies that spectral diffusion effects are small and fast enough to fall in a motional narrowing regime [107] and comply with a description of dephasing based on homogeneous mechanisms, namely charge and spin noise in addition to the natural linewidth [166]. A minor Gaussian contribution to decoherence broadening is actually present and using a Voigt curve for the fit improves its quality in the first few tens of ns of delay. However, the normal component of the Voigt is always secondary and increasing the complexity of the model does not significantly affect the estimation of the linewidth. The

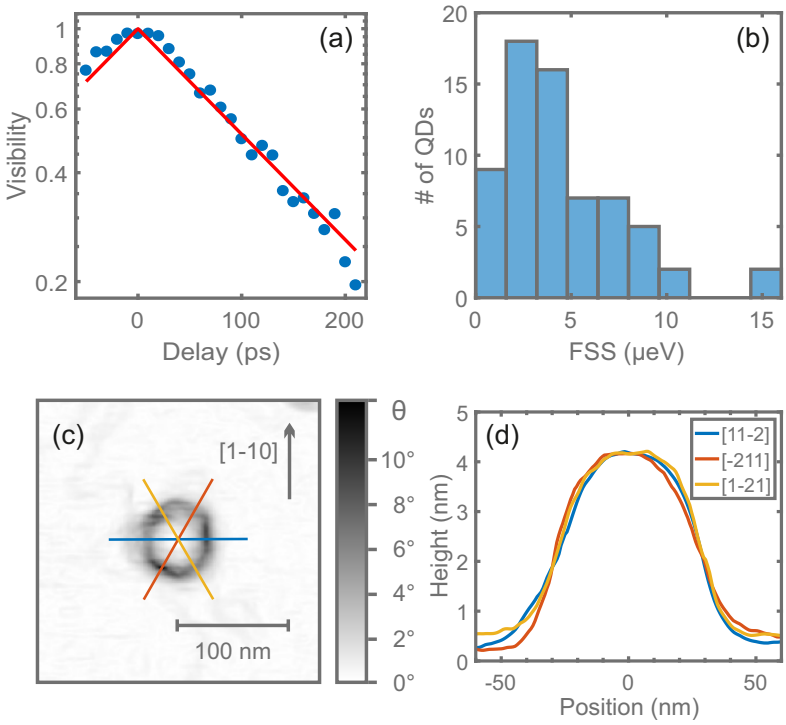

FIGURE 5.15: a) Interference visibility of the neutral exciton line from a selected quantum dot (blue dots) fitted with a single exponential decay (red curve). b) Histogram of fine structure spitting values measured on a series of quantum dots emitting between 770 and 785 nm. c) Atomic force microscopy map of a typical single quantum dot, color scale proportional to the inclination angle with respect to the (111)A plane. d) Height profiles taken along [11-2] and equivalent crystallographic directions on the same quantum dot as in panel (c) (see colored lines).

Lorentzian fit immediately yields the exciton coherence time, that can be easily translated in terms of spectral broadening [128].

The measured average neutral exciton linewidth is 15 μeV with a best value of 9 μeV, which is an improvement over previous reports where the droplets are crystallized at 200°C [138]. The result is state-of-the-art for droplet epitaxy [174, 175]. Given the measured radiative lifetimes, spectral diffusion can reach down to three times the Fourier limit, which is a very satisfying achievement for above-barrier excitation [15, 166].

Since the fine structure splitting does not appreciably vary above 770 nm (see Fig. 5.12), I studied its distribution in this spectral region and collected the values in the histogram reported in Fig. 5.15b. As in the case of all other probed samples, no preferred orientation of the in-plane emitting dipole was observed, a behavior compatible with the absence of systematic anisotropies in the shape of the quantum dots. Averaging the fine structure splitting over 66 neutral exciton lines yields a very low value of 4.5 μeV with a standard deviation of 3.1 μeV. Such a figure is comparable with other state-of-the-art epitaxial systems on which entangled photon emission has been observed without the need for external fields or temporal post-selection: 10 μeV for previous reports of droplet epitaxy GaAs dots on a (111)A substrate [27], 4 μeV for droplet etching GaAs dots [20, 176], 2 μeV for inverted patterned $InGaAs_{1-\delta}N_{\delta}$ pyramids [81, 177], 3.5 μeV for InAsP/InP dots in a wire [80], 5-10 μeV for InAs self-assembled Stranski-Krastanow nanostructures at very specific energies where the sign of the splitting is inverted [69]. In addition to that, a correct evaluation of the potential for entangled photon generation requires to consider fast radiative recombination and slow spin scattering as well, as it will be discussed more in detail in Sec. 5.3.

The low values of fine structure splitting achieved are consistent with the high in-plane symmetry found in morphology maps by atomic force microscopy. Figure 5.15c shows a truncated pyramid shape with a regular hexagonal base, which is compliant with C_{3v} symmetry, as further demonstrated by the comparison of height profiles along equivalent crystallographic directions in Fig. 5.15d. The appearance of a rounded top may be due to the limited resolution of the instrument, that in this case does not resolve atomic steps on the dot. The collection of scans performed by atomic force microscopy are instead compatible with a flat top picture.

5.2.1 Resonant two-photon excitation

The single dot emission properties presented in the main section are very promising for the generation of polarization-entangled photon pairs. At the same time, a possible hurdle was pointed out, namely the presence of several exciton complexes whose radiative recombination competes with the biexciton-exciton cascade decay channel. In this section, I will deal with this problem using a resonant two-photon excitation scheme, tested for the first time on droplet epitaxy quantum dots. The concept was developed in Ref. [164], and it consists in exciting the quantum dot with a pulsed laser, whose emission is tuned half the way between the exciton and biexciton recombination energies. The physical process is sketched in a simple energy diagram in Fig. 5.16a. The energy of the pump stays below the linear absorption threshold of the barrier material and of the exciton state in the quantum dot, while matching resonantly the two-particle energy of the biexciton state. This approach offers a way to selectively initiate a biexciton-exciton cascade, an important step forward in the direction of on-demand generation of an entangled photon pair.

The time duration of the laser pulse must be adjusted carefully, since it must be short enough to prevent the system from being excited twice by the same pulse, but, on the other hand, it must be quite narrow spectrally so to not spectrally overlap with the exciton and biexciton lines. Therefore, I used a Ti:sapphire tunable pulsed laser with a nominal pulse duration of 100 fs and broadened it by means of a 4f pulse-shaper to about 10 ps. This value is safely below the biexciton radiative recombination time and, at the same time, I was able to suppress laser backscattering by placing tunable notch filters with a bandwidth of 0.4 nm in the collection path.

Figure 5.16c shows the spectrum of a quantum dot excited with this approach. In contrast with the spectrum excited non-resonantly above the barrier band gap, reported in Fig. 5.16b, the exciton and biexciton lines present similar brightness, which is an expected characteristic of a dominant radiative recombination through the biexciton-exciton cascade. While a signature from a trion state is still present, even if weaker, this resonant process effectively suppresses radiative recombination from other multiexcitonic complexes, that reduces the number of useful recombination events for entangled photon generation.

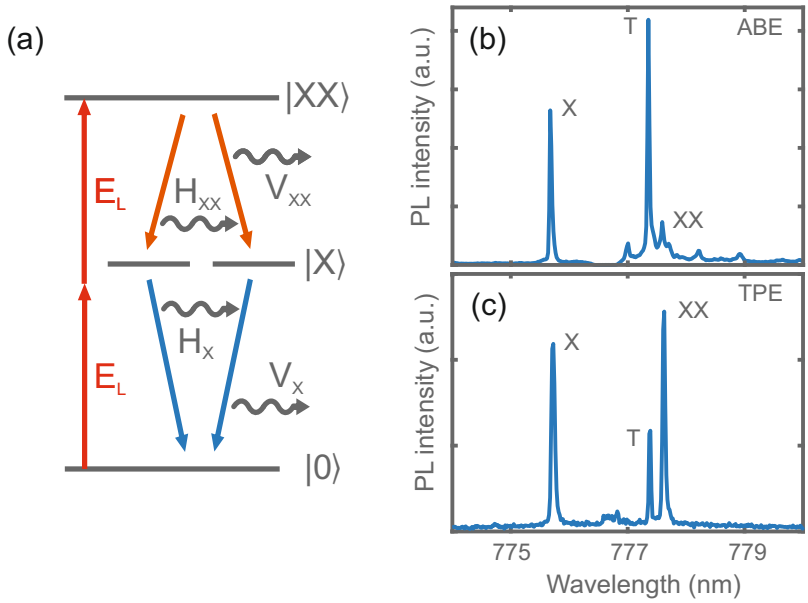

FIGURE 5.16: a) Energy diagram which describes the non linear excitation of the biexciton state via a virtual state at half of its two-particle energy and the subsequent decay with emission of a pair of photons correlated in polarization. b) Photoluminescence spectrum of a typical quantum dot under above-barrier excitation (ABE). c) Photoluminescence spectrum of the same quantum dot shown in panel (b) under resonant two-photon excitation (TPE).

In order to achieve this result, a minor adjustment to the growth protocol was necessary, namely the use of an intrinsic GaAs substrate. Tests performed on samples prepared with a n-doped substrate were hindered by the presence of an incoherent channel of charge capture by the quantum dots. In particular, a faint emission spectrum with a broad multiexcitonic band was observed, characterized by a flat and non-resonant dependence on the laser wavelength. While it is not obvious to describe how carriers photo-excited in the substrate could diffuse into the quantum dots, I observed a strong hot luminescence from GaAs, extending up to the emission range of the quantum dots. Formation of highly energetic carriers could

also be fostered by non-linear effects, such as Auger recombination.

This behavior can be interpreted as a consequence of the large laser power density employed. In contrast to linear absorption, two-photon excitation is a third-order non-linear optical process with a much lower probability cross-section. Indeed, in order to reach the maximum brightness of the exciton line a power almost three orders of magnitude higher with respect to the case of above-barrier excitation is needed. Specifically, the laser power on the sample is of the order of 10–20 μW, in combination with the strong focusing of a 0.42 NA objective and a solid immersion lens. The use of an intrinsic substrate or its removal by processing (see Ch. 6) resulted in a successful suppression of the secondary incoherent pumping process.

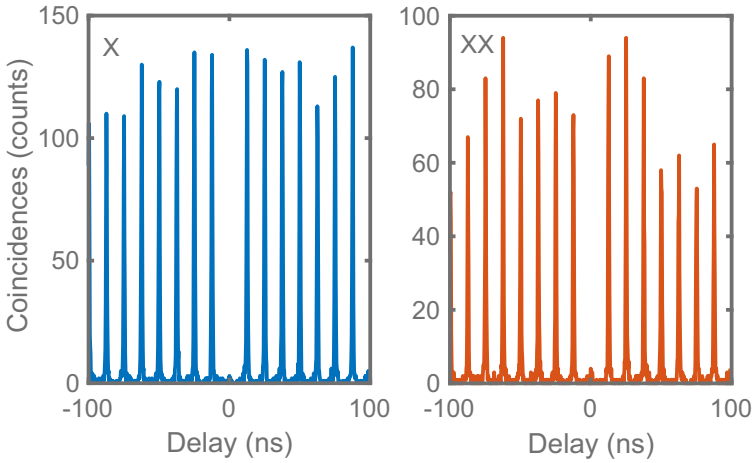

FIGURE 5.17: Autocorrelation coincidence measurements of the X and XX lines of a typical quantum dot, under resonant two-photon excitation at π-pulse.

The use of a pulsed laser together with the selective excitation of the biexciton state result in an elevated single-photon purity. This has been demonstrated by means of autocorrelation measurements performed with the Hanbury Brown–Twiss setup described in Sec. 4.2.4. Figure 5.17 shows the presence of a strong anti-bunching at zero time delay for both the exciton and biexciton transitions. In particular, I could estimate values of $g^{(2)}(0)$ equal to 0.03 ± 0.01 and 0.05 ± 0.02 for the X and XX line respectively, after

dividing the integrated intensity of the zero time delay peak by the average of the side peaks. I calculated the error assuming Poissonian statistic on the number of coincidence counts from the avalanche photodiodes. The $g^{(2)}(0)$ values reported are close to the noise level of the acquisitions and can be mainly ascribed to incomplete suppression of the laser light backscattered from the sample. This is an important result, since achieving a high single-photon purity is one of the essential requirements for on-demand operation [25].

A even more compelling evidence supporting the successful implementation of a two-photon excitation process of the biexciton state comes from the direct spectroscopic assessment of the resonant and coherent behavior of the optical absorption.

In Fig. 5.18a it is shown a photoluminescence excitation spectrum of the X and XX lines relative to the quantum dot discussed in Fig. 5.16. As expected, a clear resonance is found for both the emission peaks when the laser line is set to a wavelength exactly in between of the two transitions. The linewidth of the resonance curve does not correspond to the one of the exciton state, but it is mainly dictated by the spectral width of the laser pulse.

Figure 5.18b demonstrates the onset of a coherent excitation process. The dependence of the photoluminescence integrated intensity of the X and XX emission lines does not show a monotonic rise followed by saturation, instead it is denoted by the presence of clear of Rabi oscillations [178]. All the following experiments in two-photon excitation regime are performed at π-pulse, that is the pumping power at which the inversion of the quantum dot from the ground to the biexciton state is most probable.

The ability to directly excite the biexciton state also has an influence on time resolved measurements. Even if I have collected just a few data points, all the studied quantum dots have an exciton radiative lifetime which falls below 240 ps under resonant two photon excitation. A time-resolved photoluminescence decay is plotted in Fig. 5.18c and it can be accurately modeled as a single exponential curve convoluted with the instrument response function. The lifetime of the biexciton is just 78 ps, about half of the one relative to the exciton, because a double amount of decay paths is available. These figures are even lower than what previously reported in Sec. 5.1.4. This implies that the process of thermalization of

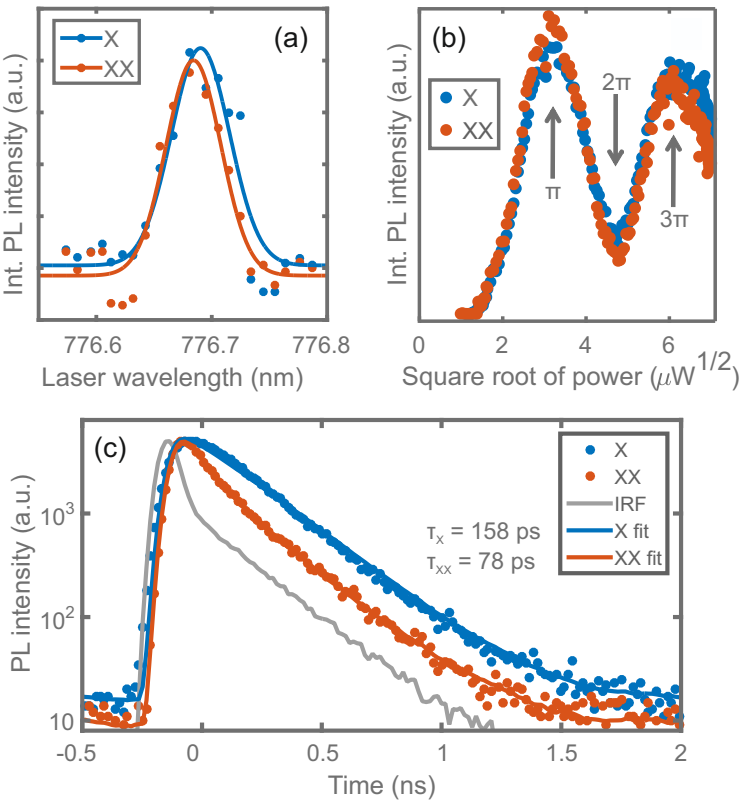

FIGURE 5.18: a) Integrated photoluminescence intensity of the X and XX lines from Fig. 5.16c as a function of the emission wavelength of the laser, along with Gaussian fits of the resonance curve. b) Integrated photoluminescence intensity of the X and XX lines from Fig. 5.16c as a function of the square root of the excitation power of the laser. Rabi oscillations are marked by arrows. c) Time-resolved decay of the photoluminescence intensity relative to the X and XX lines of a selected quantum dot. The experimental data are fitted with a single exponential decay convoluted with the instrumental response function (IRF, also shown). The decay time constants obtained from the fit are reported in the graph.

the photo-excited carriers from the AlGaAs barrier down to the exciton ground state gives a non-negligible contribution to the total decay time of the system. Therefore, the decay constant of a time-resolved measurement under resonant excitation gives a more accurate estimate of the lifetime of the intermediate exciton state in a biexciton-exciton cascade, a fundamental parameter to quantify dephasing due to a finite fine structure splitting (see Sec. 2.3.1).

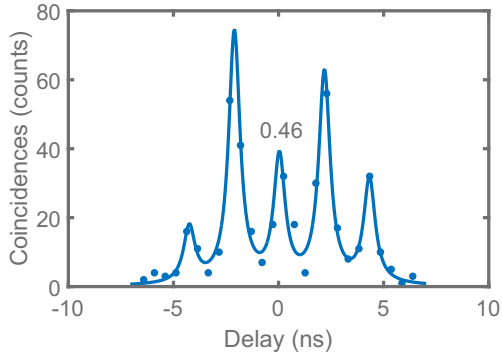

FIGURE 5.19: Hong-Ou-Mandel interferogram of the neutral exciton line from a randomly chosen quantum dot, under resonant two-photon excitation at π pulse. The dots indicate the histogram of the coincidence counts (0.512 ns time bin), whereas the continuous line is the fitted curve. The visibility of the zero delay peak without any correction for the beamsplitter asymmetry and the background light is reported in the graph.

The use of a pulsed and resonant excitation scheme also facilitates the study of photon indistinguishability from a single-photon emitter [57, 179]. A Hong-Ou-Mandel experiment of two-photon interference was performed on a randomly chosen quantum dot (see Fig. 5.19) using the setup described in Sec. 4.2.5 with a 2 ns Mach-Zehnder delay line and a non-polarizing 50:50 beamspitter. I fitted the temporal pattern of coincidence counts with the sum of five Gaussian curves with the same full width at half maximum and then calculated the visibility according to Eq. 4.5. Without keeping into account corrections for the non-ideality of the beamslitter and for the background light, I obtained a value close to 0.5.

This figure is still inadequate for many quantum optics experiments, but it can be a promising preliminary result. Higher visibility could be obtained by pre-selection of the quantum dot based on the coherence time measured with Michelson interferometry. More sophisticated approaches rely on control of the charge environment of the quantum dot, by means of optical trap filling or an electric field, and on the Purcell effect in a resonant microcavity.

The addition of a weak white light source, a quite common strategy to improve visibility of resonantly excited quantum dot by stabilizing its charge environment [180–183], resulted in no appreciable effect on the emission spectrum of the droplet epitaxy nanostructures here investigated.

5.3 Entangled photon emission

The process of optimization of the growth protocol has lead us to reach excellent figures of merit for entangled photon emission in terms of fine structure splitting, exciton lifetime and single-photon purity. Before moving on to the experimental demonstration of entangled photon generation, I want to comment on the significance of the results listed in the previous section.

In Sec. 2.3.1 I presented a theoretical model which describes the entanglement fidelity to a maximally entangled Bell state for the polarization state of the two photons emitted by the biexciton-exciton cascade. Non-ideal behavior is traced back to the dephasing of the exciton during the intermediate step of the cascade, which is mainly caused by the different phase evolution of the bright exciton states due to finite fine structure splitting and by spin scattering events. Poor single-photon purity also decreases the measured fidelity by reducing the number of useful single cascade recombinations.

In the previous section, I reported state-of-the-art figures for both fine structure splitting and radiative lifetime, the two parameters which control the magnitude of the exciton dephasing. As a consequence, the negative effect of the broken degeneracy of the bright exciton states on our droplet epitaxy GaAs quantum dots is kept low on average. The influence of background stray light is reduced as well, thanks to the resonant two-photon excitation scheme.

Additional dephasing comes from hyperfine coupling between the electron and nuclei spins. This has been recognized as a major drawback for In(Ga)As quantum dots, whose fidelity stays at best slightly above 0.8 even at zero fine structure splitting [172]. Recent studies [19, 20] pointed out that GaAs quantum dots are less affected by this effect, because the nuclear spin of Ga (3/2) is much lower than the one of In (9/2), and so the magnitude of the fluctuating magnetic field from the nuclei is reduced. Since this property is mainly dependent on the choice of material, it is an additional advantage for strain-free droplet epitaxy GaAs quantum dots as well. A literature review [184] reports an electron dephasing time from hyperfine coupling of about 15 ns for GaAs, which is considerably longer as compared to the 2 ns reported for InAs and, most importantly, to the exciton radiative lifetime.

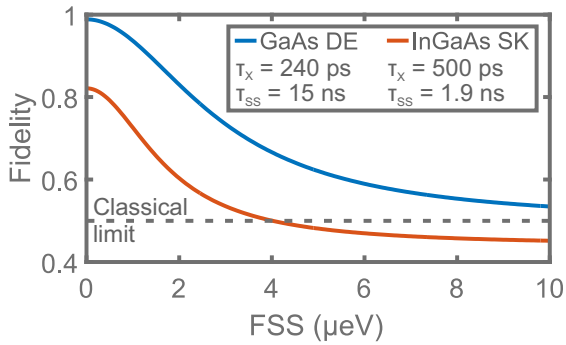

FIGURE 5.20: Entanglement fidelity as a function of fine structure splitting for the GaAs quantum dots described in this thesis and for typical Stranski-Krastanow In(Ga)As quantum dots. The curves have been traced on the basis of an exciton phase evolution model using the parameters reported in the legend.

The impact of the various factors introduced in the discussion on entanglement fidelity can be quantified by means of the Eq. 2.14 deduced in Sec. 2.3.1. Using this formula and representative values of radiative lifetime, exciton dephasing time by hyperfine coupling and background light noise, I evaluated the dependence of entanglement fidelity on fine structure splitting and reported it in Fig. 5.20. A comparison with the prediction for typical In(Ga)As Stranski-Krastanow quantum dots reveals a much broader

access to proper conditions for emitting strongly entangled photon pairs. In particular, when the expected fidelity is computed for the fine structure splitting distribution previously summarized in Fig. 5.15b, almost all the quantum dots emitting near the target wavelength of 780 nm result able to generate pairs of photons with an entanglement fidelity above the classical limit. In particular, even using a conservative estimate of 300 ps for the radiative lifetime, the yield of entanglement-ready emitters is above 95%. This is a notable achievement, since it satisfies the initial goal of providing a simple self-assembly strategy able to improve the reproducibility in the fabrication of entangled photon emitters.

In order to finally demonstrate the generation of entangled photon pairs, I performed cross-correlation measurements in different polarization bases between the X and XX emissions of a suitable quantum dot.

The spectrum of the selected quantum dot was already shown in Fig. 5.16c. It was chosen on the basis of a fine structure splitting of 2.6 ± 0.5 μeV, which is a value representative of a significant fraction of the emitters, and an exciton radiative lifetime of 230 ps under resonant two-photon excitation. According to Eq. 2.14, these values should result in an entanglement fidelity of 0.77, well above the classical limit.

Cross-correlation events were measured in the Hanbury Brown–Twiss setup described in Sec. 4.2.4. Coincidences between the exciton and biexciton lines were counted in three different polarization bases, namely two pairs of orthogonal linear polarizations (H/V and D/A, where D is rotated by 45° with respect to H) in addition to right-(R) and left-(L) handed circular polarization. Figure 5.21a displays all the experimentally acquired data, which exhibit the expected specific bunching and anti-bunching peaks.

The degree of correlation was calculated as in Eq. 4.4 from the coincidence counts between the exciton and biexciton emission, for co-polarized and cross-polarized photons, integrated over the time window of a single pulse with a time bin of 6 ns. The degrees of correlation in the six measured polarization bases enter Eq. 5.2 for the estimation of the fidelity to the expected maximally entangled Bell state [17].

$$f = (1 + C_{HV} + C_{DA} + C_{RL})/4 \tag{5.2}$$

The result is illustrated in Fig. 5.21b. The fidelity of the zero delay pulse

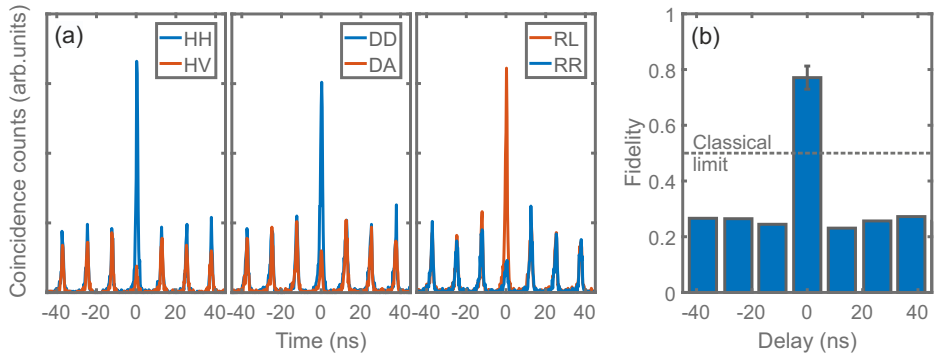

FIGURE 5.21: a) Cross-correlation measurements between the X and XX lines of a quantum dot with low but not zero fine structure splitting, acquired in different polarization bases, namely linear, diagonal and circular. b) Fidelity to the expected maximally entangled state.

is 0.77 ± 0.04, which is significantly above the upper limit for classically correlated states. I estimated the error with Gaussian propagation, assuming a Poissonian distribution of the correlation counts. The experimental figure is in very good agreement with the predictions of the previously discussed exciton phase evolution model for GaAs quantum dots. This result supports our claim that almost any quantum dot in the ensemble is capable of delivering entangled photons with fidelity above the classical limit.

Chapter 6

Sample transfer from GaAs(111)A onto a piezoelectric substrate

In the previous chapter, I illustrated how droplet epitaxy on GaAs(111)A can be used to obtain a near-unity yield of entanglement-ready emitters around the large dispersion region of Rb vapor cells at 780 nm. From the point of view of the design of the quantum dot, such a result is already satisfying basic requirements for the fabrication of a functional device. Nonetheless, in order to achieve an efficient semiconductor entangled-photon emitter capable to operate a hybrid solid state-atomic node for quantum communication, some other elements need to be improved as well.

Matching the hyperfine splitting of the absorption D_2 lines of ^{87}Rb requires an accuracy of few μeV [22, 84, 88] and is therefore beyond the capability of the control over emission energy supplied by shape engineering. Fine tuning of the wavelength of emission requires an external field. Among all the possible solutions, which include electric [185], magnetic [22] and optical fields [186], and possibly even temperature variation [187, 188], using biaxial in-plane strain is a convenient and powerful approach [189, 190]. Indeed, this mechanism to fine tune the optical properties of the emitter can be implemented in a compact, reversible and electrically-controlled

way, by integrating the active region of the sample onto a piezoelectric substrate. Moreover, if an advanced design such as a micro-machined multi-leg device is used, it is possible to apply anisotropic strain and also compensate for non-zero fine structure splitting [30, 31, 73]. This opportunity would offer an additional insight into the entangled photon emitters studied here, allowing to experimentally determine the maximal entanglement fidelity that GaAs droplet epitaxy quantum dots can achieve at precisely zero fine structure splitting.

Another essential improvement towards a solid-state entangled photon source, necessary to outperform spontaneous parametric down-conversion, is to improve the collection efficiency [45, 191]. Several solution are viable, among them disk [192] and micropillar [193] optical resonators, photonic-crystal cavities or waveguides [32], and nanowires [114]. Arguably the most successful approach in this direction is embedding the active region of the quantum dot inside a microcavity made of distributed Bragg reflectors [58, 194], which also has the advantages of reducing the exciton recombination time through Purcell effect and of being compatible with fabrication in a standard III-V MBE system. The use of AlAs/GaAs multilayers, the standard choice for In(Ga)As quantum dots, can be extended to GaAs nanostructures provided that a small fraction of Al is added to the GaAs layers to prevent absorption in the spectral window of emission of the quantum dots.

In this chapter, I will present some preliminary steps headed in this direction. In particular, I am going to focus once again on the problems related to the materials science involved. Even if the integration on a piezoelectric substrate and the fabrication of an optical cavity do not require any redesign of the quantum dots with respect to the procedure developed in the previous chapter, increasing the complexity of the structure of the sample on a (111)A substrate—a less investigated system as compared to the case of (100) orientation—poses additional challenges.

6.1 Fabrication of an AlGaAs sacrificial layer

In this section, I will discuss how to modify the structure of the sample with the aim to transfer its active region onto a monolithic single piezoelectric

crystal. In order for the strain to be effectively transferred onto the semiconductor layer only a thin membrane must be placed on the new substrate. This operation can be performed by means of standard semiconductor processing techniques.

I decided to opt for the device design proposed in Ref. [195]. A PMN-PT substrate is chosen because of its giant piezoelectric response. Only the part of the as-grown sample composed of the AlGaAs barrier and the quantum dots is transferred on top of it. A thin gold layer is introduced in between, so that, by appropriately choosing the thickness of the AlGaAs barrier and the vertical position of the quantum dots, a basic metal-semiconductor-air cavity is obtained. In particular, the thickness of the total semiconductor membrane must be 5/3 of the cavity mode wavelength—that is the wavelength at which extraction efficiency has to be maximized, divided by the refractive index of the material—and the location of the quantum dots layer must be one cavity mode wavelength away from the semiconductor-air interface, so to satisfy a standing wave condition [113]. Despite the basic design and the low internal reflectivity of the top interface, far from the onset of Purcell enhancement, it is possible to achieve an up to 15-fold increase in light extraction efficiency [195, 196].

This processing routine requires the removal of the GaAs substrate. This step can be conveniently and precisely performed by means of chemical back-etching, as it will be described in more detail in Sec. 6.2, together with the rest of the procedure for sample microfabrication. Considering the small thickness of the membrane—few hundreds of nanometers—and, consequently, the accuracy required on the portion of material to remove, the etching has to be as selective as possible. An established solution relies on introducing, during the deposition of the sample, a sacrificial layer in its structure, just below the active region. It consists of a layer 50–100 nm thick, made of AlAs or AlGaAs with a very high Al content, above 80%. In this way, no strain is introduced thanks to the very small lattice mismatch, while the large difference in composition provides a solid ground for finding etchants with vastly different reaction rates for GaAs and the sacrificial layer respectively [197].

The resulting sample structure is summarized in Fig. 6.1a. In the following part of the section, I will describe the challenges related with the growth of a defect-free AlGaAs sacrificial layer and discuss how to minimize its

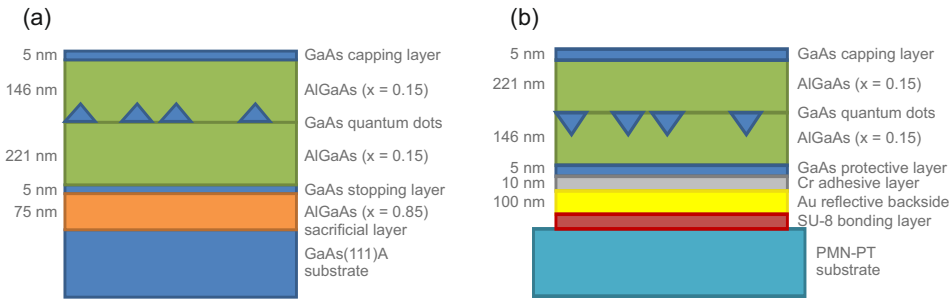

FIGURE 6.1: a) Structure of a sample with sacrificial layer and barrier thickness adjusted for a metal-semiconductor-air cavity. b) Structure of the processed sample after transfer of the active semiconductor membrane on a piezoelectric substrate.

impact on the optical quality of the sample.

6.1.1 High Al content AlGaAs on a (111)A substrate

In Ch. 5, I presented some substantial advantages of working on a (111)A oriented surface over a standard (100) for the fabrication of entangled photon emitters, above all high in-plane symmetry and crystallization of the droplets at elevated temperature. Despite the interest of (111) substrates, which extends to other fields of application such as high mobility transistors [198] and quantum well intersubband photodetectors [199], optimal conditions for epitaxial growth have been investigated to a lesser extent. This is especially true when it comes to surface morphology, as it was proved challenging to deposit material with low interfacial roughness [200, 201]. Indeed, the results presented up to now rely on recent developments towards the formation of AlGaAs layers with an atomically flat surface [139], as already mentioned in Sec. 5.1.2.

As we moved on to reproduce similar results for the deposition of the sacrificial layer, additional complications arising from the higher Al content in the barrier were revealed. A first attempt was made by extending the procedure developed for the compositional range equal to or below 30% Al content. Therefore, a 70 nm layer of AlGaAs with 85% Al fraction was

deposited at a substrate temperature of 520°C with a total group III flux of 0.1 ML/s and a beam equivalent pressure of As of 3×10^{-5} torr.

Measurements of surface morphology were performed by means of atomic force microscopy and showed a large discrepancy with respect to the expected behavior. In Fig. 6.2 I report the comparison between large-area atomic force microscopy scans of two AlGaAs layers, with 30 and 85% Al content respectively, fabricated using the growth parameters cited above. In the first case, some triangular pyramids whose height does not exceed 4 nm are observed, and they are separated by areas with atomically flat terraces. The triangular formations all have the same orientation, which indicates the presence of a single domain crystal. Conversely, in the second case, the surface is fully covered by large hillocks tens of nm tall, that often intersect along anti-phase domain boundaries. The poor crystalline quality was also confirmed by reflection high-energy electron diffraction analysis during growth, the diffraction pattern showed an intense signature of crystal twinning.

In order to overcome this hurdle, a methodical study of surface morphology on few series of samples has been carried out. We examined some viable strategies to improve the crystalline quality of the material. In particular, we investigated the impact of substrate temperature and As flux, in the range between 520 and 620°C and between 9×10^{-6} and 5×10^{-5} torr respectively; the introduction of a buffer layer between the GaAs substrate and the sacrificial layer, consisting of a high crystalline quality AlGaAs layer with 30% Al content; the effect of lowering the Al fraction of the sacrificial layer down to 55%, the minimum tolerable so to maintain enough etching selectivity for the processing of the sample.

Without entering a case-by-case scrutiny of the performed tests, I will just summarize the main conclusions. Increasing the substrate temperature succeeds in substantially reducing the surface roughness. The more clear-cut improvement is obtained by combining the deposition of the sacrificial layer at 620°C with the insertion of a buffer layer with 30% Al fraction. In that case, surface roughness is comparable with what achieved at lower Al concentration, with the ubiquitous presence of atomically flat areas, as shown in Fig. 6.2c and 6.2d. Despite these steps forward, anti-phase domain boundaries are still unavoidable, and in every sample the reflection high-energy electron diffraction pattern retains typical features related to twin

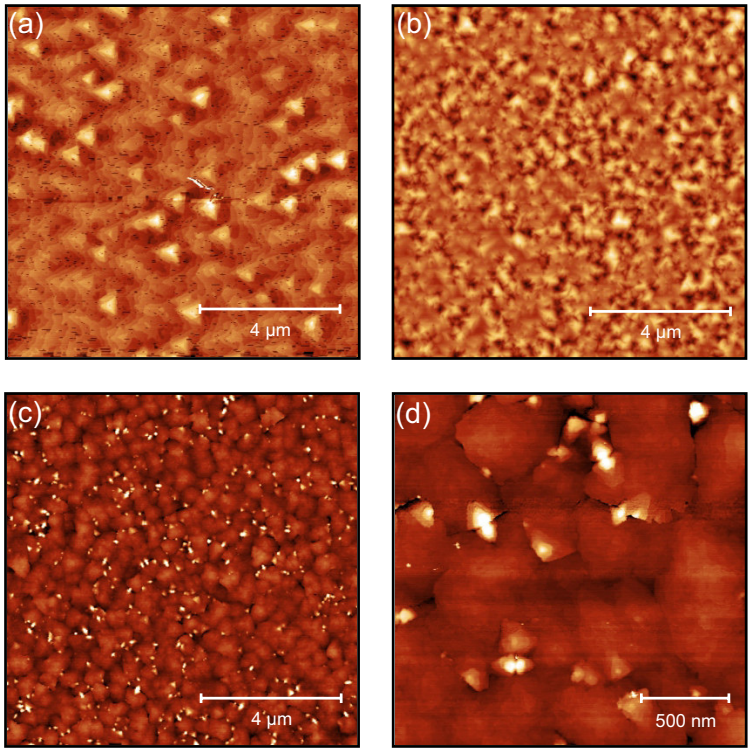

FIGURE 6.2: Atomic force microscopy images on a 10 x 10 μm^2 area performed on top of an AlGaAs layer grown by molecular beam epitaxy. a) 30% Al content, height scale 0–5 nm. b) 85% Al content deposited at 520°C, height scale 0–200 nm. c) 85% Al content deposited at 620°C on top of a 30% Al AlGaAs buffer layer, height scale 0–11 nm. d) Same as panel (c), close-up view on a 2 x 2 μm^2 area, height scale 0–13 nm.

defects. Even reducing the Al content in the sacrificial layer does not bring to any improvement, indicating a lower compositional threshold for the onset of stacking faults. Further exploration of the growth parameter space is constrained by setup limitations on the upper substrate temperature.

Given the difficulty of completely removing crystal defects in the sacrificial layer, I decided to focus on quantifying their detrimental effect on the

optical properties of the quantum dots by means of ensemble and micro-photoluminescence. Two complete samples were fabricated according to the sample structure depicted in Fig. 6.1a. The procedure used for the growth of the quantum dots was the same one of the high-quality sample studied in Sec. 5.2. The two samples differ in regard to how the sacrificial layer is fabricated. Both are made of AlGaAs with 85% Al content. In one case, the deposition takes place in conditions similar to the ones used for the barrier, that means 70 nm of AlGaAs deposited at a substrate temperature of 520°C, with a group III total flux of 0.1 ML/s and a beam equivalent pressure of As of 3×10^{-5} torr. In the other case, the best conditions for the formation of a flat surface are used: first, a thin buffer layer made of 12 monolayers of AlGaAs with 30% Al fraction is grown at 520°C, then the substrate temperature is temporarily increased to 580°C for 20 sec, while the ratio of group III fluxes is modified to deposit AlGaAs with Al content raised to 85%, and finally brought to 620°C for the growth of 70 nm of material with the same composition.

The morphology analysis by atomic force microscopy of the samples after capping already reveals that, even when starting from a flat sacrificial layer, the presence of defects propagates into the active region and results in a degraded upper interface. Fig. 6.3 compares micrometer-sized area scans from the two samples and, even if in the second case few flat areas (up to 500 nm in diameter) can be noticed, both display large terraces up to 50 nm in height.

Ensemble photoluminescence spectra suggest a decrease in radiative efficiency. As usual, the excitation laser power used for the measurement was set low enough not to have an impact on the spectral shape, and the same power was used for all the samples compared. Fig. 6.4a shows an almost 10-fold decrease in luminescence intensity from the sample with the sacrificial layer deposited at 520°C with respect to the one without. The sample for which the optimized deposition procedure of high Al content AlGaAs at higher temperature was used performs slightly better, but its radiative efficiency is still five times lower as compared to the defect-free benchmark. In addition to that, no radiative recombination from AlGaAs direct bandgap is observed at any excitation power, a possible hint of an elevated concentration of non-radiative recombination centers in the barrier material.

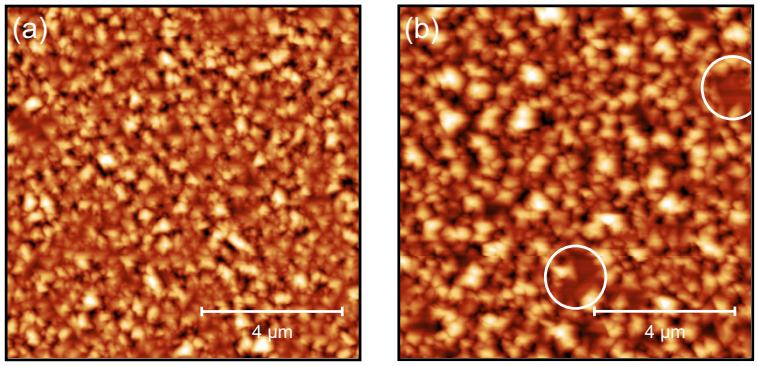

FIGURE 6.3: Atomic force microscopy images on a 10 x 10 μm^2 area performed on top of a capped quantum dot sample with a high Al content sacrificial layer. a) Sacrificial AlGaAs deposited at 520°C, height scale 0–160 nm. b) Sacrificial AlGaAs deposited at 620°C on top of a 30% Al AlGaAs buffer layer, height scale 0–180 nm. A couple of flat areas are highlighted.

Fig. 6.4b concentrates on the comparison of the energy distribution of the emitters. The introduction of the sacrificial layer causes a stark broadening of the emission range, and the features linked to monolayer fluctuations in height cannot be identified anymore. I attribute this behavior to an increased disorder in the sizes and shapes of the quantum dots, a direct consequence of the sizable surface roughness.

Single quantum dot spectroscopy confirms that the presence of defects has a strong negative effect on the optical properties of the emitters. Spectral wandering of exciton lines is increased dramatically on both the samples with the sacrificial layer. The average exciton linewidth is well above 200 μeV and it makes even difficult to correctly identify the peaks from radiative recombination of different excitonic complexes. Few narrower lines can be found, still their linewidth hardly goes below 100 μeV. Also from the point of view of fine structure splitting the performances are degraded with respect to the case with no sacrificial layer. A very broad distribution of values is observed on both samples, centered around 20 μeV. Some quantum dots present large fine structure splitting and a strong dependence of the photoluminescence intensity on linear polarization (see Fig. 6.5). This is

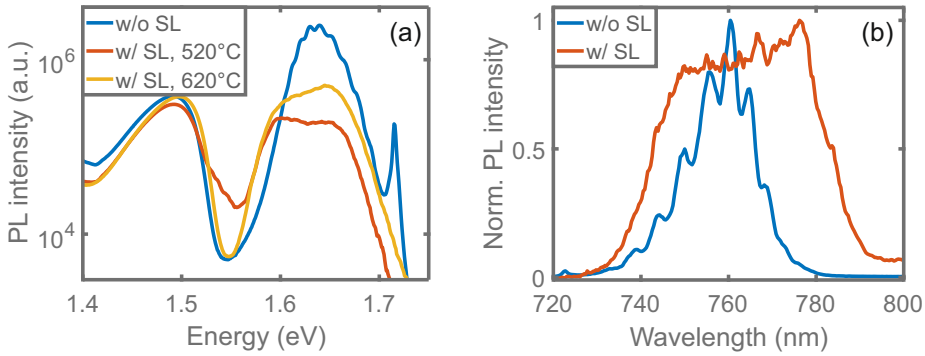

FIGURE 6.4: Comparison among the low temperature ensemble spectra of a sample grown with no sacrificial layer (SL) (blue line), with a sacrificial AlGaAs layer (85% Al) deposited at 520°C (red line) and with a sacrificial AlGaAs layer (85% Al) layer deposited at 620°C on top of a 30% Al AlGaAs buffer layer (yellow line). a) Energy on the x axis, logarithmic vertical scale, entire emission range. b) Wavelength on the x axis, linear vertical scale, quantum dots emission range.

usually a signature of relevant shape anisotropies, which is consistent with what already suggested by measurements on the ensemble. On a few lines it was also noticed sizable jittering on the second timescale.

In summary, the formation of extended defects during the deposition of a high Al content sacrificial layer causes a raise in surface roughness, increasing the disorder in the shape of the quantum dots, and creates a high concentration of charge traps which negatively affects the spectral stability of the emitters.

These serious issues could not be solved despite a series of attempts at growth optimization, hence a different strategy is needed in order to make the fabrication of high quality quantum dots compatible with some common semiconductor processing routines.

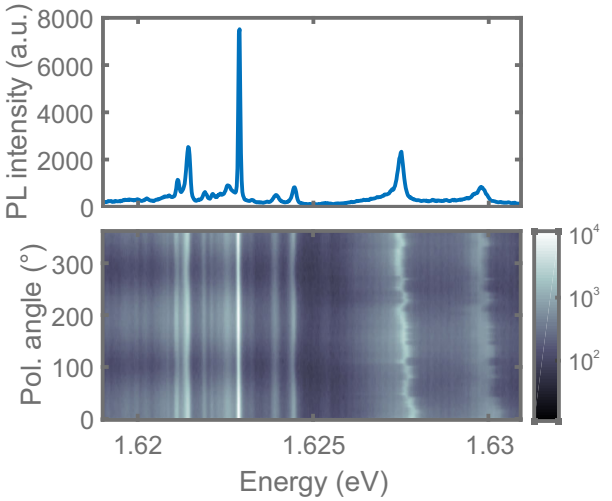

FIGURE 6.5: Polarization-resolved photoluminescence map from the sample grown with a sacrificial AlGaAs layer (85% Al) deposited at 520°C. The emission from a couple of quantum dots is captured, to show large fine structure splitting—35 μeV, on the left—and strong spectral wandering and jittering—on the right.

6.1.2 High Al content AlGaAs on a 2° miscut (111)A substrate

A common approach to avoid issues related to the presence of anti-phase domains in epitaxially grown GaAs, widely studied on Ge and Si substrates in particular, is to use a tilted substrate with respect to the low index surface [202–204]. Even a small miscut angle of few degrees can drastically affect the growth kinetics by promoting incorporation through a step-flow mechanism [205]. Despite the fact that the AlGaAs/GaAs(111)A materials system has been less frequently studied, the use of miscut substrates has already been suggested as an effective, if not crucial, expedient to improve crystal quality and surface roughness for the fabrication of multiple quantum wells [33].

Here I present the advantages of employing a GaAs(111)A substrate miscut by an angle of 2° towards the ⟨-1-12⟩ direction. The choice of a moderate tilting results from a trade-off between promoting the step-flow growth mode and keeping the distance between consecutive terrace steps

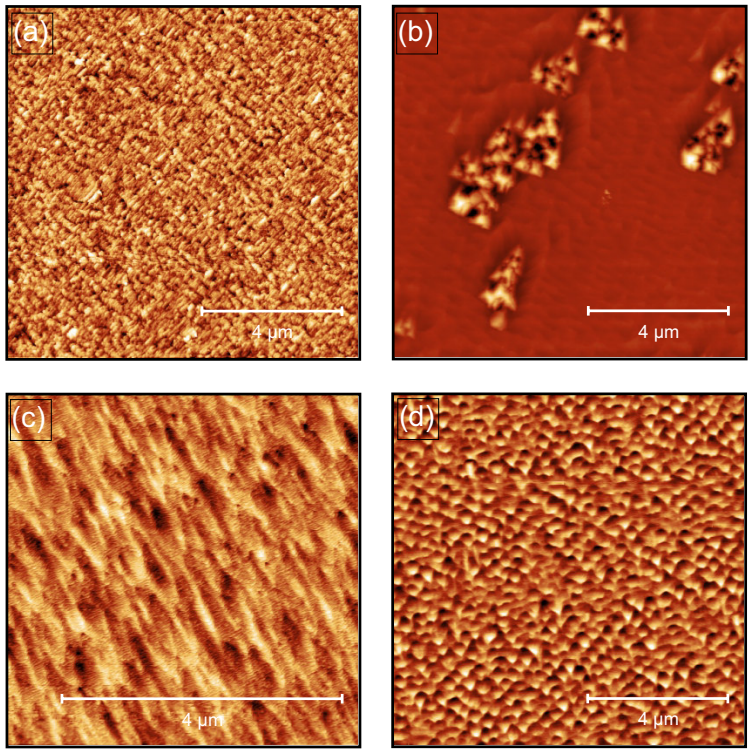

FIGURE 6.6: Atomic force microscopy images on a 10 x 10 μm^2 area performed on top of samples grown on a 2° miscut GaAs(111)A substrate. a) 85% Al content AlGaAs layer, 0.1 ML/s growth rate, height scale 0–6 nm. b) Capped quantum dot sample with sacrificial layer as in panel (a), 0.085 ML/s barrier growth rate, height scale 0–150 nm. c) close-up view on a 5 x 5 μm^2, 85% Al content AlGaAs layer, 0.35 ML/s growth rate, height scale 0–4 nm. d) Capped quantum dot sample with sacrificial layer as in panel (c), 0.58 ML/s barrier growth rate, height scale 0–10 nm.

above the lateral dimensions of a typical quantum dot.

In order to have a direct comparison with the previous attempts on a low index substrate, a high Al content AlGaAs sacrificial layer was deposited using the same growth parameters as obtained by our optimization of

surface roughness. In detail, 70 nm of AlGaAs with 85% Al content were deposited at a substrate temperature of 620°C with a group III total flux of 0.1 ML/s and a beam equivalent pressure of As of 3×10^{-5} torr, on top of a thin buffer layer of AlGaAs with 30% Al fraction. The surface morphology, probed by atomic force microscopy, is characterized by very low roughness. Moreover, this value is low enough that we can recognize terrace steps related to the tilting of the crystal planes, which are clearly visible in Fig. 6.6a. In situ reflection high-energy electron diffraction monitoring showed much weaker features from crystal twinning, also supporting increased crystalline quality. Consistently, we observed a substantial improvement when the active region with quantum dots was deposited on top of the sacrificial layer, according to the sample structure shown in Fig. 6.1a. Figure 6.6b highlights the presence of large flat areas with occasional pyramidal formations, which, on the contrary, dominated the surface morphology in the case of Fig. 6.3b.

The introduction of a small miscut is enough to trigger the transition to a step-flow regime, which results to be the most effective way to extend our growth protocol to the whole range of AlGaAs composition. However, an optimization of the growth procedure is still required to fully suppress extended defects. Despite their low spatial density, they act as nucleation sites for the creation of undesired domes, when increasing the thickness of deposited material.

Conveniently enough, the choice of a miscut substrate also gives wider access to an additional parameter, namely the deposition rate of the group III material, which ultimately determines the growth rate. Indeed, the presence of surface ledges promotes the incorporation of As, which is a slow process on the (Al)GaAs(111)A surface due to the unstable three dangling bonds configuration of As adatoms and forces the use of a high ratio of V to III beam equivalent pressure to achieve good flatness.

Figure 6.6c shows the surface of an 85% Al layer of AlGaAs, which has been deposited using the same parameters of the latest attempt, except for the group III total flux which has been increased to 0.35 ML/s. The surface roughness is mainly limited by steps induced by the tilting of crystal planes and this time no signature from crystal twinning is revealed by reflection high-energy electron diffraction analysis. The Ga/Al flux is increased also during the deposition of the active layer of the sample. The barrier material, AlGaAs with 15% Al content, is fabricated using a group III total flux of 0.58

ML/s as compared to 0.085 ML/s. Ultimately, we obtained a quantum dot sample ready for processing which possesses an excellent flatness straight up to the semiconductor-air interface, as proved in Fig. 6.6d.

The ability to significantly increase the growth rate is an important achievement in the direction of enhancing the light collection efficiency as well. The fabrication of microcavities requires the addition of thick distributed Bragg mirrors to the sample structure. If we stick to the optimized protocol previously developed for (111)A orientation, this would be a time-consuming process, in fact posing a practical limitation on the realization of a highly performing optical cavity.

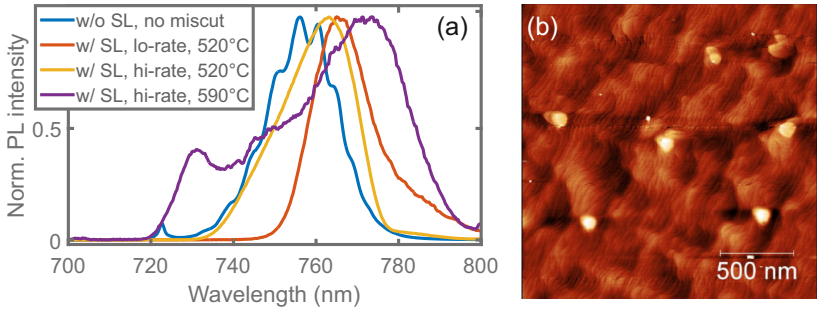

FIGURE 6.7: a) Comparison among the low temperature ensemble spectra of quantum dots from samples grown on a 2° miscut substrate. The barrier layer is deposited either at 520°C, group III flux 0.085 ML/s (red line), at 520°C, group III flux 0.58 ML/s (yellow line), or at 590°C, group III flux 0.58 ML/s (purple line). The corresponding sample with no sacrificial layer on a flat (111)A substrate is also included as a reference (blue line). b) Atomic force microscopy image on a 2 x 2 μm^2 area of quantum dots grown on a 2° miscut AlGaAs(111)A surface, height scale 0–11 nm.

I performed photoluminescence experiments on these samples in order to assess the impact of the introduction of a miscut substrate on the optical properties of the quantum dots. Ensemble photoluminescence spectra, shown in Fig. 6.7a, have features similar to the ones of the samples studied in the previous section. With respect to the case with no sacrificial layer, the distribution of emission energies is once again broadened, and there

TABLE 6.1: Average linewidth (FWHM) and fine structure splitting (FSS) values (best value in brackets), evaluated on emission lines unambiguously identified as neutral excitons, are reported for a list of samples grown on 2° miscut substrates and differing for substrate temperature (T_{sub}) and group III flux during the deposition of the barrier layer.

III flux(ML/s)	T_{sub}(°C)	FWHM(μeV)	FSS(μeV)	λ_{em}(nm)
0.085	520	130	35 (10)	750–800
0.58	520	170	16 (3)	740–780
0.58	590	120	12 (2)	725–800

are no modulations from height fluctuations of a single monolayer. This behavior has been interpreted as a consequence of the increased disorder in the size and the shape of the nanocrystals. Despite the improvements in the surface roughness, the distance between terrace steps is less than the base diameter of a typical quantum dot (see Fig. 6.7b). The interaction with atomic steps affects the geometry of the nanostructures, introducing random variations in shape and increasing their average aspect ratio, which results in a redshift of the centroid of the ensemble photoluminescence peak. A side outcome is a higher spatial density of emitters near 780 nm.

A deeper insight is offered by the single quantum dot spectroscopy data. The typical spectrum under above barrier excitation (not shown here) resembles the ones from Sec. 5.2, in terms of exciton brightness at saturation and excitonic complexes present. The spatial density of emitters within a range of few nm from 780 nm is increased with respect to that case, without hindering the possibility to optically address each dot singularly. As expected from the structural characterization done with atomic force microscopy and reflection high-energy electron diffraction, spectral wandering is dramatically reduced with respect to the samples grown on top of a sacrificial layer on a flat (111)A substrate, which is evidence of progress in crystalline quality. The average linewidth data are reported in Table 6.1, and, given the quite large standard deviation of 50–60 μeV, a non-negligible fraction of emitters close or below the resolution of the spectrometer (40 μeV) are observed. Despite that, spectral diffusion is still much larger as compared to what achieved in absence of any sacrificial layer.

A possible explanation is that the change in growth mode could have

introduced non-trivial consequences on crystal quality. Hence, in order to reproduce extremely narrow lines, we modified the deposition protocol of the barrier layer by raising the substrate temperature up to 590°C. While the higher temperature further reduces the sticking coefficient of As, this is feasible in the step-flow regime, since, on the other hand, the probability of As incorporation is increased at step edges. Nonetheless, this approach does not succeed in significantly reducing the neutral exciton linewidth (row 3 in Table 6.1).

This result offers an interesting insight into the complex problem of identifying and inhibiting sources of spectral wandering. While the temperature of crystallization of the material is surely a crucial parameter to obtain a high quality material, it is not the only factor coming into play. Indeed, given a fixed recipe for the preparation of the quantum dots, despite the higher temperatures employed during growth on a slightly miscut substrate, we were not able to even match the low level of spectral diffusion achieved on the low index surface. Arguably, the nature of the defects related to a specific growth mode ultimately dictates the magnitude of the excitonic linewidth, since their charge distribution, characteristic lifetime and spatial spread determine the fluctuating electric fields acting on the charges confined in a quantum dot.

Also the fine structure splitting is affected by the choice of a miscut substrate. This is consistent with the previous discussion on the interaction between terrace steps and quantum dots, which tends to randomly influence their morphology. However, in optimal conditions, this effect is less relevant as compared to the elevated roughness observed on a quantum dot sample with sacrificial layer on a flat (111)A substrate. On the sample where the barrier was deposited at 590°C the average fine structure splitting in the spectral region near 780 nm is 8 μeV. This value is close to doubled as compared to our best one, but it is still low enough to found a fraction of entanglement-ready emitters.

I demonstrated that using miscut substrates is a viable strategy to grow a high Al content AlGaAs layer on a substrate with (111)A orientation and drew the attention to the wider range of exploitable substrate temperatures and growth rates offered by the step-flow mode. While some quantum dots with good optical properties can be selected to perform single dot spectroscopy experiments, further investigation will be needed in order to

achieve results equivalent to the ones presented in Ch. 5.

6.2 Sample processing

In this section, I will describe in detail a reproducible procedure to transfer a semiconductor membrane onto a piezoelectric actuator. An outline of the chosen approach was already drawn in the introduction of the chapter, where I listed the requirements on the structure of the as-grown sample and illustrated the final target device, both pictured in Fig. 6.1.

The whole processing can be divided in three main phases, that are surface preparation, bonding with the piezoelectric crystal and removal of the semiconductor substrate.

The new substrate is obtained from a monolithic piezoelectric PMN-PT crystal. It can be cut to accommodate the lateral extension of the sample and it is mechanically polished down to 300 μm. In order to be able to apply a uniform electric field across the material, both sides have to be metalized, hence a coverage of 100 nm of Au, together with an adhesion layer made of 10 nm of Cr, is deposited in a metal evaporation chamber. The same metalization procedure is performed on the top surface of the sample (the epitaxially grown interface). In this way, on both the sides to bond there is a gold layer, which is also planned to act as reflective backside for the semiconductor cavity including the quantum dots.

The following step is carried out with a technique denoted as adhesive wafer bonding. SU-8 2000.5 photoresist is a convenient bonding agent provided with good mechanical, chemical and thermal stability. The photoresist is evenly distributed on the surface of the sample by spin-coating and then undergoes soft-baking. Afterward, the sample and the piezoelectric crystal are brought together using a flip chip bonder in order to achieve good control on the flatness of the adhesion layer. The bonding is hardened applying mechanical pressure (20 N) and heating at 250°C for 15 min.

Finally, the semiconductor substrate and the sacrificial layer have to be removed, leaving only a thin semiconductor membrane consisting of the barrier layer and the embedded quantum dots. This operation is performed through three steps of chemical back-etching. The first two completely remove GaAs (substrate and epitaxially-grown buffer) from the bottom of the sample, whereas the third one deals with the sacrificial layer.

After having protected the sides and its bonded interface with a soft-baked S1818 photoresist, the sample is placed into a solution based on phosphoric acid—H_3PO_4/H_20_2 3:7. This combination acts isotropically and has a fast etching rate, but it has poor compositional selectivity between GaAs and AlGaAs [197]. Therefore, it is used to accelerate the dissolution of the bulk of the thick GaAs substrate, and the reaction is stopped before it reaches the sacrificial layer. The etching rate on a GaAs (100) substrate should be around 3 μm/min, I tested it on a 2° miscut (111)A substrate and it is approximately doubled. In 40 min the GaAs layer is considerably thinned down, ready for the next step.

The remaining part is etched away with a solution of citric acid, water and hydrogen peroxide—citric acid/H_20/H_20_2 2:2:1. This time, the etching rate is much lower (ideally 3–5 Å/s), but the selectivity between GaAs and AlGaAs is higher and the sacrificial layer will effectively act as a stopping layer. The complete removal of GaAs is quite time-consuming and requires approximately 6–8 hours.

The sacrificial layer must be dissolved using an etchant with opposite compositional selectivity, hydrofluoric acid being the most common choice [197]. Total removal of 70 nm of AlGaAs with 85% Al content requires about 1 min in a HF 40% solution. A 5 nm thick GaAs layer is present to stop the reaction before reaching the AlGaAs barrier and acts as a capping to prevent oxidation.

I successfully applied this procedure on the best performing sample with sacrificial layer presented in Sec. 6.1.2. Specifically, the sample was grown on a 2° miscut (111)A substrate and the barrier was deposited at a temperature of 590°C, with a beam equivalent pressure of As of 3×10^{-5} torr and a group III flux of 0.58 ML/s. Finally, the processed sample is mounted on a chip carrier and the metalized sides of the piezoelectric crystal are contacted with gold pads using a wire bonder. A fully processed sample is pictured in Fig. 6.8. The semiconductor membrane shows excellent flatness over a large area of a few mm^2.

It is important to verify if the optical properties of the quantum dots are not negatively affected by the processing, so I investigated this sample too by means of micro-photoluminescence. The main results are summarized in Table 6.2 and clearly demonstrate that the emission features are practically

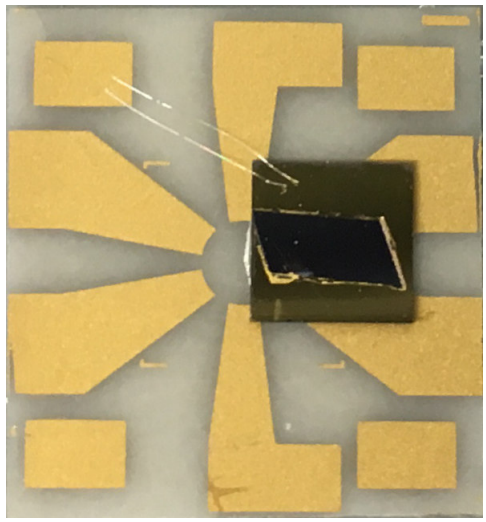

FIGURE 6.8: Picture of a semiconductor membrane containing quantum dots transferred on a piezoelectric substrate mounted on a chip carrier.

unaltered, as desired. No additional contribution to spectral diffusion is introduced, neither the fine structure splitting is increased. The latter outcome is actually non-trivial. Indeed, the bonding procedure can insert unwanted anisotropic strain in the system, related to thermal budget in a photoresist layer with poorly controlled uniformity affecting the thin semiconductor membrane. This random strain field could affect the electronic structure of the quantum dots and enlarge the energy separation between the bright exciton states. Even the spectral range of emission of the quantum dots is unaffected. For these reasons, the microfabrication method presented here is compatible with the requirements for the production of entangled photon emitters.

Table 6.2 also reports a comparison between the brightness of exciton emission. I did observe an enhancement, more than 3-fold, but it is much lower than what expected from the metal-semiconductor-air cavity. However, this was due to a poor optimization of the structural design of the sample. Reflectivity measurements, reported in Fig. 6.9, show a reflection dip which falls at 810 nm at low temperature. This marks the cavity mode

TABLE 6.2: Average linewidth (FWHM), fine structure splitting (FSS) and photoluminescence (PL) intensity values, evaluated on emission lines unambiguously identified as neutral excitons in a spectral region 10 nm wide around 780 nm, are reported for the same sample grown on a 2° miscut (111)A substrate before and after transfer on a piezoelectric crystal.

Sample	FWHM(μeV)	FSS(μeV)	PL int.(cps)	λ_{em}(nm)
as-grown	120	8	1100	725–800
processed	110	7	3500	725–800

wavelength where the light extraction efficiency is maximized, and it is shifted by 30 nm with respect to the target wavelength, that is 780 nm.

I simulated the expected reflectivity spectrum solving the Fresnel equations with the transfer matrix method. I included the entire nominal structure of the sample, from the gold layer above, as reported in Fig. 6.1b, and employed refractive indexes from the literature [206–208] (data relative to AlGaAs with 10% Al content were used for the barrier, being the closest match to the actual composition). The result is also shown in Fig. 6.9 and reproduces the redshift of the cavity mode observed in the experiment. The discrepancy between data and calculation can be explained as resulting from deviations of either the actual thickness or the refractive index of the barrier from the nominal values. An optical cavity effect is present, but more accurate design, backed by simple thin film interference calculations, will be needed in order to achieve the desired brightness enhancement in experiment.

In summary, I have presented a viable approach to integrate GaAs quantum dots epitaxially grown on a (111)A substrate onto a piezoelectric crystal for external strain tuning. The processing of the sample is based on standard microfabrication techniques, such as adhesive wafer bonding and wet etching. Selective back-etching requires the preparation of a high Al content sacrificial layer, which proved to be a challenging task on a (111)A surface. Among a few tested strategies, growth on a substrate with a 2° miscut resulted to be the most effective. The tilting with respect to the low index surface promotes growth in step-flow mode, which also allows for a higher deposition rate. This is a relevant improvement for the

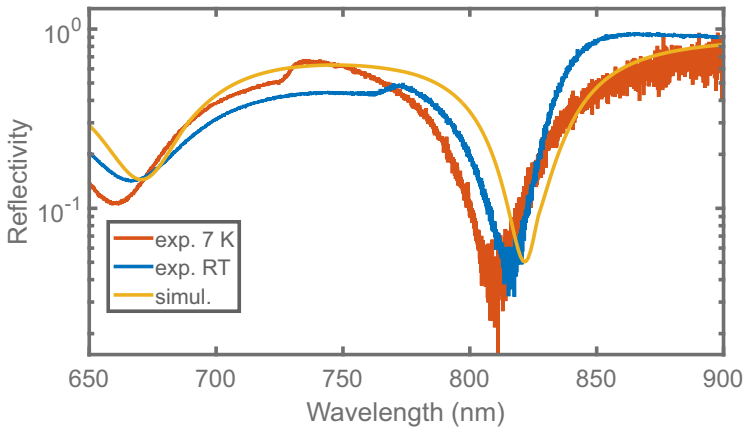

FIGURE 6.9: Reflectivity spectra acquired at cryogenic (7 K, red curve) and room (300 K, blue curve) temperature, together with a simulated spectrum (yellow curve) based on the nominal structure and on material properties at room temperature taken from literature.

fabrication of thick optical microcavities based on distributed Bragg mirrors, an important step forward in the direction of maximizing light extraction. After the processing of a quantum dot sample on the piezoelectric crystal, it is still possible to find a good fraction of entangled photon emitters, but further optimization of the growth protocol will be necessary in order to reduce spectral wandering.

Chapter 7

Conclusions and outlook

In this thesis I investigated the potentiality of GaAs quantum dots grown by droplet epitaxy on (111)A-oriented substrates as an ideal materials platform for the realization of entangled photon sources for quantum networking.

A major part of the research work presented here has been devoted to introduce and study an original approach to this fabrication method. In contrast to standard droplet epitaxy on the (100) surface, which is restricted to substrate temperatures below 250°C and intense As fluxes, quantum dot formation has been observed up to 520°C. A plausible explanation attributes this achievement to the specific choice of the substrate orientation, characterized by a very low As sticking coefficient, which favors As incorporation inside the droplet rather than with Ga adatoms on the surface.

Ensemble photoluminescence was used to characterize the wavelength distribution of the emitters. I have compared these data with energy level simulations based on the geometrical features probed by atomic force microscopy on uncapped samples. The comparison suggests that the increase in growth temperature strongly reduces the impact of interdiffusion at the interface of the quantum dots. This allowed for the reproducible design of the emission wavelength, as it was also shown how the aspect ratio of the quantum dots can be controlled through the growth dynamics. In particular, I have been able to demonstrate operation in the 780 nm range, a condition to frequency-match Rb-based optical quantum memories and so an important target for the realization of quantum repeaters.

The role of the growth parameters has also been studied in relation to single dot photoluminescence. I have confirmed that the higher temperature of crystallization of the quantum dots and the surrounding barrier brings an improvement to the crystalline quality, evaluated in terms of the magnitude of electric fields from charged defects affecting the neutral exciton linewidth. In particular, spectral wandering in optimal conditions has been reduced down to 9 μeV.

Likewise, excellent figures of merit for entangled photon generation have been achieved. Quantum dots emitting at the wavelength of interest displayed a truncated pyramid shape with regular hexagonal base, fulfilling the requirements on high in-plane symmetry for vanishing fine structure splitting. The capping process did not heavily affect the shape of the quantum dots and, therefore, a very low average fine structure splitting of 4.5 μeV has been achieved. Such a value is comparable with a natural linewidth of about 3 μeV, corresponding to the short exciton lifetime below 240 ps unveiled by time-resolved measurements under resonant excitation. Given these state-of-the-art figures of merit, a remarkably high fraction—95%—of the emitters is expected to generate photon pairs with entanglement fidelity above the classical limit. This result meets the original goal set by the research project, namely to develop a simple strategy based on self-assembly for improving the reproducibility in the fabrication of entanglement-ready emitters.

I also experimentally demonstrated entangled photon generation with the help of a resonant two-photon excitation scheme, employed for the first time on droplet epitaxy quantum dots. Cross-correlation measurements have been performed on a representative dot and yielded a fidelity value of 0.77, a value well above the classical limit. Furthermore, this result is consistent with the exciton phase evolution model for GaAs quantum dots, predicting reduced dephasing by hyperfine coupling with respect to InAs-based systems. Further investigation will be needed to test the predictions of the model in presence of totally degenerate bright exciton levels and verify the maximum degree of entanglement achievable with this choice of materials.

This thesis has also explored the possibility of integrating these nanostructures on a piezoelectric substrate in order to precisely control the emission wavelength and the fine structure splitting by strain tuning. I was

able to successfully transfer a semiconductor membrane containing GaAs (111)A quantum dots by means of chemical back-etching and adhesive wafer bonding. The introduction of a 2° miscut angle to the orientation of the substrate has been employed to deposit a sacrificial layer made out of defect-free AlGaAs with high Al content, with moderate impact on the optical properties of the quantum dots. The transition to a step flow regime also offered the possibility to increase the deposition rate, a useful progress towards the fabrication of thick distributed Bragg reflectors for enhancing light extraction.

These results set a feasible route towards external fine tuning of the electronic structure and efficient light collection. Additional efforts will be required in these research directions in order to fulfill the complete set of requirements for a practical solid-state polarization-entangled photon source. Succeeding to do so will open several possibilities for quantum optics experiments involving the slow-down of entangled photons in Rb vapor cells. Under this perspective, droplet epitaxy quantum dots deserve consideration as a candidate technology for the realization of hybrid atomic-semiconductor quantum interconnects, a proof-of-concept milestone for quantum networking.

Appendix A

Simulation of electron and heavy-hole states in a quantum molecule

In order to test the effective-mass constant-potential and single-band model—introduced in Sec. 3.1.1 and implemented in Sec. 5.1.1—on a complex realistic morphology, I briefly discuss here its use for the design of non-trivial droplet epitaxy GaAs/AlGaAs nanostructures, namely asymmetric quantum molecules.

The research interest behind these objects lies in the possibility to generate radiation in the terahertz spectral region by excitation with an optical femtosecond pulse [209]. The physical mechanism relies on bound-bound transitions in a three-level Λ-type system in which the two lowest-lying levels are localized in different spatial regions, and their energy separation matches the frequency range of the terahertz gap, namely where practical technologies for generating and detecting the radiation are not established yet. This phenomenon was observed in semiconductor quantum wells, where the separate localization of the carriers was achieved through an applied electric field either in coupled quantum wells [210] or making use of the different effective mass of the light and heavy holes [211].

In three-dimensional nanostructures a three-level Λ-type system which

satisfies the previously listed requirements can be devised by finely controlling the morphology. Droplet epitaxy allows to fabricate quantum molecules composed of two connected dome-like structures by employing the different diffusion length of Ga adatoms along the [011] and [01-1] directions [120, 212].

I used the effective-mass single-band model to estimate the energy separation between the two lowest lying confined states both for the electrons and the heavy holes, together with their spatial distribution in the quantum molecule. Due to the modest computational requirements of the simulation, it was possible to relax any assumption on the shape symmetry and use the exact geometry imaged by atomic force microscopy. Despite the quite complex morphology, the evaluation of the energy separation between the ground and first excited states reached convergence within 1 meV using 33 orthonormal wave functions per linear dimension to construct the envelope function.

An approximate electronic structure simulation allows to guide the first steps of the design of the epitaxial fabrication process and identify the more promising geometries for terahertz emission measurements among the ones accessible to the growth dynamics. Comparing the predictions evaluated on a few samples, the difference in height between the two domes of the molecule must be kept below 30% in order not to have the two-lowest lying electronic levels in the same half of the structure. The energy separation between the two levels can then be adjusted by isotropically changing the volume of the nanostructure.

Figure A.1 reports the probability to find the electron wave function inside the structure of a quantum molecule compliant with the requirements for emission in the terahertz under excitation with a femtosecond pulsed laser. In particular, the two lowest lying electronic states and the positively charged exciton formed by two electrons in these states and a heavy hole constitute a three-level Λ-like system. The ground and the first excited electron state are localized in the smaller and the bigger dome of the quantum dot molecule respectively. The energy separation between these two levels is approximately 12 meV, which fits an interesting portion of the terahertz gap around 3 THz. Instead, the energy separation between the two lowest lying heavy-hole states is only 2.5 meV, smaller than the line broadening at room temperature due to the elastic scattering with acoustic photons

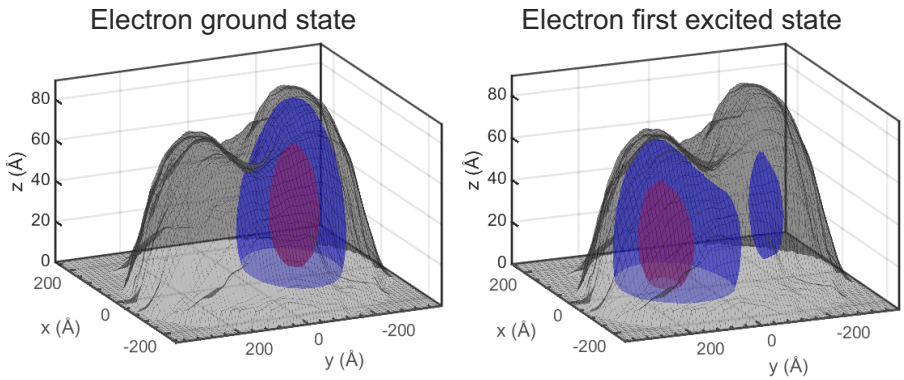

FIGURE A.1: Probability density isosurfaces (50% red, 95% blue) of the envelope function of the electron wave function confined inside a quantum molecule structure, ground (left panel) and first excited (right panel) state.

(compare with the results in Sec. 5.1.3). Assuming that the Coulomb interaction does not dramatically affect this energy separation, the hole state is effectively not localized in the excitonic complex with an electron in each of the two confined states of the bound-bound transition, thereby completing the upper part of the Λ scheme.

At the present time, measurements of terahertz generation are yet to be performed. Accurate coupling of the quantum molecules to metal nanoparticles, which is achievable by means of Ga droplet epitaxy, is expected to enhance the emission from the dipole of the bound-bound transition due to coherent-plasmonic field enhancement [209]. While I presented the versatility of the single-band effective-mass model as a tool for guiding the first stage of development of GaAs/AlGaAs nanostructures with complex geometries, experiments are needed to confirm the validity of its qualitative predictions on inter-sublevel energy separations and charge carrier localization.

Bibliography

[1] N. Gisin et al. “Quantum cryptography”. In: *Rev. Mod. Phys.* 74.1 (2002), pp. 145–195.

[2] N. Gisin and R. Thew. “Quantum communication”. In: *Nat. Photonics* 1.3 (2007), pp. 165–171.

[3] J. I. Cirac and P. Zoller. “Goals and opportunities in quantum simulation”. In: *Nat. Phys.* 8.4 (2012), pp. 264–266.

[4] A. Kandala et al. “Hardware-efficient variational quantum eigensolver for small molecules and quantum magnets”. In: *Nature* 549.7671 (2017), pp. 242–246.

[5] M. Reiher et al. “Elucidating reaction mechanisms on quantum computers”. In: *Proc. Natl. Acad. Sci. U. S. A.* (2017), p. 201619152.

[6] C. L. Degen, F. Reinhard, and P. Cappellaro. “Quantum sensing”. In: *Rev. Mod. Phys.* 89.3 (2017), p. 035002.

[7] M. A. Nielsen and I. Chuang. *Quantum computation and quantum information*. Cambridge University Press, 2010.

[8] D. Loss and D. P. DiVincenzo. “Quantum computation with quantum dots”. In: *Phys. Rev. A* 57.1 (1998), p. 120.

[9] P. Kok et al. “Linear optical quantum computing with photonic qubits”. In: *Rev. Mod. Phys.* 79.1 (2007), pp. 135–174.

[10] A. W. Harrow and A. Montanaro. “Quantum computational supremacy”. In: *Nature* 549.7671 (2017), pp. 203–209.

[11] S. J. Freedman and J. F. Clauser. “Experimental test of local hidden-variable theories”. In: *Phys. Rev. Lett.* 28.14 (1972), pp. 938–941.

[12] A. Aspect, P. Grangier, and G. Roger. "Experimental tests of realistic local theories via Bell's theorem". In: *Phys. Rev. Lett.* 47.7 (1981), pp. 460–463.

[13] J.-W. Pan et al. "Multiphoton entanglement and interferometry". In: *Rev. Mod. Phys.* 84.2 (2012), pp. 777–838.

[14] H. J. Kimble. "The quantum internet". In: *Nature* 453.7198 (2008), pp. 1023–1030.

[15] M. Bayer et al. "Fine structure of neutral and charged excitons in self-assembled In(Ga)As/(Al)GaAs quantum dots". In: *Phys. Rev. B* 65.19 (2002), p. 195315.

[16] G. Bester, S. Nair, and A. Zunger. "Pseudopotential calculation of the excitonic fine structure of million-atom self-assembled $In_{1-x}Ga_xAs$/GaAs quantum dots". In: *Phys. Rev. B* 67.16 (2003), p. 161306.

[17] A. J. Hudson et al. "Coherence of an entangled exciton-photon state". In: *Phys. Rev. Lett.* 99.26 (2007), p. 266802.

[18] I. A. Merkulov, A. L. Efros, and M. Rosen. "Electron spin relaxation by nuclei in semiconductor quantum dots". In: *Phys. Rev. B* 65.20 (2002), p. 205309.

[19] D. Huber et al. "Highly indistinguishable and strongly entangled photons from symmetric GaAs quantum dots." In: *Nat. Commun.* 8 (2017), p. 15506.

[20] R. Keil et al. "Solid-state ensemble of highly entangled photon sources at rubidium atomic transitions". In: *Nat. Commun.* 8 (2017), p. 15501.

[21] L. V. Hau et al. "Light speed reduction to 17 metres per second in an ultracold atomic gas". In: *Nature* 397.6720 (1999), pp. 594–598.

[22] N. Akopian et al. "Hybrid semiconductor-atomic interface: slowing down single photons from a quantum dot". In: *Nat. Photonics* 5.4 (2011), pp. 230–233.

[23] P. Senellart, G. Solomon, and A. White. "High-performance semiconductor quantum-dot single-photon sources". In: *Nat. Nanotechnol.* 12.11 (2017), pp. 1026–1039.

[24] H. S. Nguyen et al. "Ultra-coherent single photon source". In: *Appl. Phys. Lett.* 99.26 (2011), p. 261904.

[25] C.-Y. Lu and J.-W. Pan. "Quantum optics: Push-button photon entanglement". In: *Nat. Photonics* 8.3 (2014), pp. 174–176.

[26] S. Sanguinetti and N. Koguchi. "Chapter 4 - Droplet epitaxy of nanostructures". In: *Molecular beam epitaxy: From research to mass production*. Ed. by M. Henini. Oxford: Elsevier, 2013, p. 95.

[27] T. Kuroda et al. "Symmetric quantum dots as efficient sources of highly entangled photons: Violation of Bell's inequality without spectral and temporal filtering". In: *Phys. Rev. B* 88.4 (2013), p. 041306.

[28] K. Watanabe, N. Koguchi, and Y. Gotoh. "Fabrication of GaAs quantum dots by modified droplet epitaxy". In: *Jpn. J. Appl. Phys.* 39.2A (2000), p. L79.

[29] S. Bietti et al. "Precise shape engineering of epitaxial quantum dots by growth kinetics". In: *Phys. Rev. B* 92.7 (2015), p. 075425.

[30] R. Trotta et al. "Wavelength-tunable sources of entangled photons interfaced with atomic vapours". In: *Nat. Commun.* 7 (2016), p. 10375.

[31] Y. Chen et al. "Wavelength-tunable entangled photons from silicon-integrated III–V quantum dots". In: *Nat. Commun.* 7 (2016), p. 10387.

[32] P. Lodahl, S. Mahmoodian, and S. Stobbe. "Interfacing single photons and single quantum dots with photonic nanostructures". In: *Rev. Mod. Phys.* 87.2 (2015), p. 347.

[33] A. Chin and K. Lee. "High quality Al(Ga)As/GaAs/Al(Ga)As quantum wells grown on (111)A GaAs substrates". In: *Appl. Phys. Lett.* 68.24 (1996), pp. 3437–3439.

[34] Y. Okano et al. "Incorporation behavior of Si atoms in the molecular beam epitaxial growth of GaAs on misoriented (111)A substrates". In: *Jpn. J. Appl. Phys.* 29.8A (1990), p. L1357.

[35] A. Einstein, B. Podolsky, and N. Rosen. "Can quantum-mechanical description of physical reality be considered complete?" In: *Phys. Rev.* 47.10 (1935), pp. 777–780.

[36] J. S. Bell. "On the Einstein Podolsky Rosen paradox". In: *Physics* 1.3 (1964), pp. 195–200.

[37] B. Hensen et al. “Loophole-free Bell inequality violation using electron spins separated by 1.3 kilometres”. In: *Nature* 526.7575 (2015), pp. 682–686.

[38] J. L. O’Brien, A. Furusawa, and J. Vučković. “Photonic quantum technologies”. In: *Nat. Photonics* 3.12 (2009), pp. 687–695.

[39] I. Walmsley. “Quantum optics: Science and technology in a new light”. In: *Science* 348.6234 (2015), pp. 525–530.

[40] L.-M. Duan et al. “Long-distance quantum communication with atomic ensembles and linear optics”. In: *Nature* 414.6862 (2001), pp. 413–418.

[41] J.-W. Pan et al. “Experimental entanglement swapping: Entangling photons that never interacted”. In: *Phys. Rev. Lett.* 80.18 (1998), 3891–3894.

[42] M. Fox. *Quantum optics: an introduction*. Oxford University Press, 2006.

[43] R. Horodecki et al. “Quantum entanglement”. In: *Rev. Mod. Phys.* 81.2 (2009), pp. 865–942.

[44] K. Edamatsu. “Entangled photons: Generation, observation, and characterization”. In: *Jpn. J. Appl. Phys.* 46.11R (2007), p. 7175.

[45] A. Orieux et al. “Semiconductor devices for entangled photon pair generation: a review”. In: *Rep. Prog. Phys.* 80.7 (2017), p. 076001.

[46] J. E. Avron et al. “Entanglement on demand through time reordering”. In: *Phys. Rev. Lett.* 100.12 (2008), p. 120501.

[47] F. Troiani and C. Tejedor. “Entangled photon pairs from a quantum-dot cascade decay: The effect of time reordering”. In: *Phys. Rev. B* 78.15 (2008), p. 155305.

[48] G. Weihs, T. Huber, and A. Predojević. “Time-bin entanglement from quantum dots”. In: *Quantum dots for quantum information technologies*. Ed. by P. Michler. Springer International Publishing, 2017, pp. 267–284.

[49] E. Knill, R. Laflamme, and G. J. Milburn. “A scheme for efficient quantum computation with linear optics”. In: *Nature* 409.6816 (2001), pp. 46–52.

[50] D. Fattal et al. “Entanglement formation and violation of Bell’s inequality with a semiconductor single photon source”. In: *Phys. Rev. Lett.* 92.3 (2004), p. 037903.

[51] E. Bleuler and H. L. Bradt. “Correlation between the states of polarization of the two quanta of annihilation radiation”. In: *Phys. Rev.* 73.11 (1948), pp. 1398–1398.

[52] P. G. Kwiat et al. “New high-intensity source of polarization-entangled photon pairs”. In: *Phys. Rev. Lett.* 75.24 (1995), pp. 4337–4341.

[53] M. Takeoka, R.-B. Jin, and M. Sasaki. “Full analysis of multi-photon pair effects in spontaneous parametric down conversion based photonic quantum information processing”. In: *New J. Phys.* 17.4 (2015), p. 043030.

[54] L. Caspani et al. “Integrated sources of photon quantum states based on nonlinear optics”. In: *Light: Sci. Appl.* 6.11 (2017), p. 17100.

[55] M. Halder et al. “High coherence photon pair source for quantum communication”. In: *New J. Phys.* 10.2 (2008), p. 023027.

[56] S. M. Ulrich et al. “Correlated photon-pair emission from a charged single quantum dot”. In: *Phys. Rev. B* 71.23 (2005), p. 235328.

[57] Y.-M. He et al. “On-demand semiconductor single-photon source with near-unity indistinguishability”. In: *Nat. Nanotechnol.* 8.3 (2013), pp. 213–217.

[58] N. Somaschi et al. “Near-optimal single-photon sources in the solid state”. In: *Nat. Photonics* 10.5 (2016), pp. 340–345.

[59] X. Ding et al. “On-demand single photons with high extraction efficiency and near-unity indistinguishability from a resonantly driven quantum dot in a micropillar”. In: *Phys. Rev. Lett.* 116.2 (2016), p. 020401.

[60] O. Benson et al. “Regulated and entangled photons from a single quantum dot”. In: *Phys. Rev. Lett.* 84.11 (2000), pp. 2513–2516.

[61] W. K. Wootters. “Entanglement of formation of an arbitrary state of two qubits”. In: *Phys. Rev. Lett.* 80.10 (1998), pp. 2245–2248.

[62] D. F. V. James et al. “Measurement of qubits”. In: *Phys. Rev. A* 64.5 (2001), p. 052312.

[63] A. G. White et al. “Measuring two-qubit gates”. In: *J. Opt. Soc. Am. B* 24.2 (2007), pp. 172–183.

[64] R. M. Stevenson et al. “Biphoton interference with a quantum dot entangled light source”. In: *Opt. Express* 15.10 (2007), pp. 6507–6512.

[65] A. Fognini et al. “Path to perfect photon entanglement with a quantum dot”. In: *ArXiv:* 1710.10815 (2017). [quant-ph] https://arxiv.org/abs/1710.10815.

[66] R. M. Stevenson et al. “A semiconductor source of triggered entangled photon pairs”. In: *Nature* 439.7073 (2006), pp. 179–182.

[67] N. Akopian et al. “Entangled photon pairs from semiconductor quantum dots”. In: *Phys. Rev. Lett.* 96.13 (2006), p. 130501.

[68] R. Seguin et al. “Size-dependent fine-structure splitting in self-organized InAs/GaAs quantum dots”. In: *Phys. Rev. Lett.* 95.25 (2005), p. 257402.

[69] R. J. Young et al. “Inversion of exciton level splitting in quantum dots”. In: *Phys. Rev. B* 72.11 (2005), p. 113305.

[70] A. J. Bennett et al. “Electric-field-induced coherent coupling of the exciton states in a single quantum dot”. In: *Nat. Phys.* 6.12 (2010), pp. 947–950.

[71] A. Muller et al. “Creating polarization-entangled photon pairs from a semiconductor quantum dot using the optical Stark effect”. In: *Phys. Rev. Lett.* 103.21 (2009), p. 217402.

[72] R. Trotta et al. “Universal recovery of the energy-level degeneracy of bright excitons in InGaAs quantum dots without a structure symmetry”. In: *Phys. Rev. Lett.* 109.14 (2012), p. 147401.

[73] R. Trotta et al. “Energy-tunable sources of entangled photons: A viable concept for solid-state-based quantum relays”. In: *Phys. Rev. Lett.* 114.15 (2015), p. 150502.

[74] R. Singh and G. Bester. “Nanowire quantum dots as an ideal source of entangled photon pairs”. In: *Phys. Rev. Lett.* 103.6 (2009), p. 063601.

[75] A. Schliwa et al. “In(Ga)As/GaAs quantum dots grown on a (111) surface as ideal sources of entangled photon pairs”. In: *Phys. Rev. B* 80.16 (2009), p. 161307.

[76] E. Stock et al. “Single-photon emission from InGaAs quantum dots grown on (111) GaAs”. In: *Appl. Phys. Lett.* 96.9 (2010), p. 093112.

[77] T. Mano et al. “Self-assembly of symmetric GaAs quantum dots on (111)A substrates: Suppression of fine-structure splitting”. In: *Appl. Phys. Express* 3.6 (2010), p. 065203.

[78] K. F. Karlsson et al. “Fine structure of exciton complexes in high-symmetry quantum dots: Effects of symmetry breaking and symmetry elevation”. In: *Phys. Rev. B* 81.16 (2010), p. 161307.

[79] C. D. Yerino et al. “Strain-driven growth of GaAs(111) quantum dots with low fine structure splitting”. In: *Appl. Phys. Lett.* 105.25 (2014), p. 251901.

[80] M. A. M. Versteegh et al. “Observation of strongly entangled photon pairs from a nanowire quantum dot”. In: *Nat. Commun.* 5 (2014), p. 5298.

[81] G. Juska et al. “Towards quantum-dot arrays of entangled photon emitters”. In: *Nat. Photon.* 7.7 (2013), p. 527.

[82] A. I. Lvovsky, B. C. Sanders, and W. Tittel. “Optical quantum memory”. In: *Nat. Photonics* 3.12 (2009), pp. 706–714.

[83] G. Brennen, E. Giacobino, and C. Simon. “Focus on quantum memory”. In: *New J. Phys.* 17.5 (2015), p. 050201.

[84] R. M. Camacho et al. “Wide-bandwidth, tunable, multiple-pulse-width optical delays using slow light in Cesium vapor”. In: *Phys. Rev. Lett.* 98.15 (2007), p. 153601.

[85] C. Kupchak et al. “Room-temperature single-photon level memory for polarization states”. In: *Sci. Rep.* 5 (2015), p. 7658.

[86] R. W. Boyd and D. J. Gauthier. “Slow and fast light”. In: *Prog. Opt.* 43 (2002), pp. 497–530.

[87] K. E. Oughstun and H. Xiao. “Failure of the quasimonochromatic approximation for ultrashort pulse propagation in a dispersive, attenuative medium”. In: *Phys. Rev. Lett.* 78.4 (1997), pp. 642–645.

[88] P. Siddons et al. “Absolute absorption on rubidium D lines: comparison between theory and experiment”. In: *J. Phys. B: At., Mol. Opt. Phys.* 41.15 (2008), p. 155004.

[89] D. Bimberg, M. Grundmann, and N. N. Ledentsov. *Quantum dot heterostructures*. John Wiley & Sons, 1999.

[90] L. Pavesi and M. Guzzi. "Photoluminescence of $Al_xGa_{1-x}As$ alloys". In: *J. Appl. Phys.* 75.10 (1994), pp. 4779–4842.

[91] J. H. Davies. *The physics of low-dimensional semiconductors: an introduction*. Cambridge University Press, 1997.

[92] M. Fox. *Optical properties of solids*. Oxford University Press, 2010.

[93] J.-W. Luo, G. Bester, and A. Zunger. "Supercoupling between heavy-hole and light-hole states in nanostructures". In: *Phys. Rev. B* 92.16 (2015), p. 165301.

[94] G. Bastard. *Wave mechanics applied to semiconductor heterostructures*. John Wiley & Sons, 1990.

[95] A. Zunger. "Pseudopotential theory of semiconductor quantum dots". In: *Phys. Status Solidi B* 224.3 (2001), pp. 727–734.

[96] P. Hawrylak and M. Korkusiński. "Electronic properties of self-assembled quantum dots". In: *Single quantum dots: Fundamentals, applications, and new concepts*. Ed. by P. Michler. Springer Berlin Heidelberg, 2003, pp. 25–92.

[97] R. J. Warburton et al. "Coulomb interactions in small charge-tunable quantum dots: A simple model". In: *Phys. Rev. B* 58.24 (1998), 16221–16231.

[98] A. Bracker et al. "Binding energies of positive and negative trions: From quantum wells to quantum dots". In: *Phys. Rev. B* 72.3 (2005), p. 035332.

[99] M. Abbarchi et al. "Energy renormalization of exciton complexes in GaAs quantum dots". In: *Phys. Rev. B* 82.20 (2010), p. 201301.

[100] J.-W. Luo and A. Zunger. "Geometry of epitaxial GaAs/(Al,Ga)As quantum dots as seen by excitonic spectroscopy". In: *Phys. Rev. B* 84.23 (2011), p. 235317.

[101] H. W. van Kesteren et al. "Fine structure of excitons in type-II GaAs/AlAs quantum wells". In: *Phys. Rev. B* 41.8 (1990), pp. 5283–5292.

[102] Y. H. Huo et al. "Spontaneous brightening of dark excitons in GaAs/AlGaAs quantum dots near a cleaved facet". In: *Phys. Rev. B* 95.16 (2017), p. 165304.

[103] M. Abbarchi et al. "Exciton fine structure in strain-free GaAs/$Al_{0.3}$-$Ga_{0.7}$As quantum dots: Extrinsic effects". In: *Phys. Rev. B* 78.12 (2008), p. 125321.

[104] J. I. Pankove. *Optical processes in semiconductors*. Prentice-Hall, 2012.

[105] P. Michler. "Quantum dot single-photon sources". In: *Single semiconductor quantum dots*. Ed. by P. Michler. Springer Berlin Heidelberg, 2009, pp. 185–225.

[106] H. D. Robinson and B. B. Goldberg. "Light-induced spectral diffusion in single self-assembled quantum dots". In: *Phys. Rev. B* 61.8 (2000), R5086–R5089.

[107] A. Berthelot et al. "Unconventional motional narrowing in the optical spectrum of a semiconductor quantum dot". In: *Nat. Phys.* 2.11 (2006), pp. 759–764.

[108] M. Abbarchi et al. "Spectral diffusion and line broadening in single self-assembled GaAs/AlGaAs quantum dot photoluminescence". In: *Appl. Phys. Lett.* 93.16 (2008), p. 162101.

[109] M. Grundmann and D. Bimberg. "Theory of random population for quantum dots". In: *Phys. Rev. B* 55.15 (1997), pp. 9740–9745.

[110] M. Abbarchi et al. "Recombination lifetime of single GaAs/AlGaAs quantum dots". In: *Phys. Status Solidi C* 3.11 (2006), pp. 3860–3863.

[111] L. C. Andreani, G. Panzarini, and J.-M. Gérard. "Strong-coupling regime for quantum boxes in pillar microcavities: Theory". In: *Phys. Rev. B* 60.19 (1999), pp. 13276–13279.

[112] P. Tighineanu et al. "Single-photon superradiance from a quantum dot". In: *Phys. Rev. Lett.* 116.16 (2016), p. 163604.

[113] H. Benisty, H. De Neve, and C. Weisbuch. "Impact of planar microcavity effects on light extraction-Part I: Basic concepts and analytical trends". In: *IEEE J. Quantum Electron.* 34.9 (1998), pp. 1612–1631.

[114] J. Claudon et al. “A highly efficient single-photon source based on a quantum dot in a photonic nanowire”. In: *Nat. Photonics* 4.3 (2010), pp. 174–177.

[115] D. Leonard et al. “Direct formation of quantum-sized dots from uniform coherent islands of InGaAs on GaAs surfaces”. In: *Appl. Phys. Lett.* 63.23 (1993), pp. 3203–3205.

[116] T. Chikyow and N. Koguchi. “MBE growth method for pyramid-shaped GaAs micro crystals on ZnSe(001) surface using Ga droplets”. In: *Jpn. J. Appl. Phys.* 29.11A (1990), p. L2093.

[117] N. Koguchi and K. Ishige. “Growth of GaAs epitaxial microcrystals on an S-terminated GaAs substrate by successive irradiation of Ga and As molecular beams”. In: *Jpn. J. Appl. Phys.* 32.5R (1993), p. 2052.

[118] T. Mano et al. “Self-assembly of concentric quantum double rings”. In: *Nano Lett.* 5.3 (2005), pp. 425–428.

[119] C. Somaschini et al. “Fabrication of multiple concentric nanoring structures”. In: *Nano Lett.* 9.10 (2009), pp. 3419–3424.

[120] M. Yamagiwa et al. “Self-assembly of laterally aligned GaAs quantum dot pairs”. In: *Appl. Phys. Lett.* 89.11 (2006), p. 113115.

[121] N. Ha et al. “Size-dependent line broadening in the emission spectra of single GaAs quantum dots: Impact of surface charge on spectral diffusion”. In: *Phys. Rev. B* 92.7 (2015), p. 075306.

[122] V. Mantovani et al. “Low density GaAs/AlGaAs quantum dots grown by modified droplet epitaxy”. In: *J. Appl. Phys.* 96.8 (2004), pp. 4416–4420.

[123] T. Mano et al. “Ultra-narrow emission from single GaAs self-assembled quantum dots grown by droplet epitaxy”. In: *Nanotechnology* 20.39 (2009), p. 395601.

[124] J. G. Keizer et al. “Atomic scale analysis of self assembled GaAs/AlGaAs quantum dots grown by droplet epitaxy”. In: *Appl. Phys. Lett.* 96.6 (2010), p. 062101.

[125] C. J. Chen. *Introduction to scanning tunneling microscopy*. Oxford University Press, 2008.

[126] J. S. Villarrubia. "Algorithms for scanned probe microscope image simulation, surface reconstruction, and tip estimation". In: *J. Res. Natl. Inst. Stand. Technol.* 102.4 (1997), p. 425.

[127] E. Hecht and A. Zajac. *Optics*. Addison-Wesley, 2002.

[128] C. Kammerer et al. "Interferometric correlation spectroscopy in single quantum dots". In: *Appl. Phys. Lett.* 81.15 (2002), pp. 2737–2739.

[129] V. Zwiller, T. Aichele, and O. Benson. "Single-photon Fourier spectroscopy of excitons and biexcitons in single quantum dots". In: *Phys. Rev. B* 69.16 (2004), p. 165307.

[130] R. Loudon. *The quantum theory of light*. Oxford University Press, 2000.

[131] J. F. Clauser et al. "Proposed experiment to test local hidden-variable theories". In: *Phys. Rev. Lett.* 23.15 (1969), pp. 880–884.

[132] C. K. Hong, Z. Y. Ou, and L. Mandel. "Measurement of subpicosecond time intervals between two photons by interference". In: *Phys. Rev. Lett.* 59.18 (1987), pp. 2044–2046.

[133] H. Fearn and R. Loudon. "Theory of two-photon interference". In: *J. Opt. Soc. Am. B* 6.5 (1989), pp. 917–927.

[134] C. Santori et al. "Indistinguishable photons from a single-photon device". In: *Nature* 419.6907 (2002), pp. 594–597.

[135] S. Varoutsis et al. "Restoration of photon indistinguishability in the emission of a semiconductor quantum dot". In: *Phys. Rev. B* 72.4 (2005), p. 041303.

[136] M. Califano and P. Harrison. "Presentation and experimental validation of a single-band, constant-potential model for self-assembled InAs/GaAs quantum dots". In: *Phys. Rev. B* 61.16 (2000), pp. 10959–10965.

[137] T. Kuroda et al. "Optical transitions in quantum ring complexes". In: *Phys. Rev. B* 72.20 (2005), p. 205301.

[138] M. Jo et al. "Self-limiting growth of hexagonal and triangular quantum dots on (111)A". In: *Cryst. Growth Des.* 12.3 (2012), pp. 1411–1415.

[139] L. Esposito et al. "Ehrlich-Schwöbel effect on the growth dynamics of GaAs(111)A surfaces". In: *Phys. Rev. Materials* 1.2 (2017), p. 024602.

[140] K. Watanabe et al. “Photoluminescence studies of GaAs quantum dots grown by droplet epitaxy”. In: *J. Cryst. Growth* 227 (2001), pp. 1073–1077.

[141] D. Scarpellini et al. “Ga crystallization dynamics during annealing of self-assisted GaAs nanowires”. In: *Nanotechnology* 28.4 (2017), p. 045605.

[142] K. Sato, M. Fahy, and B. Joyce. “Reflection high energy electron diffraction intensity oscillation study of the growth of GaAs on GaAs(111)A”. In: *Surf. Sci.* 315.1 (1994), pp. 105–111.

[143] Y. Sakuma et al. “Role of thin InP cap layer and anion exchange reaction on structural and optical properties of InAs quantum dots on InP (001)”. In: *J. Vac. Sci. Technol., B: Microelectron. Nanometer Struct.–Process., Meas., Phenom.* 23.4 (2005), pp. 1741–1746.

[144] F. Guffarth et al. “Observation of monolayer-splitting for InAs/GaAs quantum dots”. In: *Phys. E* 21.2 (2004). Proceedings of the Eleventh International Conference on Modulated Semiconductor Structures, pp. 326–330.

[145] S. Bietti et al. “Gallium surface diffusion on GaAs (001) surfaces measured by crystallization dynamics of Ga droplets”. In: *J. Appl. Phys.* 116.11 (2014), p. 114311.

[146] H. Lan and Y. Ding. “Ordering, positioning and uniformity of quantum dot arrays”. In: *Nano Today* 7.2 (2012), pp. 94–123.

[147] C. Heyn et al. “Regimes of GaAs quantum dot self-assembly by droplet epitaxy”. In: *Phys. Rev. B* 76.7 (2007), p. 075317.

[148] A. Ohtake, N. Ha, and T. Mano. “Extremely high- and low-density of Ga droplets on GaAs(111)A,B: Surface-polarity dependence”. In: *Cryst. Growth Des.* 15.1 (2015), pp. 485–488.

[149] J. A. Venables, G. D. T. Spiller, and M. Hanbucken. “Nucleation and growth of thin films”. In: *Rep. Prog. Phys.* 47.4 (1984), p. 399.

[150] T. L. Einstein, A. Pimpinelli, and D. L. González. “Analyzing capture zone distributions (CZD) in growth: Theory and applications”. In: *J. Cryst. Growth* 401.S-C (2014). Proceedings of 17th International Conference on Crystal Growth and Epitaxy (ICCGE-17), pp. 67–71.

[151] K. Yamaguchi, K. Yujobo, and T. Kaizu. "Stranski-Krastanov growth of InAs quantum dots with narrow size distribution". In: *Jpn. J. Appl. Phys.* 39.12A (2000), p. L1245.

[152] Y. P. Varshni. "Temperature dependence of the energy gap in semiconductors". In: *Physica* 34.1 (1967), pp. 149–154.

[153] S. Sanguinetti et al. "Carrier thermal escape and retrapping in self-assembled quantum dots". In: *Phys. Rev. B* 60.11 (1999), pp. 8276–8283.

[154] S. Sanguinetti et al. "Temperature dependence of the photoluminescence of InGaAs/GaAs quantum dot structures without wetting layer". In: *Appl. Phys. Lett.* 81.16 (2002), pp. 3067–3069.

[155] S. Sanguinetti et al. "Carrier thermodynamics in InAs/$In_xGa_{1-x}As$ quantum dots". In: *Phys. Rev. B* 74.20 (2006), p. 205302.

[156] M. Gurioli et al. "Quantum dot decoherence measured by ensemble photoluminescence". In: *J. Appl. Phys.* 98.10 (2005), p. 103527.

[157] S. Rudin, T. L. Reinecke, and B. Segall. "Temperature-dependent exciton linewidths in semiconductors". In: *Phys. Rev. B* 42.17 (1990), p. 11218.

[158] L. Besombes et al. "Acoustic phonon broadening mechanism in single quantum dot emission". In: *Phys. Rev. B* 63.15 (2001), p. 155307.

[159] P. Borri et al. "Ultralong dephasing time in InGaAs quantum dots". In: *Phys. Rev. Lett.* 87.15 (2001), p. 157401.

[160] I. Vurgaftman, J. R. Meyer, and L. R. Ram-Mohan. "Band parameters for III–V compound semiconductors and their alloys". In: *J. Appl. Phys.* 89.11 (2001), pp. 5815–5875.

[161] L. Bouet et al. "Charge tuning in [111] grown GaAs droplet quantum dots". In: *Appl. Phys. Lett.* 105.8 (2014), p. 082111.

[162] M. Abbarchi et al. "Poissonian statistics of excitonic complexes in quantum dots". In: *J. Appl. Phys.* 106.5 (2009), p. 053504.

[163] E. Dekel et al. "Carrier-carrier correlations in an optically excited single semiconductor quantum dot". In: *Phys. Rev. B* 61.16 (2000), pp. 11009–11020.

[164] M. Müller et al. “On-demand generation of indistinguishable polarization-entangled photon pairs”. In: *Nat. Photonics* 8.3 (2014), pp. 224–228.

[165] A. V. Uskov et al. “Line broadening caused by Coulomb carrier–carrier correlations and dynamics of carrier capture and emission in quantum dots”. In: *Appl. Phys. Lett.* 79.11 (2001), pp. 1679–1681.

[166] A. V. Kuhlmann et al. “Charge noise and spin noise in a semiconductor quantum device”. In: *Nat. Phys.* 9.9 (2013), pp. 570–575.

[167] Y. H. Huo et al. “Volume dependence of excitonic fine structure splitting in geometrically similar quantum dots”. In: *Phys. Rev. B* 90.4 (2014), p. 041304.

[168] J.-P. Jahn et al. “An artificial Rb atom in a semiconductor with lifetime-limited linewidth”. In: *Phys. Rev. B* 92.24 (2015), p. 245439.

[169] P. Tighineanu et al. “Decay dynamics and exciton localization in large GaAs quantum dots grown by droplet epitaxy”. In: *Phys. Rev. B* 88.15 (2013), p. 155320.

[170] C. Heyn, C. Strelow, and W. Hansen. “Excitonic lifetimes in single GaAs quantum dots fabricated by local droplet etching”. In: *New J. Phys.* 14.5 (2012), p. 053004.

[171] P. A. Dalgarno et al. “Coulomb interactions in single charged self-assembled quantum dots: Radiative lifetime and recombination energy”. In: *Phys. Rev. B* 77.24 (2008), p. 245311.

[172] R. Trotta et al. “Highly entangled photons from hybrid piezoelectric - semiconductor quantum dot devices”. In: *Nano Lett.* 14.6 (2014), pp. 3439–3444.

[173] N. Akopian et al. “An artificial atom locked to natural atoms”. In: *ArXiv:* 1302.2005 (2013). [cond-mat.mes-hall] https://arxiv.org/abs/1302.2005.

[174] J. Wu and Z. M. Wang. “Droplet epitaxy for advanced optoelectronic materials and devices”. In: *J. Phys. D: Appl. Phys.* 47.17 (2014), p. 173001.

[175] M. Abbarchi et al. "Scanning Fabry-Pérot interferometer with largely tuneable free spectral range for high resolution spectroscopy of single quantum dots". In: *Rev. Sci. Instrum.* 82.7 (2011), p. 073103.

[176] Y. H. Huo, A. Rastelli, and O. G. Schmidt. "Ultra-small excitonic fine structure splitting in highly symmetric quantum dots on GaAs (001) substrate". In: *Appl. Phys. Lett.* 102.15 (2013), p. 152105.

[177] G. Juska et al. "Conditions for entangled photon emission from (111)B site-controlled pyramidal quantum dots". In: *J. Appl. Phys.* 117.13 (2015), p. 134302.

[178] S. Stufler et al. "Two-photon Rabi oscillations in a single $In_{1-x}Ga_xAs$/GaAs quantum dot". In: *Phys. Rev. B* 73.12 (2006), p. 125304.

[179] S. Ates et al. "Post-selected indistinguishable photons from the resonance fluorescence of a single quantum dot in a microcavity". In: *Phys. Rev. Lett.* 103.16 (2009), p. 167402.

[180] H. S. Nguyen et al. "Optically gated resonant emission of single quantum dots". In: *Phys. Rev. Lett.* 108 (5 2012), p. 057401.

[181] H. S. Nguyen et al. "Photoneutralization and slow capture of carriers in quantum dots probed by resonant excitation spectroscopy". In: *Phys. Rev. B* 87 (11 2013), p. 115305.

[182] O. Gazzano et al. "Bright solid-state sources of indistinguishable single photons". In: *Nat. Commun.* 4 (2013), p. 1425.

[183] M. Reindl et al. "Phonon-assisted two-photon interference from remote quantum emitters". In: *Nano Lett.* 17.7 (2017), pp. 4090–4095.

[184] E. A. Chekhovich et al. "Nuclear spin effects in semiconductor quantum dots". In: *Nat. Mater.* 12.6 (2013), pp. 494–504.

[185] R. B. Patel et al. "Two-photon interference of the emission from electrically tunable remote quantum dots". In: *Nat. Photonics* 4.9 (2010), pp. 632–635.

[186] M. Benyoucef et al. "Toward quantum interference of photons from independent quantum dots". In: *Appl. Phys. Lett.* 95.26 (2009), p. 261908.

[187] P. Gold et al. "Two-photon interference from remote quantum dots with inhomogeneously broadened linewidths". In: *Phys. Rev. B* 89.3 (2014), p. 035313.

[188] V. Giesz et al. “Cavity-enhanced two-photon interference using remote quantum dot sources”. In: *Phys. Rev. B* 92.16 (2015), p. 161302.

[189] E. B. Flagg et al. “Interference of single photons from two separate semiconductor quantum dots”. In: *Phys. Rev. Lett.* 104.13 (2010), p. 137401.

[190] H. Huang et al. “Electrically-pumped wavelength-tunable GaAs quantum dots interfaced with rubidium atoms”. In: *ACS Photonics* 4.4 (2017), pp. 868–872.

[191] K. D. Jöns et al. “Bright nanoscale source of deterministic entangled photon pairs violating Bell’s inequality”. In: *Sci. Rep.* 7.1 (2017), p. 1700.

[192] P. Michler et al. “A quantum dot single-photon turnstile device”. In: *Science* 290.5500 (2000), pp. 2282–2285.

[193] G. S. Solomon, M. Pelton, and Y. Yamamoto. “Single-mode spontaneous emission from a single quantum dot in a three-dimensional microcavity”. In: *Phys. Rev. Lett.* 86 (17 2001), pp. 3903–3906.

[194] A. Dousse et al. “Ultrabright source of entangled photon pairs”. In: *Nature* 466.7303 (2010), pp. 217–220.

[195] J. Zhang et al. “A nanomembrane-based wavelength-tunable high-speed single-photon-emitting diode”. In: *Nano Lett.* 13.12 (2013), pp. 5808–5813.

[196] R. Trotta et al. “Nanomembrane quantum-light-emitting diodes integrated onto piezoelectric actuators”. In: *Adv. Mater.* 24.20 (2012), pp. 2668–2672.

[197] A. G. Baca and C. I. H. Ashby. *Fabrication of GaAs devices*. The Institution of Engineering and Technology, 2005.

[198] M. Xu et al. “Metal-oxide-semiconductor field-effect transistors on GaAs (111)A surface with atomic-layer-deposited Al_2O_3 as gate dielectrics”. In: *Appl. Phys. Lett.* 94.21 (2009), p. 212104.

[199] H. Li et al. “Growth of p-type GaAs/AlGaAs(111) quantum well infrared photodetector using solid source molecular-beam epitaxy”. In: *J. Appl. Phys.* 98.5 (2005), p. 054905.

[200] Y. Horikoshi et al. "Area selective growth of GaAs by migration-enhanced epitaxy". In: *Phys. Status Solidi B* 244.8 (2007), pp. 2697–2706.

[201] T. Uehara et al. "Area-selective epitaxial growth of GaAs on GaAs-(111)A substrates by migration-enhanced epitaxy". In: *Jpn. J. Appl. Phys.* 46.2R (2007), p. 496.

[202] P. M. Petroff. "Nucleation and growth of GaAs on Ge and the structure of antiphase boundaries". In: *J. Vac. Sci. Technol., B: Microelectron. Process. Phenom.* 4.4 (1986), pp. 874–877.

[203] M. Kawabe and T. Ueda. "Molecular beam epitaxy of controlled single domain GaAs on Si (100)". In: *Jpn. J. Appl. Phys.* 25.4A (1986), p. L285.

[204] S. Strite et al. "Antiphase domain free growth of GaAs on Ge in GaAs/Ge/GaAs heterostructures". In: *Appl. Phys. Lett.* 56.3 (1990), pp. 244–246.

[205] H. Yamaguchi and Y. Horikoshi. "Step-flow growth on vicinal GaAs surfaces by migration-enhanced epitaxy". In: *Jpn. J. Appl. Phys.* 28.8A (1989), p. L1456.

[206] D. E. Aspnes et al. "Optical properties of $Al_xGa_{1-x}As$". In: *J. Appl. Phys.* 60.2 (1986), pp. 754–767.

[207] P. B. Johnson and R. W. Christy. "Optical constants of the noble metals". In: *Phys. Rev. B* 6.12 (1972), pp. 4370–4379.

[208] P. B. Johnson and R. W. Christy. "Optical constants of transition metals: Ti, V, Cr, Mn, Fe, Co, Ni, and Pd". In: *Phys. Rev. B* 9.12 (1974), pp. 5056–5070.

[209] F. Carreño et al. "Plasmon-enhanced terahertz emission in self-assembled quantum dots by femtosecond pulses". In: *J. Appl. Phys.* 115.6 (2014), p. 064304.

[210] H. G. Roskos et al. "Coherent submillimeter-wave emission from charge oscillations in a double-well potential". In: *Phys. Rev. Lett.* 68 (14 1992), pp. 2216–2219.

[211] P. C. M. Planken et al. “Terahertz emission in single quantum wells after coherent optical excitation of light hole and heavy hole excitons”. In: *Phys. Rev. Lett.* 69 (26 1992), pp. 3800–3803.

[212] Z. M. Wang et al. “Self-organization of quantum-dot pairs by high-temperature droplet epitaxy”. In: *Nanoscale Res. Lett.* 1.1 (2006), p. 57.

Acknowledgements

148 pages and 212 references only provide a glimpse at the story behind a PhD. A story made of the people I shared three years of my life with.

A special word of gratitude goes to my scientific advisor, Emiliano Bonera. He has been very supportive throughout my training in science, and I found his balanced mentoring, made of scientific expertise, trust, and respect, to be of priceless value. For everything I was taught during my stay at the Semiconductor Spectroscopy Lab in Milano-Bicocca I must thank Fabio Pezzoli and Emanuele Grilli as well, I have always received great technical and personal advising.

I have learned that collaborations are crucial to pursuit meaningful research today and had the privilege to cultivate a few fruitful and enriching ones.

Most of my PhD activities were performed in close synergy with the molecular beam epitaxy group at the L-NESS research center based in Como. Stefano Sanguinetti's extensive knowledge and his confident approach towards research have been a motivation for me to never dismiss a result as uninteresting and always look for ideas for improvement. Sergio Bietti, with his constant helpfulness and friendliness, was essential for the success of my research project. I'd like to thank him, Alexey Fedorov, and Luca Esposito for the fabrication of the samples and the AFM imaging.

I highly value the research period I spent at the JKU Institute of Semiconductor and Solid State Physics in Linz. I am grateful to Rinaldo Trotta for offering me this great opportunity. I utterly enjoyed his straight approach to problem solving and his enthusiasm in research. I also thank Armando Rastelli and everyone I worked with in Linz, Javier Martín-Sánchez, Marcus Reindl, Daniel Huber, Christian Schimpf, Johannes Aberl, Huiying Huang, Saimon Filipe Covre da Silva, Xueyong Yuan, and Michele Rota. For helping me to take my first steps in semiconductor processing and time-correlated spectroscopy, for giving me survival props as a foreigner, and for making a special work and life experience possible.

I enjoyed setting foot in the fascinating world of 2D materials too, due to the collaboration with the MDM labs in Agrate Brianza. I thank Alessandro Molle and his research group, especially Christian Martella and Silvia Vangelista with whom I had fruitful interactions.

One last element puts it all together, a fantastic office. A big thank you to Fabio, Elisa, Sebastiano, Michael, Anna, and everyone with whom I had the pleasure to share lunches and coffees, chats and rants. I loved the chemistry we had, it will remain a glad memory to glance back at, a positive model to tend to.

I won't forget to mention also who was there for me outside of the academia. To the new friends I met during these three years and to long-time ones who never let me go, thanks for the good fun together and for making me a better person.

Last but not least, a genuine hug to my family, which has constantly and lovingly supported me, despite my clumsy attempts at explaining what my work is about. Once again, the credit for this accomplishment also belongs to you.

Doctoral thesis
March 2018

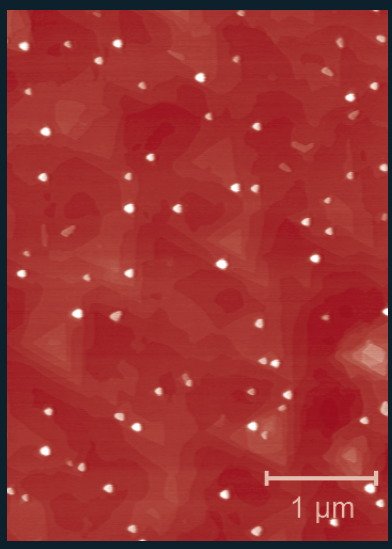

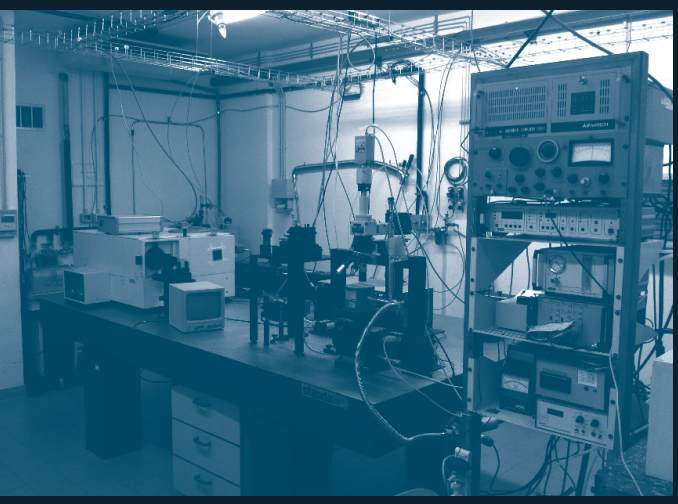

UNIVERSITÀ DEGLI STUDI DI MILANO BICOCCA